Casimir torques and lateral forces: influence of optical properties and surface morphology

Tajik, Fatemeh

university of groningen

Casimir torques and lateral forces: influence of optical properties and surface morphology

PhD thesis

to obtain the degree of PhD at the
University of Groningen
on the authority of the
Rector Magnificus Prof. E. Sterken
and in accordance with
the decision by College of Deans.

This thesis will be defended in public on

Friday 14 September 2018 at 12:45 hours

by

Fatemeh Tajik

born on 24 June 1987
in Tehran, Iran

Supervisors
Prof. G. Palasantzas
Prof. A. A. Masoudi
Prof. M. Khorrami

Assessment Committee
Prof. R. S. Decca
Prof. E. V. D. Giessen
Prof. S. Faraji
Prof. A. Aghamohammadi

Casimir torques and lateral forces: influence of optical properties and surface morphology

Fatemeh Tajik

CONTENTS

Chapter 1

Introduction

1.1 Dispersion forces

Although the macroscopic world is ruled mainly by gravity, when the objects are scaled down to micro or nano sizes then surface forces become important [1-22]. These forces are known by several different names, depending on the regime in which they operate. Therefore distinction between surface forces is in many cases rather artificial, because several of them are electromagnetic in nature, and dividing them only makes sense because of the many different ways in which electromagnetic force is manifested [1]. Dispersion forces, which are in nature and are known as van der Waals (vdW) or Casimir forces (the different names are only due to historical reasons), and originate from quantum and thermal fluctuations of electric currents inside the interacting media and in the gap separating them [2]. They become dominant when the bodies are separated by the distances smaller typically than 100 nm [2, 6-22]. They play an important role in nanotechnology including micro/nanoelectromechanical systems (MEMS/NEMS) [6-22]. This happens when two mechanical elements come in close proximity or into contact, and the surface to volume ratio increases with decreasing system size [5, 6]. In any case, dispersion forces are always present even when neutral, unpolarised and unmagnetised bodies interact in the absence of any applied electromagnetic fields [1-22].

This thesis is focused on the influence of the Casimir force and torque on the dynamical behavior of microdevices. It deals mostly with these two factors that can strongly change the functionality of microdevices. Hence it is essential

to acquire knowledge about the kind of material optical properties and surface roughness that can have an effect on Casimir forces and torques, and consequently in the dynamical behavior of MEMS in order to enhance device performance. Therefore we present a basic overview of the Casimir effect, its physical origin, and finally its practical use in microdevices, followed by a thesis outline.

1.2 van der Waals (vdW) forces

In 1873 J. D. van der Waals empirically introduced a weak attractive force between molecules in a gas to explain an observed deviation from the ideal gas law [10]. At the time the presence of such an attractive force could be understood in the case of polar molecules (molecules with a permanent dipole moment such as hydrogen or water vapor). After all, an opposite orientation of the dipole moment would be statistically favorable, so that an electrostatic attraction could occur. However, gases of nonpolar molecules were observed to exhibit a similar deviation from the ideal gas law, which could not be explained in this way and the nature of this force remained unclear [10]. This problem was resolved in 1930 by F. London [11, 12]. He showed that the quantum mechanical uncertainty of the position and the momentum of electrons in the gas give rise to a temporary dipole moment (see Fig. 1.1) in each molecule which consequently exerts an attractive electrostatic force on the other molecules. He demonstrated that the force between molecules possessing electric dipole moments fall off with distance R between the molecules as R^{-6}.

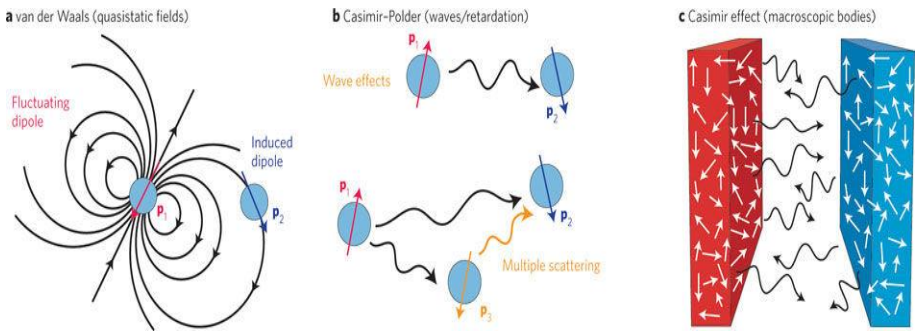

Figure 1.1: Relation between vdW and Casimir forces. A fluctuating dipole p_1 induces a fluctuating electromagnetic dipole field that induces a fluctuating dipole p_2 (Fig.1 in [6]).

In 1947 Casimir and Polder [13] generalized the London result about the vdW potential to arbitrary interatomic separations. They showed that the dependency R^{-6} is a good approximation in the non-retarded limit for distances that are much smaller than the wave length of the atomic absorption spectra (typically $< 10\ nm$). In the opposite regime, the retarded limit, for separations much larger than the atomic wave length, the vdW potential is still attractive but it falls off more strongly with increasing distance due to the influence of retardation (the finite velocity of light is taken into account). Under this condition the interaction between the molecules behaves like R^{-7} [13].

Nowadays fluctuation induced electromagnetic forces between bodies at submicrometer proximity are becoming increasingly important for applications [5, 6, 18, 21, 22]. These forces are known by several names, depending on the regime they operate, including vdW, Casimir–Polder and, more generally, Casimir forces (see Fig 1.1) [6]. They are closely related to each other since they originate from the zero point and thermal fluctuation of the electromagnetic field whose spectrum is altered by the presence of boundaries. To elaborate the connection between these forces, it is helpful to discuss their physical origin in more detail.

1.3 Connection between van der Waals and Casimir force

Let us consider two small particles such as atoms or molecules which possess equal amounts of positive and negative electric charges. In classical physics it is imagined a static arrangement such that positive and negative charge form pairs sitting exactly next to each other. Thus each pair will be electrically neutral, and it will not give rise to electric fields. However, the outcome is different in quantum physics. Due to the Heisenberg uncertainty principle [10-12,14], the motion of charges inside the particles cannot be controlled with absolute precision, and there is random motion. At any moment, positive and negative charges will be separate. This rearrangement leads to an imbalance of attractive and repulsive force such that two particles attract each other. The resulting force between two natural particles is known as the vdW force [10, 11].

Furthermore, according to classical physics, the vacuum is completely empty and it contains nothing in its purest form. However, quantum physics tell us that it is far from empty. In this view, vacuum is governed by fluctuation of electromagnetic waves which are called virtual photons [15-20]. When incident on to a perfectly conducting mirror, they must form a node on the mirror surface. So, if we place two mirrors in to quantum vacuum, then this requirement restricts the possible type of virtual photons between them, and only photons of

certain discrete wavelengths can exist. On the contrary, the virtual photons outside the mirrors can have any arbitrary wavelength. Eventually the imbalance of virtual photons hitting the mirrors from the outside leads to the attractive Casimir force between two mirrors (Fig 1.2).

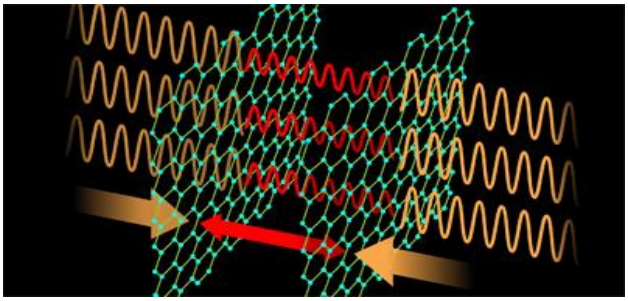

Figure 1.2: Casimir force as a consequence of vacuum fluctuations of electromagnetic field. Outside of the mirrors there is a sea of fluctuation fields but inside only certain modes of these fields can exist due to the imposed boundary. This imbalance generates the attractive Casimir force.

Thus it appears that the Casimir force is due to virtual photons, and vdW force results from the attraction between mobile charges. The two effects are similar because the mirrors impose the boundary condition for the electromagnetic field via charges. Charges inside the mirrors adapt to the fluctuating fields to vanish the field on the surface. Thus the Casimir force is not only due to field fluctuations but also due to fluctuating charges. Also, the charges inside the two particles attract and repel each other by means of the electromagnetic field. There is strong connection between fluctuating charges inside two particles as fluctuating charges inside one particle lead to fields acting on the other particle. Hence, the vdW force is also due to charge and field fluctuations.

The Casimir force was proposed by Hendrik B. G. Casimir in 1948 [2] as the attractive force between two perfectly conducting neutral parallel plates. The Casimir force depends on the distance d between the plates as

$$\frac{F_{Cas}}{A} = \frac{\pi^2 \hbar c}{240\, d^4}, \tag{1.1}$$

where A is the plate area, and ħ and c are Planck constant and speed of light respectively. Equation 1.1 is valid for perfectly conducting plates. Realistic calculation between real dielectric bodies were presented in 1952 by E. Lifshitz [14]. In terms of this theory the vdW and Casimir forces are the short and long range limits respectively of the same force.

1.4 Casimir forces in devices and practical motivation

Microelectromechanical systems (MEMS), and their extension to submicron dimensions the so-called Nanoelectromechanical systems (NEMS), are a general term used in to describe micro/nanofabricated devices. They find applications in optical communications, accelarometers, and a variety of sensor technologies. MEMS (for example see Fig. 1.3) are electrostatically actuated with the Casimir forces being omnipresent [21-25].

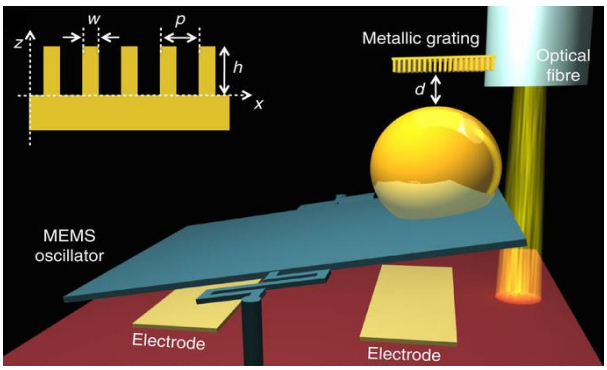

Figure 1.3: Schematic of an micromechanical (MEMS) torsional oscillator. This device measures the Casimir force between a gold-coated sphere and a nanostructured grating. The sphere is attached to the torsional plate of a micromechanical oscillator, and the nanostructured grating is fixed to a single-mode optical fibre. (Fig.1 in [26]).

Indeed, since the larger actuating force and torque is demanded with the application of smaller voltages, the separation between moving components are shrinking from micrometers to nanometers [27] implying that the role of Casimir force becomes significantly stronger for an effective treatment of device actuation properties. Nanometer separations are the right size for the Casimir effect to play role because the surface area are large enough but the gaps are

small enough for the force to draw components together and lock them permanently together. This phenomenon is usually referred as stiction and leads to loss of device functionality [28].

Moreover, by decreasing the size of MEMS, it becomes clear that surface roughness of moving components cannot be ignored since it can affect Casimir forces, and consequently the actuation dynamics of devices [29]. Another factor which has strong effect on the Casimir effect are the optical properties of materials from which devices are made. Tailoring the optical properties has become strongly relevant in developing devices for many purposes according to huge demands to involve different material [30]. It is evident that metallic bodies have significant advantages in construction of MEMS because of their valuable chemical and physical properties. On the other hand, the most important materials in nanotechnology are semiconductors, for instance silicon (Si), which is the dominant semiconductor in IC technology. They possess conductivity properties ranging from metallic to dielectric.

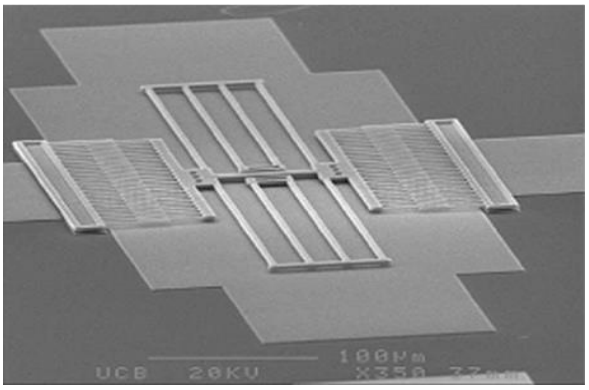

Figure 1.4: An SEM image of a SiC double-folded comb-drive Resonator (Fig.1 in [31]).

The reflectivity of semiconductors surfaces can be changed over a wide frequency range by changing the carrier density through variation of the temperature or using different kinds of doping. For example one kind of complex material, which has been under investigation in this thesis, is highly doped silicon carbide (SiC). It possesses outstanding mechanical and chemical properties. It is well integrated with Si-based MEMS technologies. Moreover due to its large electronic bandgap and high breakdown field strength, SiC is well suited for high frequency and high power solid-state devices [30,32,34]. In this thesis major focus is paid on the dynamics of torsional MEMS with respect to optical

properties, where both electrostatic and Casimir torques give contribution to describe under what conditions there is stable motion of instability due to stiction under vacuum (Figure 1.5). Operation in ambient conditions would require more surface interactions to be taken into account, as for example, capillary and hydrodynamic drag forces [35].

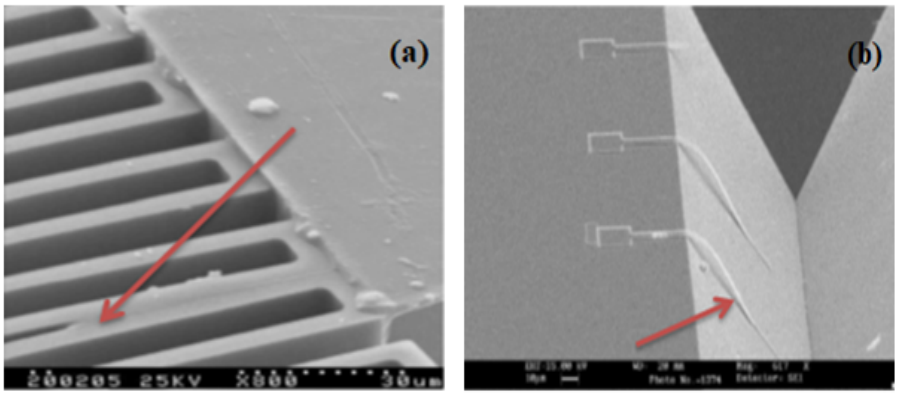

Figure 1.5: Permanent stiction in MEMS devices [68]. The arrows show adhered elements. (a) Stiction of soft microcantilevers to the substrate. (b) Microstructured elements in a micromachined accelerometer after impact loading.beam (Fig.1 in [36]).

1.5 Surface roughness: brief description of self-affine model roughness

There are three effects that must be accounted for when calculating the Casimir force between real interacting surfaces: the influence of the optical properties of the materials, the surfaces roughness, and the temperature. Temperature has been shown to have a significant effect only for separation larger than 1μm. This is because at shorter separation thermal modes do not fit between the surfaces at room temperature (thermal wavelength ~7 μm). However, at separation less than 1μm, the influence of optical properties and surfaces roughness should be carefully taken into consideration [29,37].

Advances made in the measurement and theoretical understanding of Casimir forces the last 10 years allow a more detailed study of MEMS made from real materials. It is obvious that the surface of real bodies is not characterized by a perfect geometrical shape [29, 38-42]. Even if special efforts are made to avoid large-scale deviation, from a planar or spherical shape, any real

surface is invariably covered with geometrical disorder the so-called roughness. This roughness can have profound changes in the Casimir force and the resulting operation of MEMS. It is worth mentioning that although the electrostatic force can be switched off if no potential is applied, Casimir forces will always be present (omnipresent) and will influence the actuation dynamics. This is because they originate from the quantum mechanical uncertainty, a fundamental property of nature which cannot be shut down. Roughness effects maybe on a relatively large or small scale depending on the separation distance between two bodies. In some cases roughness can be described mathematically by a regular function, but in other case the roughness can be considered as stochastic.

A wide variety of surface and interfaces occurring in nature are represented by a kind of roughness associated with self-affine fractal scaling defined by Mandelbort in terms of Brownian motion [38]. In realistic situation, evaporated metallic films can be described by the self-affine model. The importance of self-affine scaling and the relation to the Casimir force was first stressed in [39]. Isotropic rough surfaces obeying self-affine scaling are fully characterized by three parameters: root-mean-square (rms) roughness amplitude (σ), correlation length (ξ) and roughness exponent (H). The root-mean-square (rms) roughness demonstrates the deviation of the surface from flatness in the out-off plane direction. The rms roughness is defined as $\sigma = \langle [\mathrm{z(x,y)}]^2 \rangle^{1/2}$ with $\mathrm{z(x,y)} = \mathrm{h(x,y)} - \langle \mathrm{h(x,y)} \rangle$. Here $\mathrm{h(x,y)}$ is the height function, and $\langle \dots \rangle$ is an ensemble average over multiple surface scans. The average over a large surface area (with dimensions >>ξ) is zero so that $\langle \mathrm{h(x,y)} \rangle = 0$. Because there are many ways to distribute atoms on a random rough surface, which will result in the same rms amplitude, a complete description of surface roughness requires also knowledge of the lateral roughness. In this respect an important characteristic parameter is the lateral correlation length ξ, which is the average distance between adjacent peaks and valleys (an upper horizontal cut-off for the self-affine scaling). The third parameter, which is called roughness exponent (H), describes the surface irregularity at short length scales (<<ξ) and has value between 0 and 1 [40]. Values of H~0 correspond to jagged surfaces, while values H~1 correspond to a smoother hill-valley morphology (Fig. 1.6).

For self-affine roughness the height difference correlation function $\mathrm{g}(R_{X,Y}) = \langle [\mathrm{z}(x',y') - \mathrm{z(x,y)}]^2 \rangle$ with $R_{X,Y} = \sqrt{X^2 + Y^2}$, where $(\mathrm{X,Y}) = (\mathrm{x}' - \mathrm{x}, \mathrm{y}' - \mathrm{y})$, shows the scaling behavior

$$\mathrm{g}\left(R_{X,Y}\right) = \begin{cases} {R_{X,Y}}^{2\mathrm{H}} & \text{for } R_{X,Y} \ll \xi \\ 2\sigma^2 & \text{for } R_{X,Y} \gg \xi \end{cases}. \tag{1.2}$$

A simple form that satisfies the self-affine scaling of Eq. 1.2 is $g(R_{X,Y}) = 2\sigma^2[1 - e^{-((R_{X,Y})/\xi)^{2H}}]$, which has been used widely in several roughness studies [40, 41].

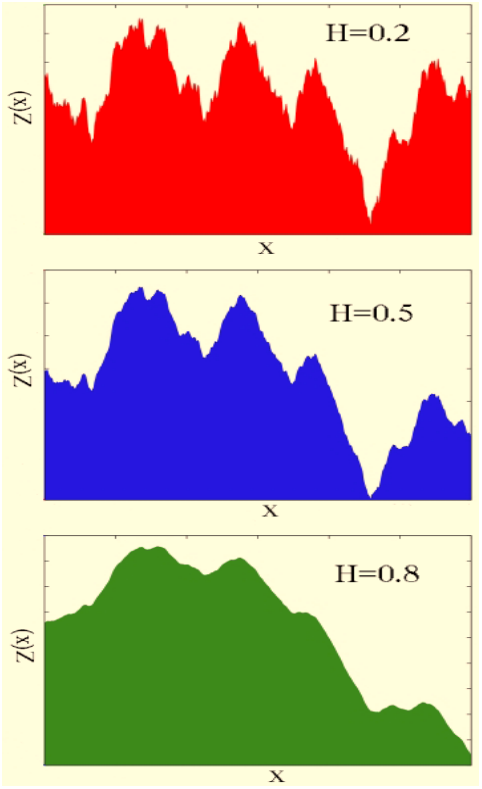

Figure 1.6: The roughness exponent describes the irregularity of surfaces at short lateral length scales (<<ξ) [40-42].

The influence of the rms roughness amplitude σ on the Casimir force is shown in Fig.1.7. Experiments have been performed between sphere (its radius is 100 μm) and a plate to measure the Casimir force [37] .The sphere was covered with 100 nm Au using an electron-beam evaporator. Silicon wafers were coated in the same way by Au to different thicknesses between 100 and 1600 nm. All of these films have different rms roughness σ and different feature size ξ (correlation length). The value of σ increases with the film thickness from 1.5 nm to 10.1 nm, while ξ is between 22 nm and 42 nm. According to Figure 1.7, thin

films (100, 200, and 400 nm) are in reasonable agreement with the theoretical expectations that take into account deviations of the dielectric functions of deposited gold from the single crystal material (via Lifshitz theory calculations [14]) and account for the roughness corrections using perturbation theory [29]. For these films the force is well described by the power law [44] $F_{Cas} \sim d^{-\alpha}$ (where d is defined as the sphere-plate separation) with the exponent α having values $2 < \alpha < 3$. However, the thick films show very different behavior. There is significant deviation from the expected scaling. The theoretical curve (black) including the roughness correction is not able to describe the measured forces as it was further described in [29].

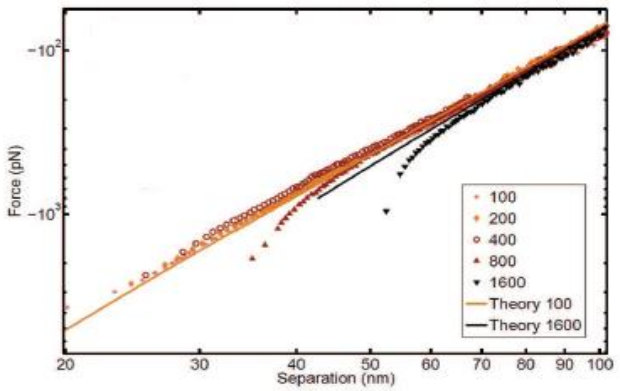

Figure 1.7: Casimir force measured for different rough surfaces on a log–log scale for various Au film thicknesses. The theoretical curves for 100 nm and 1600 nm films are shown by solid lines. [29].

Figure 1.7 shows the effect of surface roughness only on the normal Casimir forces [29]. However, in this thesis (chapter 3) we have investigated how the self-affine roughness influences the lateral Casimir force between two plates.

1.6 Thesis outline:

The outline of the present thesis as follows:

- In chapter 2 we will explain different methods used to calculate the Casimir force. The pair wise summation (PWS) method and the Lifshitz theory are discussed since they represent the main tools for our work.
- In chapter 3 and 4 we study how the correlation length and roughness exponent can affect the lateral Casimir force and Casimir torque (in both horizontal and vertical rotation).

- In chapter 5 deals with the optical properties of different surfaces (Au and SiC) to investigate their effect on the dynamic behavior of electrostatic torsional MEMS.
- In chapter 6 and 7 we study how optical properties profoundly influence dynamic and chaotic behavior in electrostatic torsional micromechanical system (MEMS) for both the case of conservative and non-conservative electrostatic torsional systems.

References

[1] J. Israelachvili, Intermolecular and Surface Forces (Academic, New York, 1992).
[2] H. B. G. Casimir, Proc. K. Ned. Akad. Wet. **51**, 793 (1948).
[3] A. W. Adamson, and A. P. Gast, Physical Chemistry of Surfaces **6**, 599 (1997).
[4] T. Abe and M. L. Reed, J. Micromech. Microeng **6**, 213 (1996).
[5] K. L. Ekinci and M. L. Roukes, Rev. Sci. Instrum **76**, 061101 (2005); A. Cleland, Foundations of Nanomechanics (Springer, New York, 2003).
[6] A. W. Rodriguez, F. Capasso, and S. G. Johnson, Nature Photonics **5**, 211 (2011).
[7] M. J. Sparnaay, Physica (Utrecht) **24**, 751 (1958); P. H. G. M. van Blockland and J. T. G. Overbeek, J. Chem. Soc. Faraday Trans **74**, 2637 (1978).
[8] S. K. Lamoreaux, Phys. Rev. Lett **78**, 5 (1997).
[9] G. Bressi, G. Carugno, R. Onofrio, G. Ruoso, Phys. Rev. Lett **88**, 041804 (2002).
[10] J. D. van der Waals, Over de Continu¨ıteit van den Gas- en Vloeistoftoestand, PhD thesis, Universiteit Leiden, 1873.
[11] F. London, "Zur Theorie und Systematik der Molekularkr¨afte", Z. Physik **63**, 245 (1930).
[12] F. London, "The general theory of molecular forces", Trans. Faraday Soc **33**, 8b (1937).
[13] H. B. G. Casimir and D. Polder, Physical Review **73**, 360 (1948).
[14] E. M. Lifshitz, Zh. Eksp. Teor. Fiz **29**, 894 (1955) [Soviet Phys. JETP 2, 73 (1956)].
[15] S. Weinberg Rev. Mod. Phys **61**, 1 (1989).
[16] K. A. Milton, The Casimir Effect: Physical Manifestations of Zero-point Energy (World Scientific, Singapore, 2001) .
[17] R. L. Jaffe, Phys. Rev. D **72**, 021301 (2005); P. W. Milonni, The Quantum Vacuum (Academic, New York, 1994).
[18] M. Bordag, U. Mohideen, and V. M. Mostepanenko, Phys. Rep **353**, 1 (2001).
[19] P. W. Milonni, The Quantum Vacuum (Academic, New York, 1994).
[20] J. Schwinger, Particles, Sources and Fields (Addison-Wesley, Reading, MA, 1970).
[21] P. Ball, Fundamental physics: Feel the force, Nature **447**, 772 (2007).
[22] F. Capasso, J.N. Munday, D. Iannuzzi, and H.B. Chan, Physics and nanomechics. IEEE J. Sel. Top. Quant. Electron **13**. 400 (2007).
[23] G. Palasantzas and J. Th. M. DeHosson, Phys. Rev. B **72**, 121409(2005).
[24] G. Palasantzas and J. Th. M. De Hosson, Phys. Rev. B **72**, 115426 (2005).
[25] W. H. Lin and Y. P. Zhao, Microsystem Technologies **11**, 80 (2005).
[26] F. Intravaia, S. Koev, W. Jung, A. A. Talin , P. S. Davids, R. S. Decca, V. A. Aksyuk, D. A. R. Dalvit and D. López, Nature Communications **4**, 2515 (2013).
[27] M. Bordag et al., Advances in the Casimir Effect (Oxford University Press, New York, 2009).
[28] R. Maboudian and R. T. Howe, J. Vac. Sci. Technol. B **15**, 1 (1997).

[29] W. Broer, H. Waalkens, V. B. Svetovoy, J. Knoester, and G. Palasantzas, Phys. Rev. Appl **4**, 054016 (2015); V. B. Svetovoy and G. Palasantzas, Adv. Colloid and Interface Science **216**, 1 (2015).
[30] Christian A. Zorman and Rocco J. Parro, p hys. stat. sol. (b) **245**, 1404(2008).
[31] N. G. Wright and A. B. Horsfall, J. Phys. D **40**, 6345 (2007).
[32] B. Stark, MEMS Reliability Assurance Guidelines for Space Applications, Jet Propulsion Laboratory Publications- 99-1.
[33] MRS Bulletin, Silicon carbide electronic materials and devices **22**, 19 (1997).
[34] R. Cheung, in Silicon Carbide Microelectromechanical Systems for Harsh Environments, edited by R. Cheung (Imperial College Press, London, 2006), Chap. 1; P. M. Sarro, Sensor Actuator A: 82, 210 (2000).
[35] F. W. DelRio, M. P. de Boer, J. A. Knapp, E. D. Reedy Jr., P. J. Clews, and M. L.Dunn, Nature Mater **4**, 629 (2005).
[36] Zhao YP, Wang LS, Yu TX, J. Adhes. Sci. Technol **17**, 519(2003).
[37] P. J. Van Zwol, G. Palasantzas, J. T. M. de Hosson, Phys. Rev. Lett **91**, 144108(2007); Phys. Rev. B **77**, 075412(2008).
[38] B. B. Mandelbrot, The Fractal Geometry of Nature (Freeman, New York, 1982).
[39] G. Palasantzas, J. Appl. Phys **97**, 126104 (2005).
[40] G. Palasantzas, Phys. Rev. B **48**, 14472 (1993); **49**, 5785 (1994); G. Palasantzas and J. Krim, Phys. Rev. Lett **73**, 3564 (1994); G. Palasantzas, Phys. Rev. E **56**, 1254 (1997).
[41] J. Krim and G. Palasantzas, Int. J. Mod. Phys. B **9**, 599 (1995).
[42] G. Palasantzas and J. Krim, Phys. Rev. B **48**, 2873 (1993).
[44] G. Palasantzas, V. B. Svetovoy, and P. J. van Zwol, Int. J. Mod. Phys. B **24**, 6013 (2010).

Chapter 2

Introduction to methods to calculate dispersion forces

2.1 Introduction

The calculation of the vacuum energy for nontrivial geometries is a complicated problem. After 20 years from Casimir's original work on plane parallel plates, Boyer presented the first calculation for a spherical shell [1]. One reason of this complication is the non-additivity in dispersion force, which is often cited as a very specific property for this kind of force [2-5]. However, another well-known example of non-additive forces is the electrostatic interaction for moving charges. The reason of non-additivity is especially clear for metals because electrons in an electric field do not keep their positions fixed, and they start to move and redistribute in response to the field.

In case of dispersive forces, it can be said that the force between two molecules depends on the position of a third molecules located nearby [5]. Consequently, the force between bodies of finite size cannot be calculated as pair wise summation of forces acting between separated molecules. If we want to address historically the process of calculating dispersion forces, it can be stated that the first two approximation methods were pairwise summation (PWS) which dates back to Lennard-Jones (1932) [6], and the proximity force approximation (PFA) (Derjaguin 1934) [7].

Therefore, in this chapter we will be explain the method to calculate the Casimir energy. It is organized into two main parts: i) The first part deals with two rough plates, which are perfectly conductive. Then the use of the PWS method under certain conditions allows one to use the perturbative approach. As a result one can calculate the Casimir energy between two rough plates for perfect reflectors without consideration of their optical properties; ii) In the second part we consider flat plates, which, however, are made from real materials and their optical properties are taken into account via the Lifshitz theory [8].

2.2 Pairwise Summation method

Here we consider a simple approximate method which allows calculation of the Casimir force between two bodies as a sum of the forces acting between their constituents (atoms or molecules). Although the Casimir force is not an additive quantity, the effects of non additivity can be partially taken into account with the help of a special normalization procedure which relates the case under consideration to a similar configuration where both the additive and the exact results are available. The additive method has been widely used in the theory of dispersion forces following Lennard-Jones (1932) [6].

To illustrate the method, we start with a configuration of two thick plates (semispaces) at a sufficiently large separation d. Here, it is supposed that they are ideal metals and perfectly conductive. Let the boundary plane of the lower semispace be at $z = 0$ and let that of the upper semispace be at $z = d$. We assume that two atoms (one in the lower semispace at a point r_1 and the other in the upper semispace at a point r_2) are characterized by an interaction energy

$$E^{AA}(r) = \frac{-B}{r^7}, \tag{2.1}$$

where the constant B is related to the static atomic polarizabilities and $r = |r_2 - r_1|$. After integration of Eq. 2.1 over the lower semispace, we find the additive interaction energy of an atom at a point r_2 with the lower semispace,

$$E_A^{add}(z_2) = -2\pi N_1 B \int_0^\infty \rho \, d\rho \int_{-\infty}^0 \frac{dz_1}{[(z_2-z_1)^2+\rho^2]^{\frac{7}{2}}} = \frac{-\pi N_1 B}{10 z_2^4}. \tag{2.2}$$

Here N_1 is the number of atoms per unit volume in the lower semispace. Integrating Eq. (2.2) over the volume of the upper semispace, we find the additive Casimir energy of the two plates (semispaces),

$$E_{pp}^{add}(d) = \frac{-\pi N_1 N_2 BS}{10} \int_d^\infty \frac{dz_2}{z_2^4} = \frac{-\pi N_1 N_2 BS}{30 d^3}, \tag{2.3}$$

where N_2 is the density of atoms in the upper semispace, and S is the infinite area of the boundary surfaces. As mentioned before, Eq. 2.3 does not take into account the effects of non additivity. The role of these effects in a configuration of two semispaces can be characterized by the normalization constant

$$K_E = \frac{E_{pp}^{add}(d)}{E(d)S} = \frac{24 N_1 N_2 B}{\pi \hbar c} \tag{2.4}$$

where $E(d)$ is Casimir energy per unit area between two ideal metals at separation d. The latter takes the non additivity effects into account. We now deal with two arbitrarily shaped bodies V_1 and V_2. In this case the additive interaction energy takes the form

$$E^{add}(d) = -B N_1 N_2 \int_{V_1} dr_1 \int_{V_2} \frac{dr_2}{|r_2 - r_1|^7}. \tag{2.5}$$

By assuming that for two arbitrary bodies the effects of non additivity plays approximately the same role as for two thick parallel plates, one can define the normalized interaction energy as [9]

$$E^{tot}(d) = \frac{E^{add}(d)}{K_E} = \frac{-\pi\hbar c}{24}\int_{V_1} dr_1 \int_{V_2} \frac{dr_2}{|r_2 - r_1|^7} \tag{2.6}$$

Eventually, Eq. 2.6 represents the Casimir energy of two ideal-metal bodies in the framework of the PWS method.

2.3 Method of pairwise summation for rough surfaces

As it mentioned in previous chapter, many bodies in nature or in laboratory conditions have rough surfaces that can affect profoundly the Casimir effect. A possible way to cope with this is a perturbative approach [10, 11], where it is assumed that a rough surface is a small deviation from smooth surface. This approximation is valid at separation d much larger than rms roughness σ ($d \gg \sigma$).

The method of pairwise summation (PWS) allows one to calculate roughness corrections for large-scale roughness of both the deterministic and stochastic nature [12]. Here, we apply the approximate phenomenological PWS method to describe the roughness corrections to the Casimir force between bodies. A perturbation theory up to forth order in the relative roughness amplitude is developed for the configurations of two parallel plates. The results obtained are applied to the case of large-scale roughness in accordance with the validity regime of the PWS method [11].

We note that for these calculation to be valid a few assumption were made. At first, this method is valid in the case of small separation in comparison to the correlation length ($\xi \gg d$). This is because it assumes the contribution of different areas to be independent of each other. Also, it is considered that the size of the plate (L) is much larger than the correlation length ($L \gg \xi$). This ensures that the interaction area contains many independent realizations of rough surfaces and hence spatial averages are equivalent to statistical averages. Furthermore, our approach requires a large size of the plate in comparison to the separation ($L \gg d$), which ensures that edge effect can be ignored.

Now we consider two parallel plates with sides of length L, and with surface roughness described by self-affine model (Chap. 1, Eq. 1.2). Both of the plates are supposed perfectly conductive, isotropic and homogeneous. The descriptions of the rough surfaces of the first and second plates are given by:

$$Z_1(x,y) = h_1(x,y), \tag{2.7}$$

$$Z_2(x',y') = d + h_2(x',y'), \tag{2.8}$$

Where the averages of h_i's vanishes at each point since we have

$$\langle h_i(x,y)\rangle = 0. \tag{2.9}$$

Now we perform the perturbative expansion of the integral Eq. 2.6 containing the Casimir-Polder interatomic potential over the volumes of the rough plates:

$$E = \frac{-\pi\hbar c}{24} \int d^2x\ d^2x' \int_{-\infty}^{h_1} dz \int_{d+h_2}^{\infty} dz' [(\mathbf{x}-\mathbf{x}')^2 + (z-z')^2]^{\frac{-7}{2}} \tag{2.10}$$

We also define $F \equiv F(\mathbf{x},\mathbf{x}',z,z') = [(\mathbf{x}-\mathbf{x}')^2 + (z-z')^2]^{\frac{-7}{2}}$ where $\mathbf{x} = (x,y)$ and $\mathbf{x}' = (x',y')$. The integrations in Eq. (2.10), are over the first ($\mathbf{x}$) and second ($\mathbf{x}'$) plates, respectively. Both integrals in z and z' direction can be broken into two parts $\int_{-\infty}^{h_1} dz = \int_{-\infty}^{0} 0 + \int_{0}^{h_1} 0$and $\int_{d+h_2}^{\infty} dz = \int_{d+h_2}^{d} 0 + \int_{d}^{\infty} 0$, where one part is independent on roughness and the other one depends on it. According to the fact that h_1 and h_2 are small, we can expand roughness dependent integrals around $z = 0$ and $z' = d$ as:

$$\int_0^{h_1} F\, dz = h_1 F|_{z=0} + \frac{h_1^2}{2}\frac{\partial F}{\partial z}|_{z=0} + \frac{h_1^3}{6}\frac{\partial^2 F}{\partial z^2}|_{z=0} + \frac{h_1^4}{24}\frac{\partial^3 F}{\partial z^3}|_{z=0} + \cdots \tag{2.11}$$

$$\int_d^{d+h_2} F\, dz' = h_2 F|_{z'=d} + \frac{h_2^2}{2}\frac{\partial F}{\partial z'}|_{z'=d} + \frac{h_2^3}{6}\frac{\partial^2 F}{\partial z'^2}|_{z'=d} + \frac{h_2^4}{24}\frac{\partial^3 F}{\partial z'^3}|_{z'=d} + \cdots \tag{2.12}$$

Inserting Eqs. 2.11 and 2.12 in Eq. 2.10 and then substituting the integrand with its statistical average, and assuming homogeneity, it is seen that the integrand of Eq. 2.10 would depend on $(\mathbf{x}-\mathbf{x}')$. So, one can perform one of the integrations to obtain

$$E = E_0 \sum_{m,n=0}^{\infty} \int \frac{d^2x}{d^2}\, \alpha_{mn}(\mathbf{x})\, \frac{h_{mn}(\mathbf{x})}{\mathbf{d^{m+n}}} \tag{2.13}$$

where $E_0 = \frac{-\pi^2\hbar c A}{720\, d^3}$ is the Casimir energy between two ideal metal plates with flat surfaces and $h_{mn}(\mathbf{x}) = \langle [h_1(\mathbf{x})]^m\ [h_2(\mathbf{0})]^n\rangle$. In the zeroth-order expansion (i.e. for m = n = 0) we have $E = E_0$. Then it follows from this that

$\alpha_{mn}(\mathbf{x}) = \frac{d^2}{\int d^2x}$. According to our choice in Eq. 2.9, $\alpha_{01}(\mathbf{x})$ and $\alpha_{10}(\mathbf{x})$ do not have any contribution in the result. The other coefficients up to fourth order are obtained as:

$$\alpha_{02}(\mathbf{x}) = \alpha_{20}(\mathbf{x}) = \frac{15}{\pi} \frac{d^7}{(x^2+d^2)^{\frac{7}{2}}} \tag{2.14}$$

$$\alpha_{03}(\mathbf{x}) = \alpha_{30}(\mathbf{x}) = \frac{35}{\pi} \frac{d^9}{(x^2+d^2)^{\frac{9}{2}}} \tag{2.15}$$

$$\alpha_{04}(\mathbf{x}) = \alpha_{40}(\mathbf{x}) = \frac{35}{4\pi}\left[\frac{d^9}{(x^2+d^2)^{\frac{9}{2}}} - 9\frac{d^{11}}{(x^2+d^2)^{\frac{11}{2}}}\right] \tag{2.16}$$

$$\alpha_{11}(\mathbf{x}) = \frac{-30}{\pi} \frac{d^7}{(x^2+d^2)^{\frac{7}{2}}} \tag{2.17}$$

$$\alpha_{12}(\mathbf{x}) = -\alpha_{21}(\mathbf{x}) = \frac{-105}{\pi} \frac{d^9}{(x^2+d^2)^{\frac{9}{2}}} \tag{2.18}$$

$$\alpha_{13}(\mathbf{x}) = \alpha_{31}(\mathbf{x}) = \frac{35}{\pi}\left[\frac{d^9}{(x^2+d^2)^{\frac{9}{2}}} - 9\frac{d^{11}}{(x^2+d^2)^{\frac{11}{2}}}\right] \tag{2.19}$$

2.4 Lifshitz theory

Fluctuation induced electromagnetic (EM) forces between two objects arise due to perturbation of quantum fluctuations of the EM field [3,4,8], as it was predicted by H. Casimir in 1948 [3] assuming two perfectly conducting parallel plates. Following Casimir's calculation, Lifshitz and co-workers in the 1950's [8] considered the general case of real dielectric plates by exploiting the fluctuation-dissipation theorem, which relates the dissipative properties of the plates (optical absorption by many microscopic dipoles) and the resulting EM fluctuations. The theory correctly describes the attractive interaction due to quantum fluctuations for all separations covering both the Casimir (long-range) and van der Waals (short-range) regimes [8].

The dependence of the Casimir force on materials is an important topic since in principle one can tailor the force by engineering the boundary conditions of the electromagnetic field with a suitable choice of materials [5-19]. The latter allows the exploration of new concepts in actuation dynamics of MEMS. This is because MEMS engineering is conducted at the micron to nanometer

length scales. As a result Casimir forces become of increasing interest because MEMS have surface areas large enough and gaps small enough for the Casimir force not only to draw components together but also to lock them permanently. On the other hand, the irreversible adhesion of moving parts resulting in general from Casimir and electrostatic forces can be exploited to add new functionalities to MEMS architectures.

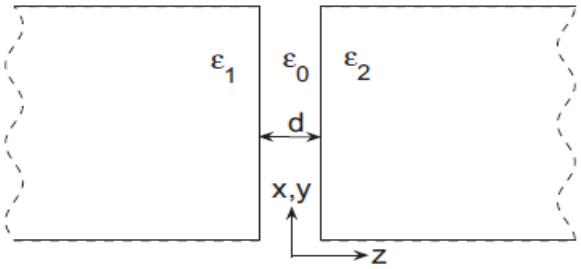

Fig. 2.1: Schematic view of two semispaces separated by a distance d, which is used to illustrate the Lifshitz theory [5, 8].

2.5 Fluctuation dissipation theorem

The fundamental idea of the Lifshitz theory is that the interaction between bodies is established through fluctuating electromagnetic fields obeying the fluctuation-dissipation theorem (FDT) [13, 14]. The FDT theorem is a powerful tool in statistical physics for predicting the behavior of systems, and it applies to both classical and quantum mechanical systems. Such fluctuating EM fields are always present inside and extend beyond the material boundaries. A well-known example of this fundamental idea is thermal radiation. However, it has to be stressed that electromagnetic fluctuations exist even at zero temperature as zero-point quantum fluctuations. The electric polarization $\mathbf{P}(\omega, \mathbf{r})$, or the electric current density $\mathbf{J}(\omega, \mathbf{r}) = -i\omega\mathbf{P}(\omega, \mathbf{r})$, is the source of these fluctuations[4-5]. Understanding of these fluctuations is easy in the case of metallic surfaces. A point $\boldsymbol{r}$ where the density of electrons is smaller than that of its surrounding will attract electrons - and change to a current - to increase the density at $\boldsymbol{r}$. According to the FDT, the correlations of the fluctuating currents are related to the dissipation in the medium as:

$$\langle J_\alpha(\omega, \mathbf{r}) J_\beta^*(\omega', \mathbf{r}') \rangle = \omega\varepsilon''(\omega)\left(\frac{\hbar\omega}{2} + \frac{\hbar\omega}{e^{\hbar\omega/kT}-1}\right)\delta(\omega - \omega')\delta(\mathbf{r} - \mathbf{r}')\delta_{\alpha\beta} \qquad (2.20)$$

where $\alpha, \beta = x, y, z$ are the vector components. The imaginary part $[\varepsilon''(\omega)]$ of the frequency dependent permittivity $[\varepsilon(\omega)]$ is associated with the dissipation of the EM fields in the interacting bodies. The FDT explains that the existence of dispersion forces is closely related to the dissipation in the materials of interacting bodies.

In Eq. 2.20 the contributions from the zero-point and thermal fluctuations are separated. The first and second term on the right hand side of Eq. 2.20 represent zero point energy and thermal contributions respectively. The fluctuating currents are the sources of an electromagnetic field. This field is described by the Maxwell equations and solutions of these equations can be expressed via the Green functions [13-14]. For instance the components of the electric field are

$$E_\alpha(\omega, \mathbf{r}) = \frac{i}{\omega} \int d\,\mathbf{r}'\, G_{\alpha\beta}(\omega, \mathbf{r}, \mathbf{r}')\, J_\beta(\omega, \mathbf{r}'), \tag{2.21}$$

where $G_{\alpha\beta}$ denotes the components of the Green Function Tensor (GFT). The GFT implies the role of the response in linear response theory. Combining Eq. 2.20 and Eq. 2.21 with the general properties of the GFT, one obtains the correlation function of the electric field:

$$\langle E_\alpha(\omega, \boldsymbol{r}) E_\beta^*(\omega', \boldsymbol{r}') \rangle = 2\pi\omega\hbar \coth\left(\frac{\hbar\omega}{2kT}\right) Im G_{\alpha\beta}(\omega, \boldsymbol{r}, \boldsymbol{r}') \delta(\omega - \omega') \tag{2.22}$$

The correlation functions of the magnetic field can be easily found by applying Maxwell's equations. The Green tensor, which is the solution of the Maxwell equations, can be expressed via the equation:

$$\left[\partial_\alpha \partial_\beta - \delta_{\alpha\beta}\left(\nabla^2 + \frac{\omega^2}{c^2}\,\varepsilon(\omega, \boldsymbol{r})\right)\right] G_{\alpha\gamma}(\omega, \boldsymbol{r}, \boldsymbol{r}') = 4\pi \frac{\omega^2}{c^2} \delta_{\alpha\beta} \delta(\boldsymbol{r} - \boldsymbol{r}') \tag{2.23}$$

In Eq. (2.23) $\varepsilon(\omega, \boldsymbol{r})$ describes the dielectric function of the interacting materials.

2.6 Real frequency representation

The explicit form of the Green functions can be easily found for two parallel plates, which are interacting via long wavelength fluctuations. The simplest

configuration consists of two semi spaces made from different materials characterized by the dielectric functions $\varepsilon_1(\omega)$ and $\varepsilon_2(\omega)$, separated by a small gap, which is filled with the material described by the dielectric function $\varepsilon_0(\omega)$ (Fig. 2.1). For parallel plates, the force acting on each body is calculated via the Green functions. The final result for the force (per unit area) can be written as

$$F(T,z) = \frac{1}{2}\frac{\hbar}{\pi^2}\int_0^\infty d\omega \coth\left(\frac{\hbar\omega}{2kT}\right)\ \mathrm{Re}\int_0^\infty dq\ q\ |k_0|\ g(\mathbf{q},\omega) \tag{2.24}$$

where the wave vector in the gap is $K = (\mathbf{q}, k_0)$ with $\mathbf{q}$ being the in-plane vector, and the z component $k_0 = (\varepsilon_0\omega^2/c^2 - \mathbf{q}^2)^{1/2}$. The function $g(\mathbf{q},\omega)$ is given by

$$g(\mathbf{q},\omega) = \sum_{\nu=s,p}\frac{r_1^\nu r_2^\nu e^{2ik_0 z}}{1 - r_1^\nu r_2^\nu e^{2ik_0 z}} \tag{2.25}$$

The coefficients $r_{1,2}^\nu$ are the Fresnel reflection coefficients (see Eq. 2.26 below) for the inner surfaces of the plates 1 and 2. In this format, $\nu = s$ and $\nu = p$ represent the transverse electric (TE) and transverse magnetic (TM) polarization, respectively. The factor $g(\mathbf{q},\omega)$ describes multiple reflections from the inner surfaces of the bodies 1 and 2. The frequency dependent factor $\coth(\hbar\omega/2kT)$ originates from the FDT. Finally, the Fresnel reflection coefficients are given by

$$r_i^s = \frac{k_0 - k_i}{k_0 + k_i} \quad , \quad r_i^p = \frac{\varepsilon_i k_0 - \varepsilon_0 k_i}{\varepsilon_i k_0 + \varepsilon_0 k_i} \tag{2.26}$$

where

$$k_0 = \sqrt{\varepsilon_0(\omega)\frac{\omega^2}{c^2} - \boldsymbol{q}^2} \quad , \quad k_i = \sqrt{\varepsilon_i(\omega)\frac{\omega^2}{c^2} - \boldsymbol{q}^2} \quad . \tag{2.27}$$

The real frequency representation of Eq.2.24 is unpractical for force calculations because the integrand is a fast oscillating function due to the factor $e^{ik_0 z}$. However, there are cases where the use of the real frequency representation is necessary to consider as for example, when the plates have different temperatures leading to non-equilibrium situations [15,16]. Besides that, the research in this thesis has been performed under equilibrium conditions and for the short distance range $z \lesssim 200$ nm. Indeed, at room temperature, $T = 300$ k, the thermal wavelength is $\lambda_T = \hbar c/kT = 7.6\ \mu m$. Therefore, since $\lambda_T \gg z$ thermal fluctuations will not give any significant contributions to dispersion forces.

2.7 Imaginary frequency representation

The problem of fast oscillations in Eq. 2.24 is usually avoided by the contour rotation in the frequency complex plane. Because of this process, only the poles of the function $\coth(\hbar\omega/\mathrm{kT})$ contribute to the integral. These poles are located at following frequencies:

$$\omega_n = \mathrm{i}\zeta_n = \mathrm{i}\frac{2\pi \mathrm{nkT}}{\hbar}, \quad \mathrm{n} = 0, 1, 2, \ldots \tag{2.28}$$

where ζ denotes the imaginary part of frequency, which is known as the Matsubara frequency. After this transformation the Lifshitz formula takes the form

$$\mathrm{F(T,z)} = \frac{\mathrm{kT}}{\pi}\sum_{\mathrm{n=0}}^{\infty}{}' \int_0^{\infty} \mathrm{d}\mathbf{q}\ \mathbf{q}\ |\mathrm{k_0}|\ \sum_{\nu=\mathrm{s,p}} \frac{\mathrm{r_1^\nu r_2^\nu e^{2ik_0 z}}}{1-\mathrm{r_1^\nu r_2^\nu e^{2ik_0 z}}} \tag{2.29}$$

where prime indicates that the term corresponding $n = 0$ term should be multiplied with a factor $1/2$. Unlike the real frequency representation, here the quantities $k_0 = \sqrt{\varepsilon_0(i\zeta)(\zeta^2/c^2 + q^2}$ and $g(q, i\zeta_n) = \sum_{\nu=s,p}(r_1^\nu r_2^\nu e^{2ik_0 z}/ 1 - r_1^\nu r_2^\nu e^{2ik_0 z})$ no longer oscillate as a function of frequency. According to the relation $coth(\hbar\omega/kT) = 1 + 2/\,[exp(\hbar\omega/kT) - 1]$, only the first term on the right side persist in the limit $T \to 0$, associated with the zero point energy. At separation distance much shorter than λ_T (i.e. in this study $d = 200\,nm$), the contribution of thermal fluctuations becomes negligible. In this way the Matsubara frequency can be used as a continuous variable, and the sum in Eq. 2.29 changes to an integral if we substitute $\frac{kT}{\pi}\sum_{n=0}^{\infty}{}' \to \frac{\hbar}{2\pi^2}\int_0^{\infty} d\zeta$. Therefore, Eq. 2.29 becomes:

$$\mathrm{F(z)} = \frac{\hbar}{2\pi^2}\int_0^{\infty} \mathrm{d}\zeta \int_0^{\infty} \mathrm{d}\mathbf{q}\ \mathbf{q}\ \mathrm{k_0}\ \sum_{\nu=\mathrm{s,p}} \frac{\mathrm{r_1^\nu r_2^\nu e^{-2k_0 z}}}{1-\mathrm{r_1^\nu r_2^\nu e^{-2k_0 z}}} \tag{2.30}$$

The reflection coefficients in this case depend only on the dielectric functions at imaginary frequencies $\varepsilon(i\zeta)$. These functions cannot be directly measured, but they can be expressed via the measurable function $\varepsilon''(\omega)$ with the help of the Kramers–Kronig relation [5, 16]

$$\varepsilon\,(\mathrm{i}\zeta) = 1 + \frac{2}{\pi}\int_0^{\infty} \frac{\omega\varepsilon''(\omega)}{\omega^2+\zeta^2} \tag{2.31}$$

The general property of $\varepsilon(i\zeta)$ is that this function is real, positive, and decreases with increasing ζ. It also shows that the dispersion forces are completely determined by $\varepsilon''(\omega)$, which is responsible for the dissipation in the material. As it mentioned before in order to evaluate the force with the Lifshitz formula, one has to know the dielectric function of the material at imaginary frequencies $\varepsilon(i\xi)$, which is calculated via $\varepsilon''(\omega)$ according to Eq. 2.31. This issue will be addressed in the next section.

2.8 Dielectric function and methods for extrapolation

The experimental data available for $\varepsilon''(\omega)$ are always restricted from low and high frequencies. The low-frequency, cutoff ω_{cut} is especially important in the case of metals, such as Au, which show significant absorption due to conduction charge carriers in the infrared range. Hence, in metals ε'' is large at low frequencies which contribute significantly to $\varepsilon(i\xi)$. Therefore, an important step in the evaluation of $\varepsilon(i\xi)$is extrapolation of the dielectric function $\varepsilon''(\omega)$ to low frequencies $\omega < \omega_{cut}$, where the experimental data are not accessible. One simple method which can solve this problem is the Drude model. This model describes the dielectric function at low optical frequencies as:

$$\varepsilon(\omega)_D = \varepsilon_o - \frac{\omega_p^2}{\omega(\omega + i\omega_\tau)}. \tag{2.32}$$

The second term in Eq. 2.32 is defined by the plasma frequency ω_p, and the relaxation frequency ω_τ. The ratio ${\omega_p}^2/\omega_\tau$ is an indication for static conductivity (for $\omega \to 0$) of the material [5, 16]. The Drude model is often used for extrapolating in the low optical frequency regime $0 < \omega < \omega_1 (= 0.03\, eV)$. In the high optical frequency range $\omega > \omega_2$, which is significant only at separations smaller than 10 nm, the imaginary part of the permittivity is extrapolated as an inverse power law $\varepsilon''(\omega) \sim 1/\omega^3$. Therefore, for frequencies $\omega < \omega_1$ and $\omega > \omega_2$, $\varepsilon''(\omega)$ is extrapolated as

$$\omega < \omega_1 (= 0.03\ \text{eV}):\ \varepsilon''(\omega) = \frac{\omega_p^2 \omega_\tau}{\omega(\omega^2 + \omega_\tau^2)}, \omega > \omega_2 (= 9.34\ \text{eV}): \varepsilon''(\omega) = \frac{A}{\omega^3} \tag{2.33}$$

where A is chosen to match the value of $\varepsilon''(\omega)$ at $\omega = \omega_2$ between experimental data and the extrapolation. Using the Drude model, the dielectric function $\varepsilon(i\xi)$ in all frequencies can be written as:

$$\varepsilon(i\xi) = 1 + \frac{2}{\pi}\int_{\omega_1}^{\omega_2} \frac{\omega\, \varepsilon''_{exp}(\omega)}{\omega^2 + \xi^2}\, d\omega + \Delta_L\varepsilon(i\xi) + \Delta_H\varepsilon(i\xi) \tag{2.34}$$

where

$$\Delta_L\varepsilon(i\xi) = \frac{2}{\pi}\int_0^{\omega_1} \frac{\omega\, \varepsilon''_L(\omega)}{\omega^2 + \xi^2}\, d\omega$$
$$\Delta_H\varepsilon(i\xi) = \frac{2}{\pi}\int_{\omega_2}^{\infty} \frac{\omega\, \varepsilon''_H(\omega)}{\omega^2 + \xi^2}\, d\omega \tag{2.35}$$

The integrals of the extrapolations can also be found analytically:

$$\Delta_H\varepsilon(i\xi) = \frac{2}{\pi}\int_{\omega_2}^{\infty} \frac{\omega\varepsilon''(\omega)}{\omega^2+\zeta^2} d\omega = \frac{2\omega_2^3\varepsilon''(\omega_2)}{\pi\zeta^2}\left[\frac{1}{\omega_2} - \frac{\frac{\pi}{2} - \arctan(\omega_2/\zeta)}{\zeta}\right] \tag{2.36}$$

$$\Delta_L\varepsilon(i\xi) = \frac{2}{\pi}\int_0^{\omega_1} \frac{\omega\varepsilon''(\omega)}{\omega^2+\zeta^2} d\omega = \frac{2\omega_p^2\omega_\tau}{\pi(\zeta^2-\omega_\tau^2)}\left[\frac{\arctan(\omega_1/\omega_\tau)}{\omega_\tau} - \frac{\arctan(\omega_1/\zeta)}{\zeta}\right]. \tag{2.37}$$

However, the Drude model, which is used to calculate the Casimir force via the Lifshitz theory, leads to deviations from experimental force results. The latter remains still today an open problem in Casimir physics [17-19]. For metals this issue is very well addressed by the dissipationless plasma model (having infinite absorption at the frequency $\omega = 0$ and zero anywhere else) at separations above 160 nm [5, 16]. The plasma model formula is straightforward to apply. At low optical frequencies $\omega < \omega_1$, the term $\Delta_L\varepsilon(i\zeta)$ from the Drude model (Eq.(2.34)) is replaced by ω_p^2/ζ^2, yielding

$$\varepsilon(i\zeta)_P = 1 + \frac{2}{\pi}\int_{\omega_1}^{\omega_2} \frac{\omega\varepsilon''_{exp}(\omega)}{\omega^2+\zeta^2} d\omega + \frac{\omega_p^2}{\zeta^2} + \Delta_H\varepsilon(i\zeta) \tag{2.38}$$

References

[1] T. H. Boyer, Phys. Rev. **174**, 1764(1968).
[2] H. C. Hamaker, Phisica **4**, 1058 (1937).
[3] H. B. G. Casimir, Proc. K. Ned. Akad. Wet. **51**, 793 (1948).
[4] Parsegian VA: Van der Waals forces. Cambridge, UK: Cambridge University Press (2006).
[5] V.B. Svetovoy , G. Palasantzas , Advances in Colloid and Interface Science **216**, 1–19 (2015): G Torricelli, P J van Zwol, O Shpak, G Palasantzas, V B Svetovoy, C Binns, B J Kooi, P Jost and M Wuttig , Adv. Funct. Mater. **22**, 3729 (2012).
[6] J. E. Lennard-Jones, Trans. Faraday Soc. **28**, 333 (1932).
[7] B. V. Derjaguin, Theorie des Anhaftens kleiner Teilchen. Kolloid Z. **69**, 155(1934).
[8] E. M. Lifshitz, Zh. Eksp. Teor. Fiz. **29**, 894 (1955) [Soviet Phys. JETP **2**, 73 (1956)].
[9] V. M. Mostepanenko and I. Yu. Sokolov, Doklady Akad. Nauk SSSR **298**, 1380 [Sov. Phys. Dokl. (USA) **33**, 140] (1988).
[10] C. Genet, S. Reynaud and A. Lambrecht, Europhys. Lett. **62**, 484 (2003).
[11] P. A. Maia Neto, A. Lambrecht, and Serge Reynaud, Phys. Rev. A. **72**, 012115 (2005).
[12] M. Bordag et al., "*Advances in the Casimir Effect* "(Oxford University Press, New York, 2009)**.**
[13] LD Landau, EM Lifshitz. Electrodynamics of continuous media, Oxford: Pergamon Press (1963).
[14] LD Landau, EM Lifshitz. Statistical physics, part 1. Oxford: Pergamon; (1986).
[15] M Antezza, LP Pitaevskii, S Stringari, VB Svetovoy. Phys Rev A. **77**, 022901(2008).
[16] V.B Svetovoy, P.J.van Zwol, GPalasantzas, , J.Th.M. DeHosson, Phys. Rev. B **77**, 035439 (2008); P.J. van Zwol, G. Palasantzas, J.Th.M.De Hosson, Phys. Rev. **79**, 195428 (2009).
[17] R. S. Decca, D. López, E. Fischbach, G. L. Klimchitskay, D. E. Krause, and V. M. Mostepanenko, Phys. Rev. D **75**, 077101 (2007).
[18] R.S. Decca , D. López , E. Fischbach , G.L. Klimchitskaya , D.E. Krause, V.M. Mostepanenko, Annals of Physics **318**, 37 (2005).; R. S. Decca, D. Lopez, E. Fischbach, and D. E. Krause, Phys. Rev. Lett. **91**, 050402 (2003).
[19] G. L. Klimchitskaya, U. Mohideen, and V. M. Mostepanenko Rev. Mod. Phys. **81**, 1827 (2009); U. Mohideen and Anushree Roy, Phys. Rev. Lett. **81**, 4549 (1998).

Chapter 3

Lateral Casimir forces between self-affine rough surfaces

Abstract. *The effect of self-affine roughness on the lateral Casimir force between two plates isstudied using a perturbative expansion method. The PWS (pairwise summation) method is applicable only at lateral correlation lengths much larger than the separation between two plates. The effect of the roughness parameters on the lateral Casimir force is investigated, and it is seen that this effect is significant, enabling one to tailor roughness parameters to obtain the desirable Casimir force and increase the yield of micro or nano-electromechanical devices based on the vacuum fluctuations.*

This chapter has been published in :

F Tajik, A A Masoudi, M Khorrami, "Lateral Casimir force between self-affine rough surfaces", *Physica B: Condensed Matter* 485, 116 (2016).

3.1 Introduction

During the last few decades, there has been much interest in devices of length scales of micro meters or nanometers, the so-called micro (nano) electromechanical systems (MEMS-NEMS). In such devices, the Casimir effect which is negligible in macro systems plays an important role. This effect was discovered by H. Casimir in 1948 [1]. He calculated that in the zero-temperature limit, two parallel flat conducting plates attract each other with the force F,

$$F_{Cas} = \frac{\pi^2 \hbar c A}{240\, d^4}, \tag{3.1}$$

where d is the separation of the plates, A is the surface area of each plate, and c and $\hbar$ are the speed of light and the reduced Planck constant, respectively. The Casimir force is a prediction of quantum field theory, arising as a result of the dependence of the zero- point vacuum fluctuations of the electromagnetic field on the boundaries. So, this force depends on the shape of the boundary surfaces [2]. It is known that surfaces are not exactly smooth in the micro (nano) scales. So the roughness could affect the Casimir force in micro (nano) devices. Recently, many high-precision (with the uncertainties of a few percents) have been performed to measure the normal Casimir force [3–8], using for example, the torsion pendulum [3], the atomic force microscope (AFM) [8]. The force measured in those experiments is perpendicular to two surfaces [9]. In [10], it is shown that the normal Casimir force is increased when the roughness of the surfaces increased.

Similar to the normal Casimir force, the lateral Casimir force arises from the boundary induced modifications of the zero-point electromagnetic field fluctuation. The lateral force is a tangential force acting between the two surfaces. Ref. [11] describes an experiment showing the lateral Casimir force between a sinusoidally corrugated plate and a large corrugated sphere. In [2,12–14], the lateral Casimir force between two periodically rough surfaces has been studied. Here the lateral Casimir force between two self-affine rough plates is studied. As mentioned above, in MEMS (NEMS) the Casimir force and the roughness are two important factors. Here the aim is to investigate the effect of different parameters of such surfaces on the magnitude of the lateral Casimir force. The lateral Casimir force vanishes if the two surfaces are uncorrelated. So it is assumed that there is a nonzero cross-correlation between the two surfaces. The two plates are assumed to be ideal conductors. They are also assumed to be isotropic, homogeneous, and self-affine rough surfaces [15]. Self-affine surfaces are characterized by the rms roughness (σ), the lateral correlation length (ξ), and the roughness exponent (H), which is between 0 and1. H is a

measure of the irregularity of the surface at short length scales (<ξ) [15]: small (large) values of H correspond to jagged (smoother) surfaces (see Fig. 3.1) [15].

For our analysis here the PWS (pair wise summation) method is used. This is based on pair wise summation of interaction energy between constituents of the two bodies [16–18]. This method is applicable only at ξ much larger than separation between two surfaces. Under this condition, the PWS method is very accurate [2]. The scheme of the paper is the following. In Section 3.2 the method and the model are introduced. In Section 3.3 the results are discussed. Section 3.4 is devoted to the concluding remarks.

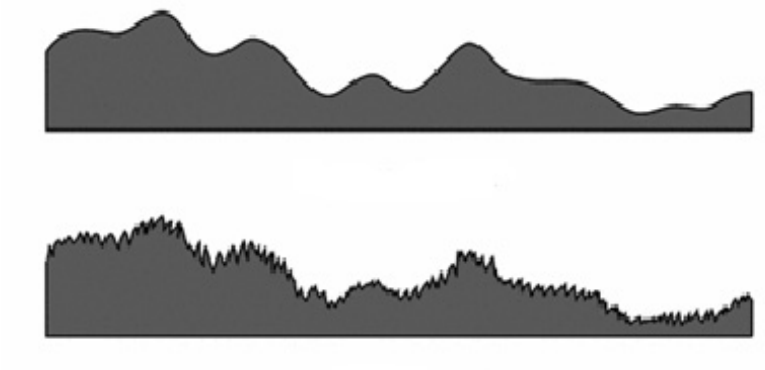

Figure 3.1: Two self-affine surfaces with different value of the roughness exponent (H). The upper surface has the larger value of H.

3.2 The model

The self-affine rough surfaces of the plates are described through

$$Z_1(\mathbf{x}) = h_1(\mathbf{x}) \tag{3.2}$$

$$Z_2(\mathbf{x}) = d + h_2(\mathbf{x}), \tag{3.3}$$

where Z_i is the height of the ith surface, x is the (two-dimensional) position vector in each plate, d is the average distance between the two plates (which is position-independent). The averages of h_i's vanishe at each point:

$$\langle h_i(\mathbf{x})\rangle = 0 \tag{3.4}$$

The plates are assumed to be surfaces of area A. As it was mentioned in chapter 2 (Sect. 2.3), the conditions for the validity of the PWS method, and applying the perturbation method to consider roughness effect, can be written as:

$$|\mathrm{h_i}| \ll d \tag{3.5}$$

$$\mathrm{d} \ll \xi \tag{3.6}$$

$$\xi \ll \mathrm{L} \tag{3.7}$$

where ξ is the lateral correlation length in each plate (the lateral correlation length), and L is the size of the plates. The Casimir energy for two rough plates (see chapter 2 Sect. 3 Eq. 2.10) can be written as:

$$\mathrm{E} = \frac{-\pi\hbar c}{24} \int \mathrm{d^2x}\ \mathrm{d^2x'}\ \varepsilon[\mathbf{x}-\mathbf{x}', \mathrm{h_1}(\mathbf{x}), \mathrm{h_2}(\mathbf{x})] \tag{3.8}$$

where the integration regions for $\mathbf{x}$ and $\mathbf{x}'$ are the first and second plates, respectively. Substituting the integrand with its statistical average, and assuming homogeneity, it is seen that the integrand would depend on only $(\mathbf{x}-\mathbf{x}')$. So one can perform one of the integrations to obtain

$$\mathrm{E} = \frac{-\pi\hbar c}{24} \int \mathrm{d^2x}\ \ \varepsilon[\mathbf{x}, \mathrm{h_1}(\mathbf{x}), \mathrm{h_2}(\mathbf{0})] \tag{3.9}$$

Homogeneity also means that the statistical averages of functions of only $\mathrm{h_1}(\mathbf{x})$ or $\mathrm{h_2}(\mathbf{x})$ do not depend on $\mathbf{x}$. One can then split the Casimir energy into two parts, $\mathrm{E_1}$ which is not changed when $\mathrm{h_1}$ or $\mathrm{h_2}$ are transformed (the plates are laterally transformed), and a remaining part $\tilde{E}$, where

$$\mathrm{E_1} = \mathrm{E}|_{\mathrm{h_1}=0} + \mathrm{E}|_{\mathrm{h_2}=0} - \mathrm{E}|_{\mathrm{h_1}=\mathrm{h_2}=0} \tag{3.10}$$

Thus, we have

$$\widetilde{\mathrm{E}} = \frac{-\pi\hbar c}{24} \int \mathrm{d^2x}\ \mathrm{d^2x'} \int_0^{\mathrm{h_1}} \mathrm{dz} \int_{\mathrm{d+h_2}}^{\mathrm{d}} \mathrm{dz'}[(\mathbf{x}-\mathbf{x}')^2 + (\mathrm{z}-\mathrm{z}')^2]^{\frac{-7}{2}} =$$
$$: \frac{-\pi\hbar c}{24} \int \mathrm{d^2x}\ \ \tilde{\varepsilon}[\mathbf{x}, \mathrm{h_1}(\mathbf{x}), \mathrm{h_2}(\mathbf{0})] \tag{3.11}$$

This can be expanded in terms of $\mathrm{h_1}$ and $\mathrm{h_2}$:

$$\widetilde{\mathrm{E}} = \frac{-\pi\hbar c}{24} \sum_{m,n=1}^{\infty} \int \mathrm{d}^2\mathrm{x}\ \ \tilde{\varepsilon}_{mn}(\mathbf{x})\, \mathrm{h}_{mn}(\mathbf{x}) \ = \\ -\mathrm{E}_0 \ \sum_{m,n=1}^{\infty} \int \frac{\mathrm{d}^2\mathrm{x}}{\mathrm{d}^2}\ \alpha_{mn}(\mathbf{x})\ \frac{\mathrm{h}_{mn}(\mathbf{x})}{\mathbf{d^{m+n}}} \tag{3.12}$$

where

$$\mathrm{E}_0 = \frac{-\pi^2\hbar c A}{720\, \mathrm{d}^3}, \tag{3.13}$$

$$\mathrm{h}_{mn}(\mathbf{x}) = \overline{\{[\mathrm{h}_1(\mathbf{x})]^m\ \ [\mathrm{h}_2(\mathbf{x})]^n\}} \tag{3.14}$$

$$\alpha_{mn} = \ \frac{30\, \mathrm{d}^{5+m+n}}{\pi}\ \tilde{\varepsilon}_{\boldsymbol{mn}} \tag{3.15}$$

$(-\mathrm{E}_0)$ is the Casimir energy between two flat plates. As E_1 does not change by a lateral translation of the plates, it is $\tilde{E}$ which is relevant to the calculation of the lateral Casimir force. In fact it is seen that if the second plate is laterally transformed by **r**, the result would be a change of $\mathrm{h}_2(\mathbf{x})$ into $\mathrm{h}_2(\mathbf{x}-\mathbf{r})$, so that $\mathrm{h}_{mn}(\mathbf{x})$ is changed into $\mathrm{h}_{mn}(\mathbf{x}+\mathbf{r})$. Defining $\widetilde{\mathrm{E}}(\mathbf{r})$ as

$$\widetilde{\mathrm{E}}(\mathbf{r}) = -\mathrm{E}_0 \ \sum_{m,n=1}^{\infty} \int \frac{\mathrm{d}^2\mathrm{x}}{\mathrm{d}^2}\ \alpha_{mn}(\mathbf{x})\ \frac{\mathrm{h}_{mn}(\mathbf{x}+\mathbf{r})}{\mathrm{d}^{m+n}} \tag{3.16}$$

it is seen that the lateral force $\mathrm{F}_\perp$ satisfies

$$\mathbf{F}_\perp = -\nabla_r\left[\widetilde{\mathrm{E}}(\mathbf{r})\right] \tag{3.17}$$

Assuming that the probability distribution of h_1 and h_2 is invariant under $(\mathrm{h}_1, \mathrm{h}_2) \to (-\mathrm{h}_1, -\mathrm{h}_2)$, it turns out that in Eq.3.12 only the terms with (m+n). So, up to fourth order in h_1 and h_2 only three terms in Eq. 3.12 are nonvanishing:

$$\alpha_{11}(\mathbf{x}) = \ \frac{-30}{\pi}\ \frac{\mathrm{d}^7}{(\mathbf{x}^2+\mathrm{d}^2)^{\frac{7}{2}}} \tag{3.18}$$

$$\alpha_{31}(\mathbf{x}) = \alpha_{13}(\mathbf{x}) = \ \frac{35}{\pi}\left[\ \frac{\mathrm{d}^9}{(\mathbf{x}^2+\mathrm{d}^2)^{\frac{9}{2}}} - 9\frac{\mathrm{d}^{11}}{(\mathbf{x}^2+\mathrm{d}^2)^{\frac{11}{2}}}\right] \tag{3.19}$$

One has

$$\overline{[\mathrm{h}_\mathrm{i}(\mathbf{x})]^2} \ = \sigma_\mathrm{i}^2 \tag{3.20}$$

$$\overline{[h_1(\mathbf{x})h_2(\mathbf{x}')]} = c_{12}(\mathbf{x}-\mathbf{x}'). \tag{3.21}$$

σ_i is the rms roughness of the ith plate and c_{12} is the cross correlation function between the two plates, and use has been made of the homogeneity of the system, so that σ_i are constant in both plates and c_{12} depends on only the relative position of the observation points. Using the approximations [20],

$$\begin{aligned}\overline{\{[h_1(\mathbf{x})]^3\ [h_2(\mathbf{x}')]^1\}} &\approx \overline{[h_1(\mathbf{x})]^2}\ \ \overline{[h_1(\mathbf{x})h_2(\mathbf{x}')]} = \sigma_1^2 c_{12}(\mathbf{x}-\mathbf{x}'),\\ \overline{\{[h_1(\mathbf{x})]^1\ [h_2(\mathbf{x}')]^3\}} &\approx \overline{[h_2(\mathbf{x}')]^2}\ \ \overline{[h_1(\mathbf{x})h_2(\mathbf{x}')]} = \sigma_2^2 c_{12}(\mathbf{x}-\mathbf{x}')\end{aligned} \tag{3.22}$$

one arrives at the following form for the Casimir energy:

$$\widetilde{E}(\mathbf{r}) = -E_0 \int \frac{d^2x}{d^2}\left[\alpha_{11}(\mathbf{x}) + \frac{\sigma_1^2+\sigma_2^2}{d^2}\,\alpha_{13}(\mathbf{x})\right]\frac{c_{12}(\mathbf{x}+\mathbf{r})}{d^2} + \cdots \tag{3.23}$$

For the cross correlation, a model corresponding to rough hetero-structures is used [21–23]:

$$c_{12}(\mathbf{x}) = \gamma_{12}\sqrt{c_2(\mathbf{x})c_1(\mathbf{x})} \tag{3.24}$$

$$\gamma_{12} = \exp(-\frac{d}{\xi_\perp}), \tag{3.25}$$

where c_i is the auto correlation function in the ith plate, and $\xi_\perp$ is the vertical correlation length. If the system is isotropic as well, then the correlations would depend on only x. For self-affine surfaces [24,25],

$$c_i(\mathbf{x}) = \sigma_i^2 \exp[-\left(\frac{d}{\xi_i}\right)^{2H_i}] \tag{3.26}$$

Thus we have,

$$c_{12}(\mathbf{x}) = \gamma_{12}\sigma_1\sigma_2 \exp[-\frac{1}{2}\left(\frac{d}{\xi_1}\right)^{2H_1} - \frac{1}{2}\left(\frac{d}{\xi_2}\right)^{2H_2}] \tag{3.27}$$

From which,

$$\widetilde{E}(\mathbf{r}) = -\frac{E_0\,\gamma_{12}\,\sigma_1\,\sigma_2}{d^2}\int\frac{d^2x}{d^2}\left[\alpha_{11}(\mathbf{x}) + \frac{\sigma_1^2+\sigma_2^2}{d^2}\,\alpha_{13}(\mathbf{x})\right]\exp[-\frac{1}{2}\left(\frac{|\mathbf{x}+\mathbf{r}|}{\xi_1}\right)^{2H_1} - \frac{1}{2}\left(\frac{|\mathbf{x}+\mathbf{r}|}{\xi_2}\right)^{2H_2}] + \cdots \quad (3.28)$$

Exploiting the isotropy of the system, it is seen that $\widetilde{E}$ depends on only $|\mathbf{r}|$, which is denoted by r. Also the lateral force would be radial:

$$\vec{\mathbf{F}}_\perp = \hat{\mathbf{r}}F_\perp$$
$$F_\perp = -\hat{\mathbf{r}}.\nabla_r[\widetilde{E}\,(\mathbf{r})] \quad (3.29)$$

where $\hat{\mathbf{r}}$ is the radial (two-dimensional) unit vector. One then arrives at

$$F_\perp = E_0\int\frac{d^2x}{d^2}\left[\alpha_{11}(\mathbf{x}) + \frac{\sigma_1^2+\sigma_2^2}{d^2}\alpha_{13}(\mathbf{x})\right]\times\frac{\hat{\mathbf{r}}.\mathbf{x}+r}{|\mathbf{x}+\mathbf{r}|}\frac{1}{d^2}\frac{d[c_{12}(|\mathbf{x}+\mathbf{r}|)]}{d|\mathbf{x}+\mathbf{r}|} + \cdots \quad (3.30)$$

So using Eq.(27),

$$F_\perp = -\frac{F_0\,\gamma_{12}\,\sigma_1\,\sigma_2}{d^2}\int\frac{d^2x}{d^2}\left[\alpha_{11}(\mathbf{x}) + \frac{\sigma_1^2+\sigma_2^2}{d^2}\alpha_{13}(\mathbf{x})\right]\times \frac{\hat{\mathbf{r}}.\mathbf{x}}{3d}\left[\frac{H_1 d^2}{\xi^2{}_1}\left(\frac{|\mathbf{x}+\mathbf{r}|}{\xi_1}\right)^{2(H_1-1)} + \frac{H_2 d^2}{\xi^2{}_2}\left(\frac{|\mathbf{x}+\mathbf{r}|}{\xi_2}\right)^{2(H_2-1)}\right]\times \exp[\frac{-1}{2}\left(\frac{|\mathbf{x}+\mathbf{r}|}{\xi_1}\right)^{2H_1}\frac{-1}{2}\left(\frac{|\mathbf{x}+\mathbf{r}|}{\xi_2}\right)^{2H_2}] \quad (3.31)$$

where

$$F_0 = \frac{3E_0}{d} = \frac{\pi^2\hbar c A}{240\,d^4} \quad (3.32)$$

for small values of r, the Casimir energy in Eq. 3.28 is seen to be

$$\widetilde{E}(\mathbf{r}) = \widetilde{E}(0) + \frac{r^2}{2d^2}\frac{E_0\,\gamma_{12}\,\sigma_1\,\sigma_2}{d^2}\int\frac{d^2x}{d^2}\left[\alpha_{11}(\mathbf{x}) + \frac{\sigma_1^2+\sigma_2^2}{d^2}\,\alpha_{13}(\mathbf{x})\right]\times \exp\left[-\frac{1}{2}\left(\frac{x}{\xi_1}\right)^{2H_1} - \frac{1}{2}\left(\frac{x}{\xi_2}\right)^{2H_2}\right]\times\left\{\frac{1}{2}\left[H_1^2\left(\frac{x}{\xi_1}\right)^{2H_1} + H_2^2\left(\frac{x}{\xi_2}\right)^{2H_2}\right] - \frac{H_1H_2}{2}\left(\frac{x}{\xi_1}\right)^{2H_1}\left(\frac{x}{\xi_2}\right)^{2H_2} - \frac{1}{4}\left[H_1^2\left(\frac{x}{\xi_1}\right)^{4H_1} + H_2^2\left(\frac{x}{\xi_2}\right)^{4H_2}\right]\right\}\frac{2d^2}{x^2} + \cdots \quad (3.33)$$

For $r \ll \xi_1, \xi_2$.Thus we obtain

$$F_{\perp} = -\frac{r}{3d}\frac{F_0\,\gamma_{12}\,\sigma_1\,\sigma_2}{d^2}\int\frac{d^2x}{d^2}\left[\alpha_{11}(\mathbf{x}) + \frac{\sigma_1^2+\sigma_2^2}{d^2}\,\alpha_{13}(\mathbf{x})\right] \times \exp[-\frac{1}{2}\left(\frac{x}{\xi_1}\right)^{2H_1} - \frac{1}{2}\left(\frac{x}{\xi_2}\right)^{2H_2}] \times \left\{\frac{1}{2}\left[H_1^2\left(\frac{x}{\xi_1}\right)^{2H_1} + H_2^2\left(\frac{x}{\xi_2}\right)^{2H_2}\right] - \frac{H_1H_2}{2}\left(\frac{x}{\xi_1}\right)^{2H_1}\left(\frac{x}{\xi_2}\right)^{2H_2} - \frac{1}{4}\left[H_1^2\left(\frac{x}{\xi_1}\right)^{4H_1} + H_2^2\left(\frac{x}{\xi_2}\right)^{4H_2}\right]\right\}\frac{2d^2}{x^2} + \cdots \quad (3.34)$$

For $\xi_i = \xi$ and $H_i = H$, these become

$$\widetilde{E}(\mathbf{r}) = \widetilde{E}(0) + \frac{r^2}{2d^2}\frac{E_0\,\gamma_{12}\,\sigma_1\,\sigma_2}{d^2}\int\frac{d^2x}{d^2}\left[\alpha_{11}(x) + \frac{\sigma_1^2+\sigma_2^2}{d^2}\alpha_{13}(x)\right] \times \exp\left[-\left(\frac{x}{\xi}\right)^{2H}\right] \times \{H^2\left[\left(\frac{x}{\xi}\right)^{2H} - \left(\frac{x}{\xi}\right)^{4H}\right]\}\frac{2d^2}{x^2} + \cdots \quad r \ll \xi \quad (3.35)$$

$$F_{\perp} = -\frac{-r}{3d}\frac{F_0\,\gamma_{12}\,\sigma_1\,\sigma_2}{d^2}\int\frac{d^2x}{d^2}\left[\alpha_{11}(x) + \frac{\sigma_1^2+\sigma_2^2}{d^2}\alpha_{13}(x)\right] \times \exp\left[-\left(\frac{x}{\xi}\right)^{2H}\right] \times \{H^2\left[\left(\frac{x}{\xi}\right)^{2H} - \left(\frac{x}{\xi}\right)^{4H}\right]\}\frac{2d^2}{x^2} + \cdots \quad (3.36)$$

for $r \ll \xi$. It is seen that for small values of r, the energy is quadratic in r, hence the lateral force is linear in r. For large values of r, a saddle point approximation could be used to obtain the Casimir energy and the lateral force:

$$\widetilde{E}(\mathbf{r}) = -\frac{E_0\,\gamma_{12}\,\sigma_1\,\sigma_2}{d^2}\int\frac{d^2x}{d^2}\left[\alpha_{11}(\mathbf{r}) + \frac{\sigma_1^2+\sigma_2^2}{d^2}\,\alpha_{13}(\mathbf{r})\right] \times \exp\left[-\frac{1}{2}\left(\frac{x}{\xi_1}\right)^{2H_1} - \frac{1}{2}\left(\frac{x}{\xi_2}\right)^{2H_2}\right] + \cdots = \frac{E_0\,\gamma_{12}\,\sigma_1\,\sigma_2}{d^2}\left(\frac{30}{\pi}\frac{d^7}{r^7}\right)\int\frac{d^2x}{d^2}\exp\left[-\frac{1}{2}\left(\frac{x}{\xi_1}\right)^{2H_1} - \frac{1}{2}\left(\frac{x}{\xi_2}\right)^{2H_2}\right] + \cdots \quad (3.37)$$

for $r \gg \xi_1, \xi_2$. Thus we obtain,

$$F_{\perp} = \frac{F_0\,\gamma_{12}\,\sigma_1\,\sigma_2}{d^2}\left(\frac{30}{\pi}\frac{d^8}{r^8}\right)\int\frac{d^2x}{d^2}\exp\left[-\frac{1}{2}\left(\frac{x}{\xi_1}\right)^{2H_1} - \frac{1}{2}\left(\frac{x}{\xi_2}\right)^{2H_2}\right] + \cdots \quad (3.38)$$

and for $\xi_i = \xi$ and $H_i = H$,

$$\widetilde{E}(\mathbf{r}) = \frac{E_0\,\gamma_{12}\,\sigma_1\,\sigma_2}{d^2}\,\frac{\pi\xi^2}{d^2}\,\Gamma\left(1+\frac{1}{H}\right)\left(\frac{30}{\pi}\frac{d^7}{r^7}\right) + \cdots \quad r \gg \xi \quad (3.39)$$

And

$$F_{\perp} = \frac{F_0\,\gamma_{12}\,\sigma_1\,\sigma_2}{d^2}\,\frac{\pi\xi^2}{d^2}\,\Gamma\left(1+\frac{1}{H}\right)\left(\frac{70}{\pi}\frac{d^8}{r^8}\right) + \cdots \quad r \gg \xi \quad (3.40)$$

It is seen that for large values of r, the energy is proportional to r^{-7}, hence the lateral force is proportional to r^{-8}.

3.3 Results and Discussion

The explicit form of the Green functions can be easily found for two parallel plates The dimensionless lateral Casimir force is denoted by f:

$$f = \frac{d^2}{F_0\, \gamma_{12}\, \sigma_1\, \sigma_2}\ F_{\perp} \tag{3.41}$$

In Figures 3.2 and 3.3, the same roughness parameters (σ, ξ, H) are used for both plates. According to Eq. 3.5 and 3.6, it has been considered in this study:

$$\frac{d}{\xi} = 0.2, \text{ and } \frac{\sigma}{d} = 0.2 \tag{3.42}$$

Figure 3.2 shows f as a function of (r/ξ) for different values of H. The lateral force tends to zero as the displacement tends to zero. The lateral force is repulsive (tends to increase the displacement), if the cross correlation between the plates is positive (γ_{12} is positive). Otherwise it is attractive. Increasing the displacement, the lateral force reaches a peak and then decreases, as for large displacements the correlation of points in the plates which are in front of each other vanishes, and the smaller the value of H (the more jugged the plates), the peak of the lateral force is achieved in smaller displacements.

Figure 3.3 shows f as a function of H, for$\xi = r$, which is an intermediate value for r, neither too small nor too large. It is seen that for such intermediate values of (r/ξ) is increasing with H. In the limit of $r \ll \xi$, the lateral force is proportional to r. Figure 3.4 shows the dimensionless force constant k as a function of H, where

$$k = 3d\frac{f}{r} = \frac{3d^3}{F_0\, \gamma_{12}\, \sigma_1\, \sigma_2}\ \frac{F_{\perp}}{r} \tag{3.43}$$

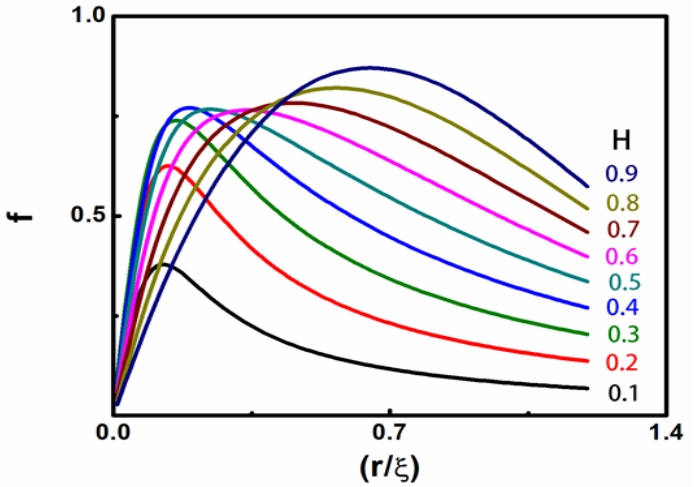

Figure 3.2: f versus (r/ξ) for (d/ξ)=(σ/d)=0.2, and H=0.1 to 0.9, with H increasing by 0.1 at each step. f is the dimensionless lateral force, and the graphs are so that f is increasing with H at (r/ξ)=1.

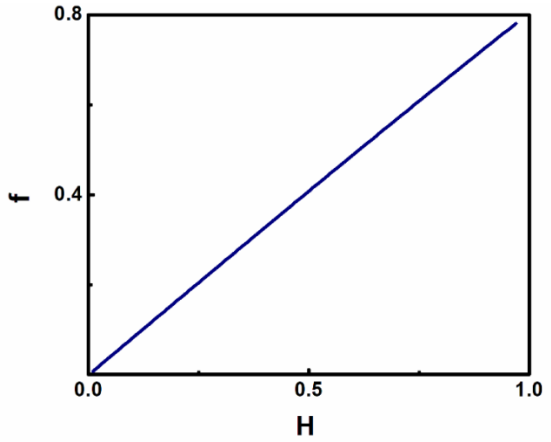

Figure 3.3: f versus H for (r/ξ)=1. f is the dimensionless lateral force, and for this value of (r/ξ) it is increasing with H.

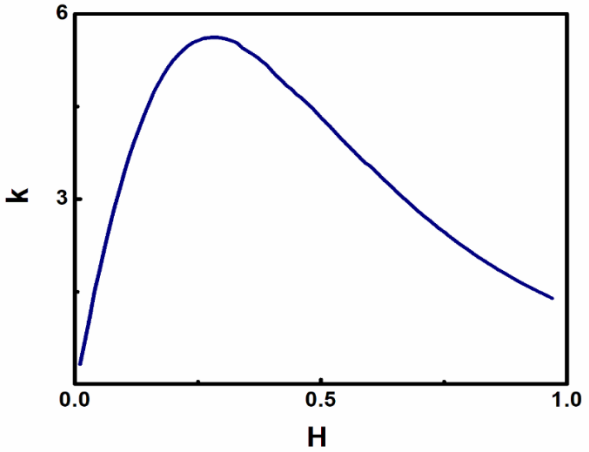

Figure 3.4: k versus H in the limit of r ≪ ξ. k is the dimensionless force constant and is not monotonic in H. it has a peak.

It is seen that k is not monotonic in H: it increases in H, reaches a maximum, and then decreases in H.

3.4 Conclusion

The lateral Casimir force between two self-affine rough plates was studied, using the pair wise summation method. The precision of the PWS method is good when the lateral correlation lengths are much larger than the separation between the two plates. The dependence of the lateral Casimir force on the lateral displacement of the two plates and the roughness exponent of the plates was investigated. It was seen that when the displacement is increased from zero, the lateral force increases and reaches a peak, and after that it decreases with increasing the displacement. The displacement at which this peak occurs is an increasing function of the roughness exponent. For small values of the displacement, the lateral Casimir force is linear with displacement. For large displacements, the lateral Casimir force behaves like the inverse of the 8 th power of the displacement. It is also seen that for appositive cross correlation between the plates (positive γ_{12}), the lateral Casimir force is repulsive for all displacements. This means that the point of no displacement (in which the lateral Casimir force is zero) is an unstable equilibrium when the correlation between the plates is positive.

References

[1] H.B.G. Casimir, Proc. K. Ned. Akad. Wet **51**, 793 (1948).
[2] T. Eming, A. Hanke, R. Golestanian, M. Kardar, Phys. Rev. Lett **87**, 260402 (2001).
[3] S.K. Lamoreaux, Phys. Rev. Lett **78**, 5 (1997).
[4] B.W. Harris, F. Chen, U. Mohideen, Phys. Rev. A **62**, 052109 (2000).
[5] T. Ederth, Phys. Rev. A **62**, 062104 (2000).
[6] G. Bressi, G. Carugno, R. Onofrio, G. Ruoso, Phys. Rev. Lett **88**, 041804 (2002).
[7] R.S. Decca, D. López, E. Fischbach, D.E. Krause, Phys. Rev. Lett **91**, 050402 (2003).
[8] U. Mohideen, A. Roy, Phys. Rev. Lett **81**, 4549 (1998).
[9] M.J. Sparnaay, Physica **24**, 751 (1958).
[10] V.B. Bezerra, G.L. Klimchitskaya, C. Romero, Mod. Phys. Lett. A **12**, 2613 (1997).
[11] F. Chen, U. Mohideen, Phys. Rev. Lett **88**, 101801 (2002).
[12] R. Golestanian, M. Kardar, Phys. Rev. Lett **78**, 18 (1997).
[13] M. Bordag, G.L. Klimchitskaya, U. Mohideen, V.M. Mostepanenko, Phys. Rev. A **69**, 044103 (2004).
[14] M. Bordag, G.L. Klimchitskaya, V.M. Mostepanenko, Int. J. Mod. Phys. A**10**, 2661 (1995).
[15] J. Krim, G. Palasantzas, Int. J. Mod. Phys. B **9**, 6 (1995).
[16] M. Bordag, G.L. Klimchitskaya, U. Mohideen, V.M. Mostepanenko, Advances in the Casimir Effect, Oxford University Press, New York, 2009.
[17] M. Bordag, U. Mohideen, V.M. Mostepanenko, Phys. Rep **353**, 1 (2001).
[18] V.M. Mostepanenko, N.N. Trunov, The Casimir Effect and its Applications, Oxford Clarendon Press, 1997.
[19] H.B.G. Casimir, D. Polder, Phys. Rev **73**, 360 (1948).
[20] G. Palasantzas, J. Barnas, J.Th.M. De Hosson, Acta Phys. Pol. A **97**, 495 (2000).
[21] Z.H. Ming, A.K. Rol, Y.L. Soo, Y.H. Kao, Phys. Rev. B **47**, 16373 (1993).
[22] D.G. Stearn, D.P. Gaines, D.W. Sweeney, J. Appl. Phys. **84**, 1003 (1998).
[23] T. Gu, A.I. Goldman, M. Mao, Phys. Rev. B **56**, 6474 (1997).
[24] G. Palasantzas, Phys. Rev. B **48**, 14472 (1993).
[25] R. Pynn, Phys. Rev. B **45**, 602 (1991).

Chapter 4

The effect of roughness and correlation on Casimir torque between two plates

Abstract. *The effect of roughness and correlation on the Casimir torque is studied. The plates are assumed to be perfect conductors. The pairwise summation (PWS) method is used, which is a good approximation when the correlation length is much larger than the distance between the plates. Torque components both parallel and perpendicular to the plates are obtained. It is seen that the component parallel to the plates is nonvanishing even if the plates are smooth, but there are contributions due to roughness and correlation as well, and the contribution of the correlation is an increasing function of both the roughness exponent and the correlation length. The component perpendicular to the plates, however, is nonvanishing only if the plates are rough and correlated to each other. As the roughness exponent increases, this component increases, reaches a peak and then decreases.*

This chapter has been published in :

F Tajik, M Khorrami, A A Masoudi, F Mohammad Dezashibi, “The effect of roughness and correlation on the Casimir torque between two plates”, *Int. J. Mod. Phys. B* .31, 1750258 (2017).

4.1 Introduction

Investigating Casimir phenomena is becoming more and more frequent recently. One motivation is the need to improve nano- or micro-technologies [1-8]. The Casimir effect is manifested, among other things, as an attraction between two parallel plates. This attractive force (F) is given by [9]:

$$F_{Cas} = \frac{\pi^2 \hbar c A}{240\, d^4}, \tag{4.1}$$

where d is the separation of the plates and A is the surface area of each plate. This effect is the result of the fact that the vacuum energy of the fields in a bounded region does depend on the boundaries [10]. Casimir effects are very small, unless the separations are tiny, so Casimir effects are important only in micro or nano-scales. But in such scales the surfaces are not completely smooth and their roughness does affect Casimir phenomena [11].

Many experimental works have been carried out regarding Casimir effects, among which are Refs. 12-18. In Refs. 19 and 20, among other things, the effect of patterned plates on the Casimir effect has been addressed. In Ref. 21, it has been shown that introducing roughness increases the component of the Casimir force which is perpendicular to the plates. In Ref. 22, the effect of roughness on the lateral Casimir force is studied. There are many works on the Casimir torque between two plates as well, among which are Refs. 23-31. In Ref. 24, 28 and 29, the Casimir torque is studied which arises in periodic systems with broken rotational symmetry. Others have investigated the Casimir torque in optically anisotropic materials, where the Casimir torque originates from the misalignment between two optical axes [30,31].

Here the Casimir torque between two parallel rough plates is studied. The plates are assumed to be perfect conductors. This is a good approximation when the separation between plates is not too small, say larger than a micron [32]. For our purpose the pairwise summation (PWS) method is used to obtain the Casimir energy corresponding to the two plates, as a function of the orientation of the plates. The pairwise summation method is based on the approximation that the Casimir energy between two thick plates is a summation of contributions of pairs of pieces (particles), where each pair consists of one element in each plate. The contribution of each pair is inversely proportional to the distance of its parts from each other, to the power seven. This method is accurate when the correlation lengths are much larger than the separation of the plates [9, 33, 35] and especially in the case where the bodies are ideal conductors. If the bodies are not ideal conductors, sometimes the nonadditive nature of the

Casimir phenomenon could be implemented by a so-called normalizing constant. Similar methods have been used to address such problems, for example, in Refs. 36-38. One can also relax the condition of infinite conductivity of the plates to be able to tackle more realistic situations, taking into account the optical properties of the materials. This is done through the Lifshitz model, for example, in Ref. 24.

Investigating the effect of roughness on the Casimir force or torque is important, especially in the nanoscale, where the effects themselves become important. A force or torque which is in the opposite direction of a displacement, means that things tend to stick to each other. This increases the frictional effects. On the other hand, a force or torque in the same direction tends to separate things from each other, which could serve as a mechanism for lowering the friction. As will be seen, the correlation between the roughness of the two plates affects the sign of the Casimir torque due to the roughness. The scheme of the paper is the following. In Sec. 4.2, the method and the model are introduced. In Sec. 4.3, the results are discussed. Section 4.4 is devoted to the concluding remarks.

4.2 The model

The system consists of two rough plates, approximately parallel with each other. The planes can rotate, and the rotations could be decomposed into rotations along an axis parallel to the plates and those along an axis perpendicular to the planes. For small angles of rotation, the rotation of the two plates is equivalent to just one plate rotating relative to the other. So it is assumed that the first plate is fixed while the other can rotate. The Casimir energy depends on the angles of rotation, and the derivative of this energy is the torque. The axis perpendicular to the first (fixed) plate is the z-axis. The first plate is located at z = 0, the second is located at z = d. The deviation of the height of the ith plate from its mean is denoted by h_i, which is a function of the horizontal position x. The average actual height (mean plus deviation) of the ith plate is denoted byZ_i. When the rotation is along an axis parallel to the plates, that axis is taken to be the y-axis. The plates are taken to be discs of radius R (surface areas $A = \pi R^2$), at a distance d from each other. One has:

$$\overline{h_1(\mathbf{x})} = 0 \tag{4.2}$$

where $\bar{X}$ is the ensemble average of X. Throughout this text, because of validity region for PWS and applying perturbation method for roughness (see chapter 2 Sect. 3),it is assumed that

$$|h_i| \ll d \tag{4.3}$$

$$d \ll \xi \tag{4.4}$$

$$\xi \ll R \tag{4.5}$$

where ξ is the correlation length corresponding to h_is, i.e., the in-plane correlation length of the deviations from the average heights. Figure 4.1 shows the schematic geometry of the plates and rotations.

i) Rotation along an axis parallel to the plates: The equations of the surfaces of the plates are

$$Z_1(\mathbf{x}) = h_1(\mathbf{x}) \tag{4.6}$$

$$Z_2(\mathbf{x}') = d + h_2(\mathbf{x}') + \theta\, \hat{\mathbf{x}}.\mathbf{x}' = d + \tilde{h}_2(\mathbf{x}') \tag{4.7}$$

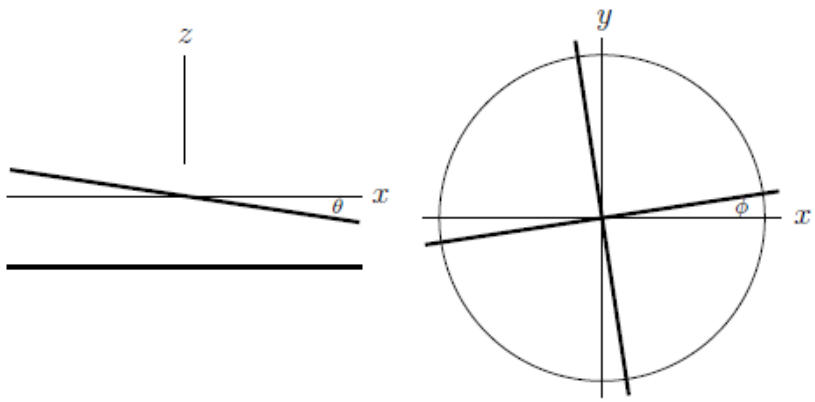

Figure 4.1: (a) Side view of the plates. The y-axis is perpendicular to the page. θ is the angle of rotation around y. (b) Plates seen from above. The z-axis is perpendicular to the page. φ is the angle of rotation around z.

where θ is the angle of rotation. The expression is up to first order in θ (valid for small values of θ). Here, the pairwise summation method is used to calculate

the Casimir energy. This method is the approximation that the Casimir energy between two thick plates is a summation of contributions of pairs of pieces, each consisting of one element in each plate. The contribution corresponding to each pair is inversely proportional to the distance of its parts from each other, to the power seven. The Casimir energy for two rough plates (see chapter 2 Sect. 3 Eq. 2.10) can be written as [39]:

$$\mathrm{E} = \frac{-\pi\hbar c}{24} \int \mathrm{d}^2x \ \mathrm{d}^2x' \ \varepsilon[\mathbf{x}-\mathbf{x}', \mathrm{h}_1(\mathbf{x}), \tilde{\mathrm{h}}_2(\mathbf{x})] =$$
$$-E_0 \ \sum_{m,n=1}^{\infty} \int \frac{\mathrm{d}^2x\prime}{\mathrm{A}} \ \frac{\mathrm{d}^2x}{\mathrm{d}^2} \ \alpha_{mn}(\mathbf{x}-\mathbf{x}') \ \frac{\tilde{h}_{\mathrm{mn}}(\mathbf{x},\mathbf{x}\prime)}{\boldsymbol{d^{m+n}}} \tag{4.8}$$

where the integration regions for $\mathbf{x}$ and $\mathbf{x}'$ are the whole lower and upper plates, respectively, and

$$\mathrm{E}_0 = \frac{\pi^2\hbar c A}{720\, \mathrm{d}^3}, \tag{4.9}$$

$$\tilde{\mathrm{h}}_{\mathrm{mn}}(\mathbf{x}) = \overline{\{[\mathrm{h}_1(\mathbf{x})]^{\mathrm{m}} \ \left[\tilde{\mathrm{h}}_2(\mathbf{x}')\right]^{\mathrm{n}}\}} \tag{4.10}$$

($-\mathrm{E}_0$) is the Casimir energy between two plates and α_{mn}s are the (dimension-less) coefficients of expansion of ε. The Casimir torque $\tau_{||}$ is related to the Casimir energy through

$$\tau_{||} = -\frac{\partial E}{\partial \theta} \tag{4.11}$$

For small angles, the Casimir energy can be expanded in θ, with the lowest θ-dependent term being quadratic in θ:

$$E = E^{(0)} + \ E_{||}^{(2)} \frac{\theta^2}{2} + \cdots \tag{4.12}$$

Hence,

$$\tau_{||} = -E_{||}^{(2)}\theta + \cdots, \tag{4.13}$$

with

$$\mathrm{E}_{||}^{(2)} = \ -E_0 \ \sum_{m,n=0}^{\infty} \int \frac{d^2x'}{A} \frac{d^2x}{d^2} \ \alpha_{m,n}(\boldsymbol{x}-\boldsymbol{x}') \times [n(n-1)](\hat{\boldsymbol{x}}.\boldsymbol{x}')^2 \ \frac{h_{m,n-2}(x,x')}{d^{m+n}} \tag{4.14}$$

where

$$h_{\mathrm{mn}}(\mathbf{x}) = \overline{\{[\mathrm{h}_1(\mathbf{x})]^{\mathrm{m}}\ [\mathrm{h}_2(\mathbf{x}')]^{\mathrm{n}}\}}. \tag{4.15}$$

Assuming the system to be homogeneous, $h_{\mathrm{mn}}(\mathbf{x},\mathbf{x}')$ would depend on only $(\mathbf{x}-\mathbf{x}')$. So, one can use $(\mathbf{x}-\mathbf{x}')$ instead of $\mathbf{x}$ as the integration variable, and perform the integration on x, the result would be

$$\mathrm{E}_{||}^{(2)} = -\frac{\mathrm{E}_0\,\mathrm{R}^2}{4\,\mathrm{d}^2}\sum_{\mathrm{m,n=0}}^{\infty}[\mathrm{n}(\mathrm{n}-1)]\int\frac{\mathrm{d}^2\mathrm{x}}{\mathrm{d}^2}\,\alpha_{\mathrm{m,n}}(\mathbf{x})\,\frac{\mathrm{h}_{\mathrm{m,n-2}}(\mathbf{x})}{\mathrm{d}^{\mathrm{m+n}}} \tag{4.16}$$

The first nonvanishing terms (up to the second order in roughness) read

$$\mathrm{E}_{||}^{(2)} = -\frac{\mathrm{E}_0\,\mathrm{R}^2}{2\,\mathrm{d}^2}\int\frac{\mathrm{d}^2\mathrm{x}}{\mathrm{d}^2}\left[\alpha_{0,2}(\mathbf{x}) + \frac{\sigma_1^2}{\mathrm{d}^2}\alpha_{2,2}(\mathbf{x}) + \frac{6\sigma_2^2}{\mathrm{d}^2}\alpha_{0,4}(\mathbf{x}) + \frac{3\mathrm{c}_{12}(\mathbf{x})}{\mathrm{d}^2}\alpha_{1,3}(\mathbf{x})\right] + \cdots \tag{4.17}$$

where σ_{i} shows the RMS roughness in the plate i and c_{12} is the cross-correlation function between two plates:

$$\overline{[\mathrm{h}_{\mathrm{i}}(\mathbf{x})]^2} = \sigma_i^2 \tag{4.18}$$

$$\overline{[\mathrm{h}_1(\mathbf{x})\mathrm{h}_2(\mathbf{x}')]} = \mathrm{c}_{12}(\mathbf{x}-\mathbf{x}'). \tag{4.19}$$

Also,

$$\alpha_{02}(\mathbf{x}) = \frac{15}{\pi}\frac{\mathrm{d}^7}{(\mathbf{x}^2+\mathrm{d}^2)^{\frac{7}{2}}} \tag{4.20}$$

$$\alpha_{22}(\mathbf{x}) = \frac{-105}{2\pi}\left[\frac{\mathrm{d}^9}{(\mathbf{x}^2+\mathrm{d}^2)^{\frac{9}{2}}} - 9\frac{\mathrm{d}^{11}}{(\mathbf{x}^2+\mathrm{d}^2)^{\frac{11}{2}}}\right] \tag{4.21}$$

$$\alpha_{04}(\mathbf{x}) = \frac{1}{6}\alpha_{22}(\mathbf{x}) \tag{4.22}$$

$$\alpha_{13}(\mathbf{x}) = \frac{-2}{3}\alpha_{22}(\mathbf{x}). \tag{4.23}$$

Assuming the plates to be homogeneous, σ_{i}s are constant. For the cross correlation [40-42]:

$$c_{12}(\mathbf{x}) = \gamma_{12}\sqrt{c_2(\mathbf{x})c_1(\mathbf{x})} \tag{4.24}$$

$$\gamma_{12} = \exp(-\frac{d}{\xi_\perp}) \tag{4.25}$$

where c_i is the autocorrelation function of the ith plate and $\xi_\perp$ is the vertical correlation length. For an isotropic system with self-affine roughness, the auto-correlation function is [43, 44]:

$$c_i(\mathbf{x}) = \sigma_i^2 \exp[-\left(\frac{d}{\xi_i}\right)^{2H_i}] \tag{4.26}$$

where ξ_i and H_i are correlation length and roughness exponent of the plate i. The roughness exponent H is a measure of the irregularity of the surface: a larger value for H corresponds to a smoother surface. Using these equations, one obtains

$$E_{||}^{(2)} = E_0^{(2)}\left[1 + 15\ \frac{\sigma_1^2+\sigma_2^2}{d^2}\left(1 - \frac{\sigma_1\sigma_2}{\sigma_1^2+\sigma_2^2}\gamma_{12}\,\chi_c\right)\right] + \cdots, \tag{4.27}$$

where $E_0^{(2)}$ corresponds to at plates, the remaining is the result of roughness of the plates, and χ_c corresponds to the contribution due to the cross-correlation between the plates:

$$E_0^{(2)} = -\frac{E_0\,R^2}{2\,d^2}\int\frac{d^2x}{d^2}\,[\alpha_{02}(\mathbf{x})] = -\frac{3E_0\,R^2}{d^2} \tag{4.28}$$

and

$$\chi_c = \frac{1}{\int\frac{d^2x}{d^2}\,[\alpha_{22}(\mathbf{x})]}\int\frac{d^2x}{d^2}\frac{\sqrt{c_1(x)\,c_2(x)}}{\sigma_1\,\sigma_2}\,\alpha_{22}(x). \tag{4.29}$$

For $\sigma_{1=}\sigma_2 = \sigma$, the expression for $E_{||}^{(2)}$ k is further simplified to

$$E_{||}^{(2)} = E_0^{(2)}\left[1 + 30\ \frac{\sigma^2}{d^2}\,(1 - \gamma_{12}\,\chi_c)\right] + \cdots \tag{4.30}$$

It is seen that for small values of θ, the torque is proportional to θ, with the proportionality constant being ($-E_{||}^{(2)}$). The torque is nonzero even for smooth plates, and is proportional to the square of the plates' size and inversely

proportional to their distance, as can be seen in Eq. 4.28. If the plates are rough, then a contribution of roughness is added to the torque. That contribution is further proportional to the mean square of roughness divided by the square of the distance between the plates. Finally, if the roughness of the plates are correlated, another contribution appears which is further proportional to the coherence parameter γ. These can be summarized in

$$\tau_{||0} \propto E_0 \frac{R^2}{d^2} \tag{4.31}$$

$$\tau_{||\text{rough}} \propto E_0 \frac{R^2}{d^2} \frac{\sigma^2}{d^2} \tag{4.32}$$

$$\tau_{||\text{correlated}} \propto E_0 \frac{R^2}{d^2} \frac{\sigma^2}{d^2} \gamma \tag{4.33}$$

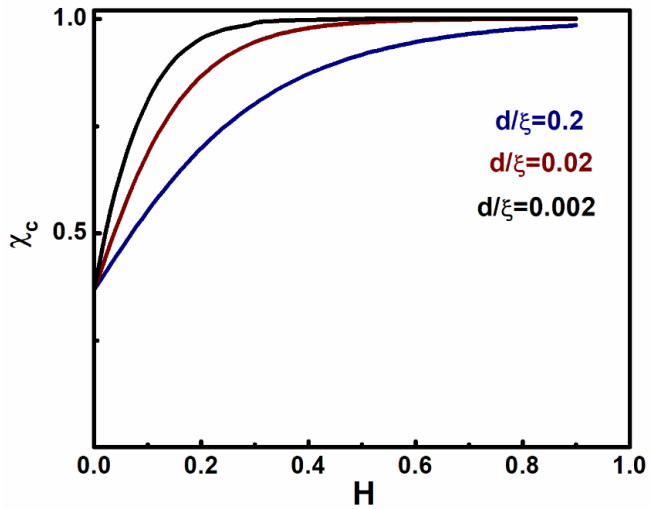

Figure 4.2: χ_c (an indicator of the effect of cross-correlation on the torque constant for rotations around an axis parallel to the plates) versus H (the roughness exponent), for some values of (d/ξ). The values of (d/ξ) are indicated on the curves.

The proportionality constant in the last relation is $(-90\chi_c)$ and χ_c has been plotted in Fig. 4.2. As the torque is proportional to E_0 and the square of the size of the plates, and E_0 itself is proportional to the area of the plates, the torque is proportional to the square of the area of the plates.

ii) Rotation along an axis perpendicular to the plates: The equations of the surfaces of the plates are

$$Z_1(\mathbf{x}) = h_1(\mathbf{x}) \tag{4.34}$$

$$Z_2(\mathbf{x}') = d + h_2(U^{-1}\mathbf{x}') \tag{4.35}$$

$$U\mathbf{x}' = x' + \varphi\,\hat{\boldsymbol{z}} \times \mathbf{x}' - \frac{\varphi^2}{2}\mathbf{x}' + \cdots \tag{4.36}$$

where φ is the angle of rotation. The energy between the two rough plates, the Casimir-Polder energy equation, reads

$$\begin{aligned} E &= \frac{-\pi\hbar c}{24}\int d^2x\; d^2x'\; \varepsilon[\mathbf{x}-\mathbf{x}', h_1(\mathbf{x}), h_2(U^{-1}\mathbf{x}')] = \\ &: \frac{-\pi\hbar c}{24}\int d^2x\; d^2x'\; \varepsilon[\mathbf{x}-U\mathbf{x}', h_1(\mathbf{x}), h_2(\mathbf{x}')] = \\ &-E_0\sum_{m,n=1}^{\infty}\int \frac{d^2x'}{A}\frac{d^2x}{d^2}\,\alpha_{m,n}(\mathbf{x}-U\mathbf{x}')\,\frac{h_{m,n}(\mathbf{x},\mathbf{x}')}{d^{m+n}} \end{aligned} \tag{4.37}$$

The Casimir torque τ is related to the Casimir energy through

$$\tau = -\frac{\partial E}{\partial \varphi} \tag{4.38}$$

For small angles, the Casimir energy can be expanded in φ, with the lowest φ dependent term being quadratic in φ:

$$E = E^{(0)} + E_{\perp}^{(2)}\frac{\varphi^2}{2} + \cdots \tag{4.39}$$

Hence

$$\tau_{\perp} = -E_{\perp}^{(2)}\varphi + \cdots \tag{4.40}$$

One has

$$\begin{aligned} E_{\perp}^{(2)} = -E_0\sum_{m,n=0}^{\infty}\int \frac{d^2x'}{A}\frac{d^2x}{d^2} \times \{\big[(\mathbf{x}')^i\,\partial_i + (\hat{\boldsymbol{z}} \times \mathbf{x}')^i(\hat{\boldsymbol{z}} \times \\ \mathbf{x}')^j\;\partial_i\;\partial_j\big]\,\alpha_{m,n}\}\,(\mathbf{x}-\mathbf{x}')\frac{h_{m,n}(\mathbf{x},\mathbf{x}')}{d^{m+n}} \end{aligned} \tag{4.41}$$

Assuming the system to be homogeneous, $h_{m,n}(\mathbf{x},\mathbf{x}')$would depend on only $(\mathbf{x}-\mathbf{x}')$. So, one can use $(\mathbf{x}-\mathbf{x}')$ instead of **x** as the integration variable, and perform the integration on x, the result would be

$$E_{\perp}^{(2)} = -\frac{E_0 R^2}{2 d^2} \sum_{m,n=0}^{\infty} \int \frac{d^2x}{d^2} (\nabla^2 \alpha_{m,n})(\mathbf{x}) \frac{h_{m,n}(\mathbf{x})}{d^{m+n}} \tag{4.42}$$

The first nonvanishing term reads

$$E_{\perp}^{(2)} = -\frac{E_0 R^2}{2 d^2} \int \frac{d^2x}{d^2} (d^2 \nabla^2 \alpha_{11})(\mathbf{x}) \frac{c_{12}(\mathbf{x})}{d^2} + \cdots \tag{4.43}$$

So,

$$E_{\perp}^{(2)} = -\frac{E_0 R^2}{2 d^2} \gamma_{12} \frac{\sigma_1 \sigma_2}{d^2} (d^2 \nabla^2 \alpha_{11})(0) \chi_{\perp} + \cdots \tag{4.44}$$

Where

$$\chi_{\perp} = \frac{1}{(d^2 \nabla^2 \alpha_{11})(0)} \int \frac{d^2x}{d^2} \frac{\sqrt{c_1(x)\, c_2(x)}}{\sigma_1\, \sigma_2} (d^2\, \nabla^2 \alpha_{11})(x) \tag{4.45}$$

Using

$$\alpha_{11}(\mathbf{x}) = \frac{-30}{\pi} \frac{d^7}{(\mathbf{x}^2 + d^2)^{\frac{7}{2}}} \tag{4.46}$$

one arrives at

$$(d^2 \nabla^2 \alpha_{11})(\mathbf{x}) = \frac{-210}{\pi} \frac{d^9 (7\mathbf{x}^2 - 2d^2)}{(\mathbf{x}^2 + d^2)^{\frac{11}{2}}} \tag{4.47}$$

$$(d^2 \nabla^2 \alpha_{11})(0) = \frac{420}{\pi} \tag{4.48}$$

Using these, for $\sigma_{1=}\sigma_2 = \sigma$, the expression for $E_{\perp}^{(2)}$ is further simplified to

$$E_{\perp}^{(2)} = -\frac{420}{\pi} \frac{E_0 R^2}{2 d^2} \gamma_{12} \frac{\sigma^2}{d^2} \chi_{\perp} + \cdots \tag{4.49}$$

It can be seen that the component of torque, which is perpendicular to the plates, is nonzero only if the plates are rough and their roughness are correlated to each other. Again, for small values of φ, the torque is proportional to φ, with the proportionality constant being ($E_{\perp}^{(2)}$). This proportionality constant is propor-

tional to the square of the plates' size, the mean square roughness and the coherence parameter, and is inversely proportional to the distance of the plates to the power 4, as seen in Eq. 4.49. The remaining factor is $(210\chi_{\perp}/\pi)$. Figure 4.3 is the plot of $\chi_{\perp}$.

The dependence of this torque on the size of the system, separation of the plates, the mean square roughness and the coherence parameter is similar to the contribution of the correlation of the plates on the torque component parallel to the plates; among other things, it is proportional to the square of the area of the plates.

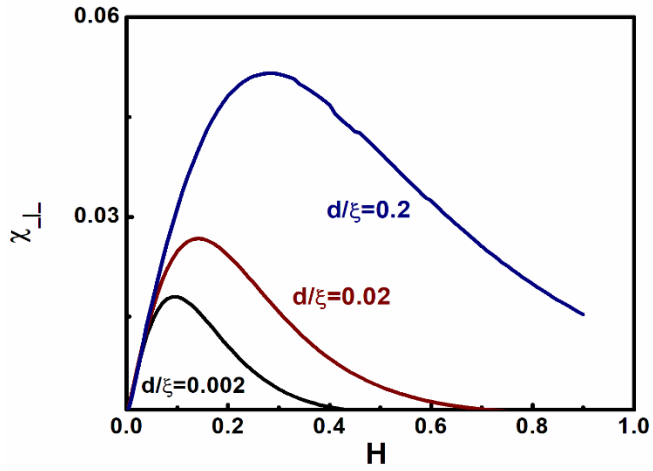

Figure 4.3: $\chi_{\perp}$ (an indicator of the torque constant for rotations around an axis perpendicular to the plates) versus H (the roughness exponent), for some values of (d/ξ). The values of (d/ξ) are indicated on the curves.

However, $\chi_{\perp}$ is not an increasing function of H. Its maximum value for fixed (d/ξ) is denoted by $\chi_{\perp m}$. This value of $\chi_{\perp}$ is attained at $H = H_m$. H_m and $\chi_{\perp m}$ depend on (d/ξ), and are plotted in Figs. 4.4 and 4.5, respectively.

4.3 Results and discussion

The explicit form of the Green functions can be easily found for two parallel plates The graphs are for the case $\sigma_{1=}\sigma_2 = \sigma$. Figures 4.2 and 4.3 show χ_c and $\chi_{\perp}$, respectively, versus H, for some values of (d/ξ). Figure 4.2 shows that the contribution of correlation to the torque component parallel to the plates is increasing with respect to both the roughness exponent and the correlation length.

One can also extract the following asymptotic behaviors for small and large values of H:

$$\chi_c = \frac{1}{e}\left[1 - H\left(2\ln\frac{2d}{\xi} - \frac{17}{5}\right)\right] + \cdots \tag{4.50}$$

$$\chi_c = 1 + \frac{1}{6}\left[1 + \left(\frac{\xi}{d}\right)^2\right]^{\frac{-7}{2}} - \frac{7}{6}\left[1 + \left(\frac{\xi}{d}\right)^2\right]^{\frac{-9}{2}} + \cdots \quad \text{for large H} \tag{4.51}$$

Figure 4.3 shows that the torque component perpendicular to the plates decreases with the correlation length. Regarding the roughness exponent, however, as the roughness exponent increases it first increases, then reaches a maximum and then decreases. The asymptotic behavior is

$$\chi_\perp = \frac{2\pi}{7e} H + \cdots \tag{4.52}$$

$$\chi_\perp = \pi\left\{\left[1 + \left(\frac{\xi}{d}\right)^2\right]^{\frac{-7}{2}} - \left[1 + \left(\frac{\xi}{d}\right)^2\right]^{\frac{-9}{2}}\right\} + \cdots \quad \text{for large H} \tag{4.53}$$

In fact, Figure 4.4 shows H_m (the value of H which maximizes $\chi_\perp$) as a function of (d/ξ), and Figure 4.5 shows $\chi_{\perp m}$ (the maximum value of $\chi_\perp$) as a function of (d/ξ).

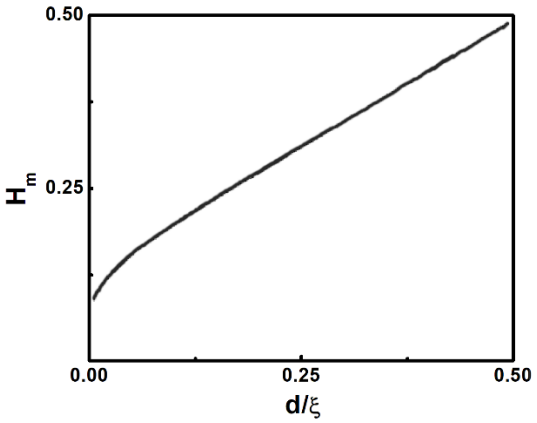

Figure 4.4: H_m(the value of H which maximizes $\chi_\perp$) versus (d/ξ).

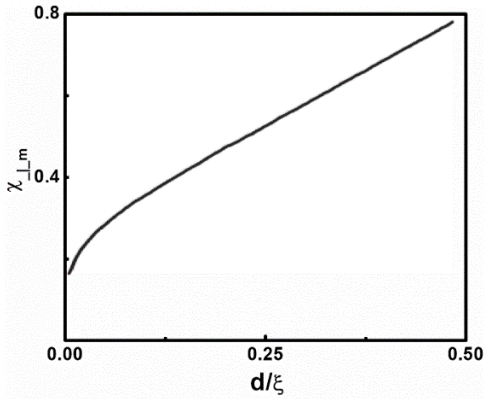

Figure 4.5: $\chi_{\perp m}$ (the maximum value of $\chi_{\perp}$) versus (d/ξ).

4.4 Conclusions

The effect of self-affine roughness on the Casimir torque was studied using the PWS method. This method is accurate when the distance between the plates is much less than the correlation length. Two components of the torque were studied. It was seen that for the component parallel to the plates, there is a nonzero part even if the planes are smooth. The effect of the correlation between the plates increases when the roughness index increases or when the correlation length increases. The component perpendicular to the plates is nonvanishing only if there is a correlation between the two plates. This component, as a function of the roughness exponent, increases, reaches a peak and then decreases.

The effect of roughness on the torque is particularly important for the component of the torque which is normal to the plates, as this component vanishes in the absence of roughness. The fact that this component has a peak as a function of the roughness exponent means that, for example, one could tune the roughness exponent to reach that maximum, or avoid that maximum. A maximum positive torque means that the plates do not get stuck to each other, and this would be important if large frictions are to be avoided.

References

[1] P. Meakin, Phys. Rep. **235**, 1991 (1993).
[2] F. Capasso et al., IEEE J. Sel. Top. Quant. Electron. **13**, 400 (2007).
[3] R. Esquivel-Sirvent, M. A. Palomino-Ovando and G. H. Cocoletzi, Appl. Phys. Lett. **95**, 051909 (2009).
[4] A. W. Rodriguez, F. Capasso and S. G. Johnson, Nat. Photon. **5**, 211 (2011).
[5] P. Ball, Nature **447**, 772 (2007).
[6] M. Sedighi et al., J. Phys.: Condens. Matter. **27**, 214014 (2015).
[7] M. Sedighi and G. Palasantzas, Appl. Phys. Lett. **117**, 144901 (2014).
[8] W. H. Broer, G. Palasantzas and V. B. Svetovoy, Phys. Rev. B **87**, 125413 (2013).
[9] H. B. G. Casimir, Proc. K. Ned. Akad. Wet **51**, 793 (1948).
[10] T. Eming et al., Phys. Rev. Lett. **87**, 260402 (2001).
[11] G. Palasantzas, J. Appl. Phys. **97**, 126104 (2005).
[12] S. K. Lamoreaux, Phys. Rev. Lett. **78**, 5 (1997).
[13] B. W. Harris, F. Chen and U. Mohideen, Phys. Rev. A **62**, 052109 (2000).
[14] T. Ederth, Phys. Rev. A **62**, 062104 (2000).
[15] G. Bressi et al., Phys. Rev. Lett. **88**, 041804 (2002).
[16] R. S. Decca et al., Phys. Rev. Lett. **91**, 050402 (2003).
[17] U. Mohideen and A. Roy, Phys. Rev. Lett. **81**, 4549 (1998).
[18] M. J. Sparnaay, Physica **24**, 751 (1958).
[19] M. Tröndle, L. Harnau and S. Dietrich, J. Chem. Phys. **129**, 124716 (2008).
[20] A. Gambassi and S. Dietrich, Soft Matter. **7**, 1247 (2011).
[21] V. B. Bezerra, G. L. Klimchitskaya and C. Romero, Mod. Phys. Lett. A **12**, 2613 (1997).
[22] F. Tajik, A. A. Masoudi and M. Khorrami, Physica B **485**, 116 (2016).
[23] W. Long and L. Schuermann, arXiv:1310.1421 [hep-th].
[24] R. Guerout et al., Europhys. Lett. **111**, 4 (2015).
[25] F. Intravaia et al., Nat. Commun. **4**, 2515 (2013).
[26] M. Imboden et al., J. Appl. Phys. **116**, 134504 (2016).
[27] M. Shahzamani, M. Amini and M. Soltani, Eur. Phys. J. D **71**, 13 (2017).
[28] R. B. Rodrigues et al., J. Phys. A **41**, 164004 (2008).
[29] R. B. Rodrigues et al., Europhys. Lett. **76**, 822 (2006).
[30] T. G. Philbin and U. Leonhardt, Phys. Rev. A **78**, 042107 (2008).
[31] X. Chen and J. C. H. Spence, Phys. Status Solidi A **210**, 9 (2013).
[32] V. B. Svetovoy and G. Palasantzas, Adv. Colloid Interface Sci. **216**, 1 (2015).
[33] M. Bordag et al., Advances in the Casimir Effect (Oxford University Press, New York, 2009).
[34] M. Bordag, U. Mohideen and V. M. Mostepanenko, Phys. Rep. **353**, 1 (2001).
[35] V. M. Mostepanenko and N. N. Trunov, The Casimir Effect and Its Applications (Clarendon Press, Oxford, 1997).
[36] V. N. Marachevsky, Phys. Scripta. **64**, 205 (2001).
[37] P. Barcellona and R. Passante, Ann. Phys. **355**, 282 (2015).
[38] A. F. Bitbol et al., Phys. Rev. B **87**, 045413 (2013).

[39] H. B. G. Casimir and D. Polder, Phys. Rev. **73**, 360 (1948).
[40] Z. H. Ming et al., Phys. Rev. B **47**, 16373 (1993).
[41] D. G. Stearn, D. P. Gaines and D. W. Sweeney, J. Appl. Phys. **84**, 1003 (1998).
[42] T. Gu, A. I. Goldman and M. Mao, Phys. Rev. B **56**, 6474 (1997).
[43] G. Palasantzas, Phys. Rev. B **48**, 14472 (1993).
[44] R. Pynn, Phys. Rev. B **45**, 602 (1991).

Chapter 5

Sensitivity on materials optical properties of single beam torsional Casimir actuation

Abstract. *Here we investigate the dynamical sensitivity of electrostatic torsional type micro electromechanical systems (MEMS) on the optical properties of interacting materials. This is accomplished by considering the combined effect of mechanical Casimir and electrostatic torques to drive device actuation. The bifurcation curves and the phase portraits of the actuation dynamics have been analyzed to compare the sensitivity of a single beam torsional device operating between materials with conductivities that differ by several orders of magnitude. It is shown that the range of stable operation of torsional MEMS against stiction instabilities can increase by decreasing the conductivity of interacting materials. Moreover, the introduction of controlled dissipation, corresponding to a finite quality factor, in an otherwise unstable torsional system, could alter an unstable motion towards stiction to dissipative stable motion.*

This chapter has been published in :

F Tajik, M Sedighi, G Palasantzas," Sensitivity on materials optical properties of single beam torsional Casimir actuation", *J. Appl. phys* 121, 174302 (2017).

5.1 Introduction

Nowadays the improvement micro/nanofabrication technologies has given strong impetus to device architectures deep into submicron length scales, where Casimir forces between components inevitably will play significant role on their actuation dynamics [1-4]. These interactions between two objects arise due to perturbation of quantum fluctuations of the EM field [4, 5], as it was predicted by H. Casimir in 1948 [6] assuming two perfectly conducting parallel plates. A few years later Lifshitz and co-workers in the 50's [7] considered the general case of real dielectric plates by exploiting the fluctuation-dissipation theorem, which relates the dissipative properties of matter (via optical absorption by many microscopic dipoles) and the resulting EM fluctuations. This theory describes the attractive interaction due to quantum fluctuations for all separations covering both the Casimir (long-range) and van der Waals (short-range) regimes [1, 7, 8]. In any case, the dependence of the Casimir force on materials is an important topic since in principle one can tailor the force by suitable choice of materials [9-16].

Casimir forces could have strong technological potential for micro/nanoelectromechanical systems (MEMS/NEMS) such as switches, accelerometers, quantum levitation systems etc., because they have surface areas large enough but gaps small enough for the force to draw components together, and affect their actuation dynamics [1-4]. On the other hand the strong dependence of the Casimir force on the material optical properties [9-16] can be utilized to tune the actuation of devices. Although, metals give strong Casimir forces due to the high absorption of conduction electrons in the infrared range, other materials with less conductivity but suitable for operation in harsh environments can also be used in actuating components [17]. Therefore, a suitable choice of materials could open a multitude of opportunities for device engineering, and increase operation yield of these devices.

Furthermore, the broken symmetry in periodic MEMS has also attracted strong interest for contactless motion transmission. Indeed, when the translation symmetry is broken along two parallel periodic plates, it leads to creation of lateral Casimir forces [4, 19, 20]. Moreover, a Casimir torque can arise in systems with broken rotational symmetry [21-23]. The Casimir torque has also been investigated in optically anisotropic materials, where the torque originates from misalignment between the optical axes of the interacting plates [24-27]. Nonetheless, the Casimir torque due to broken rotational symmetry is stronger than that in anisotropic systems [22]. In addition, a mechanical torque can arise in torsional electrostatic actuators due to the normal Casimir force [28-32]. The torsional actuator is constructed from two electrodes, one of which

is fixed and the other is able to rotate around an axis. By applying a voltage between two electrodes the moving electrode can rotate because of the electrostatic force, while at a certain voltage the rotating electrode can become unstable and collapse on the fixed one [33]. This dynamical behavior has been studied extensively in parallel-plate and sphere-plate geometries [17, 18, 34-38] by considering interaction between materials with measured optical properties.

On the other hand, the dynamics of torsional electrostatic actuator was studied by considering the effect of van der Waals forces without including taking into account measured optical properties [31, 39]. So far, however, the effect of the influence of the Casimir force on dynamical behavior of torsional actuators made of materials with different optical properties still remains unexplored. In addition, torsional oscillators have been used for the measurement of the Casimir force [8, 28, 40] underlying the importance of this type of MEMS in table top cosmology to probe fundamental physics. Therefore, a realistic analysis of torsional dynamics will be performed here, where the mechanical torque due to the Casimir forces will be considered, using the measured optical properties of materials with diverse conductivities over several orders of magnitude, as input to the Lifshitz theory.

5.2 Influence of optical properties on Casimir forces

In principle, the Lifshitz theory is applicable at any temperature, to any Prior to modeling the torsional system and its actuation dynamics, we will present briefly the Lifshitz theory, which will be necessary for the calculation of the torsional Casimir torques, and illustrate the influence of different material optical properties that will be used in this study. Indeed, we consider here Au [15], which is good metal conductor and has been used in torsional devices [8, 40], and nitrogen doped SiC, which is a poor conductor but suitable for operation in harsh environments and well integrated in Si-based MEMS technologies [17, 36]. The imaginary parts $\varepsilon''(\omega)$ of the measured frequency dependent dielectric response function $\varepsilon(\omega)$ of Au and SiC, and the corresponding functions at imaginary frequencies $\varepsilon(i\xi)$ are shown in Figure 5.1. The ratio ω_p^2/ω_τ as obtained from the analysis of the optical data shown in Figure 5.1 [15, 17] which yields the sample conductivity $\sigma = (\omega_p^2/\omega_\tau)/4\pi$. For SiC we have obtained ${\omega_p}^2/\ \omega_\tau|_{SiC} = 0.4$ eV [17], and for Au ${\omega_p}^2/\ \omega_\tau|_{Au} \approx 1600$ eV [15]. These values indicate a conductivity contrast for Au/SiC more than three orders of magnitude. Moreover, significant differences in $\varepsilon(i\xi)$ for Au and SiC appear

for frequencies ξ<1 eV, which will manifest to differences in the Casimir force for separations c/2ξ>10 nm.

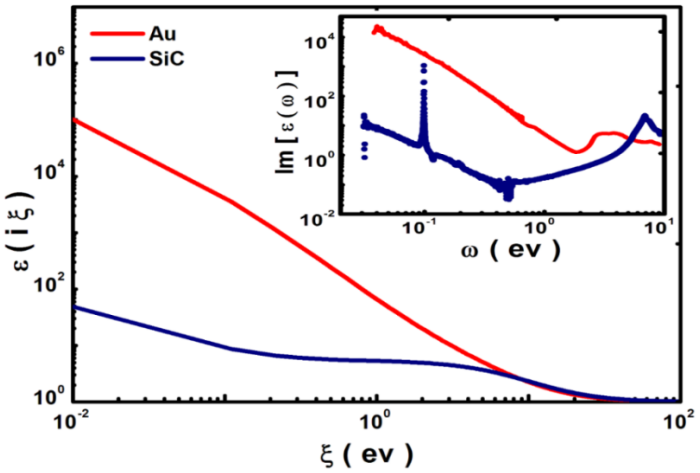

Figure 5.1: dielectric functions $\varepsilon(i\xi)$ are calculated using the Drude model for Au and conductive SiC. Here we use the data for Au from the sample 3 in [15]. The inset shows the imaginary part $\varepsilon''(\omega)$ of the frequency-dependent dielectric function measured with ellipsometry.

The non-measurable dielectric function $\varepsilon(i\xi)$ is the necessary input for Eq. 2.30 which is the calculation of the Casimir force via Lifshitz theory between two parallel plates at separation d and finite temperature (see chapter 2, Sect. 2.7)

5.3 Actuation dynamics theory for single beam torsional MEMS

Here we consider the electrostatic torsional actuator shown in Figure 5.2, where only the upper plate can rotate without any buckling due to the applied torques. This is a cantilever type motion that applies in the limit where the cantilever does not elastically deform because we assume large beam lengths (L_x) and small torsional angles at maximum separation ($d/L_x \ll 1$). It is assumed that both plates are coated with an optically bulk coating of Au or SiC (thicknesses > 100 nm) [15, 17].

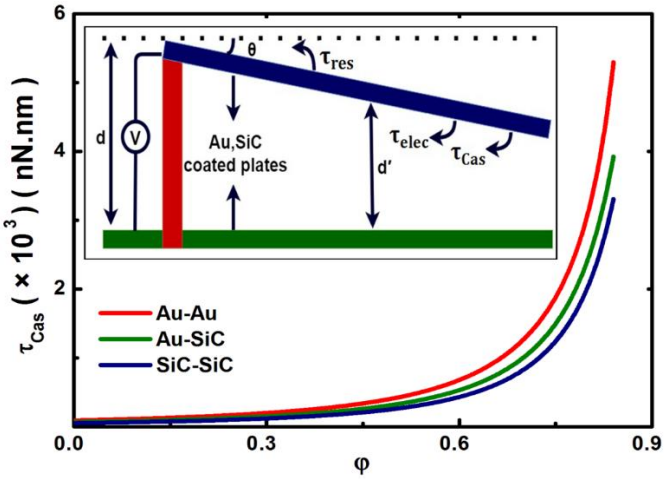

Figure 5.2: Casimir torques calculated for different pairs of materials (Au-Au, Au-SiC, SiC-SiC) using as input the optical data from Figure 5.1. $\varphi = \theta/\theta_0$ is the normalized torsional angle with respect to the maximum angle $\theta_0 = d/L_x$. The inset shows Schematics of the torsional MEM system at initial separation $d = 200\,nm$ with the corresponding acting torques indicated

The initial distance when the plates are parallel is assumed to be d=200 nm, and the system temperature T=300 K. When a voltage V is applied between the two electrodes, the electrostatic torque will rotate the moving plate. If we denote with θ the torsional angle, the electrostatic torque is given by [31, 39]

$$\tau_{elec} = \frac{1}{2}\varepsilon_0 L_y v^2 \frac{1}{\sin^2(\theta)}\left[\ln\left(\frac{d - L_x \sin(\theta)}{d}\right) + \frac{L_x \sin(\theta)}{d - L_x \sin(\theta)}\right], \tag{5.1}$$

where L_x and L_y are length and width of each plate respectively (here we consider $L_x = L_y = 10$ μm), and ε_0 is the permittivity of vacuum. Any rotation of the beam will generate a torsional restoring torque

$$\tau_{res} = k\theta \tag{5.2}$$

with k the torsional spring constant around the support point allowing rotation of the beam [8, 28, 40, 41]. Besides the electrostatic and restoring torques, a mechanical Casimir torque will also act on the rotating beam pulling it towards the fixed plate. If we apply the proximity force approximation (PFA), where one takes the summation from all area strips $L_y\,dr$ contributing a torque $rF_{Cas}(d')L_y\,dr$ (with $d' = d - r\sin\theta$) [32, 42], which is given by [31,39]

$$\tau_{Cas} = \int_0^{L_x} r F_{Cas}(d') L_y \, dr \,, \tag{5.3}$$

Here we consider for simplicity flat plates because at short separations (<100 nm) nanoscale roughness can also have significance influence [34, 38, 43]. Eq. 5.3 is approximate because we assume summation of the mechanical Casimir torques using Eq. 5.1 and for small torsion angles θ (<<1). The latter condition is satisfied since $\theta \leq \theta_0 \ (= d/L_x) = 0.02$. Calculations of Casimir torques for Au and SiC coated plates are shown in Figure 5.2, where the mechanical torque is stronger for the Au-Au system due to higher absorption of conduction electron in the infrared range (considering the Drude model to extrapolate at low frequencies where the optical measurements are not available, see chapter 2, Sect. 2.8).

If we now consider all acting torques on the moving plate, then the equation of motion for torsional system reads of the form

$$I_0 \frac{d^2\theta}{dt^2} + I_0 \frac{\omega}{Q} \frac{d\theta}{dt} = -\tau_{res} + \tau_{elec} + \tau_{Cas}, \tag{5.4}$$

where I_0 is the moment of inertia. The second term at the right hand of Eq.5.4 is the intrinsic energy dissipation of the moving plate with Q the quality factor of the MEM system. In the following we will consider high quality factors (unless it is stated otherwise) $Q \geq 10^4$ [44], so that we can neglect the effect of this term. The frequency ω is assumed to be typical for many resonators like AFM cantilever, and MEMS [8, 28, 40, 44].

5.4 Results and discussion

Our goal is to find out under what conditions there is a periodic solution for the torsional system, which it will indicate that the restoring torque is strong enough to prevent collapsing of the rotating plate onto the fixed plate. For this purpose we introduce the bifurcation parameter $\delta_{Cas} = \tau_{Cas}^m / k\theta_0$ that represents the ratio of the minimal Casimir torque $\tau_{Cas}^m = \tau_{Cas}(\theta = 0)$, and the maximum restoring torque $k\theta_0$. A small change in δ_{Cas} can lead to an abrupt change in the actuation of the MEM system [18, 45]. Using δ_{Cas}, Eq. 5.3 obtains the more convenient form

$$I \frac{d^2\varphi}{dt^2} = -\varphi + \delta_v \frac{1}{\varphi^2}\left[\ln(1-\varphi) + \frac{\varphi}{1-\varphi}\right] + \delta_{Cas}\left[\frac{\tau_{cas}}{\tau_{Cas}^m}\right], \tag{5.5}$$

with $\varphi = \theta/\theta_0$, $I = I_0/k$, and $\delta_v = (\varepsilon_0\, V^2\, L_y\, L_x^3)/(2kd^3)$ the bifurcation parameter for the electrostatic force [30, 35]. The equilibrium points of Eq. 5.5 correspond to $\tau_{total}(= -\tau_{res} + \tau_{elec} + \tau_{Cas}) = 0$ and $d\tau_{total}/d\varphi = 0$. As a result we obtain from Eq. 5.5

$$-\varphi + \delta_v \frac{1}{\varphi^2}\left[\ln(1-\varphi) + \frac{\varphi}{1-\varphi}\right] + \delta_{Cas}\left[\frac{\tau_{cas}}{\tau_{Cas}^m}\right] = 0. \tag{5.6}$$

5.4.1 Strongest Casimir torque system: Au-Au

Figure 5.3(a) shows plot of δ_{Cas} vs. φ for the case of Au-Au system that has the strongest Casimir torque, and different applied voltages V or equivalently different bifurcation parameters δ_v. The maximum of δ_{Cas} decreases with increasing of δ_v. For a specific voltage, if the restoring torque is strong enough so that $\delta_{Cas} < \delta_{Cas}^{MAX}$, then there are two equilibrium points. The stationary points near to $\varphi = 0$ are stable centers for which periodic solutions exist around them, while the other ones close to $\varphi = 1$ are unstable saddle points. In the latter case, the torsional system is unstable during oscillation around these points due to the stronger Casimir torque leading to collapse of the moving plate on the fixed plate, a situation known as stiction.

This can also be demonstrated by plotting δ_v versus φ, as it is shown in Figure 5.3(b) for different values of δ_{Cas}. The lowest diagram in this figure is for the case of the maximum $\delta_{Cas} = 0.14$ (for V=0 in Figure 5.3(a)), and it implies that if $\delta_{Cas} > 0.14$ the torsional system will lose its stability even in the absence of any applied voltage due the strong Casimir torque. And also for $0 < \delta_{Cas} < 0.14$ and $\delta_v > 0$, there two equilibrium points in Figure 5.3(b) as it was discussed for Figure 5.3(a). The critical saddle points, where the motion becomes unstable, satisfy the additional condition $d\tau_{total}/d\varphi = 0$. The latter yields from Eq. 5.4 the second condition for δ_{Cas} and δ_v

$$-1 + \delta_v\left[\frac{2\varphi - 3}{\varphi^2(1-\varphi)^2} + \frac{2\ln(1-\varphi)}{\varphi^3}\right] + \delta_{Cas}\frac{1}{\tau_{Cas}^m}\left(\frac{d\tau_{Cas}}{d\varphi}\right) = 0. \tag{5.7}$$

Besides the bifurcation analysis, the dynamics of the torsional system can be illustrated by the aid of the phase portraits that show the angular velocity $d\varphi/dt$ vs. the rotation angle φ [46]. Indeed, in Figure 5.3(c) we show the phase portraits around the sable and saddle points for the case $\delta_v = 0$ (V=0) of Figure 5.3(b). Any solution with initial conditions within the homoclinic orbit that goes through the unstable saddle point (squares in Figure 5.3(c)) will lead to stable

motion, while for any other initial conditions outside the homoclinic orbit the upper plate will perform unstable motion leading to collapse on the fixed plate. The periodic solutions indicate that the restoring torque is strong enough to keep system in operation and avoid any stiction instabilities.

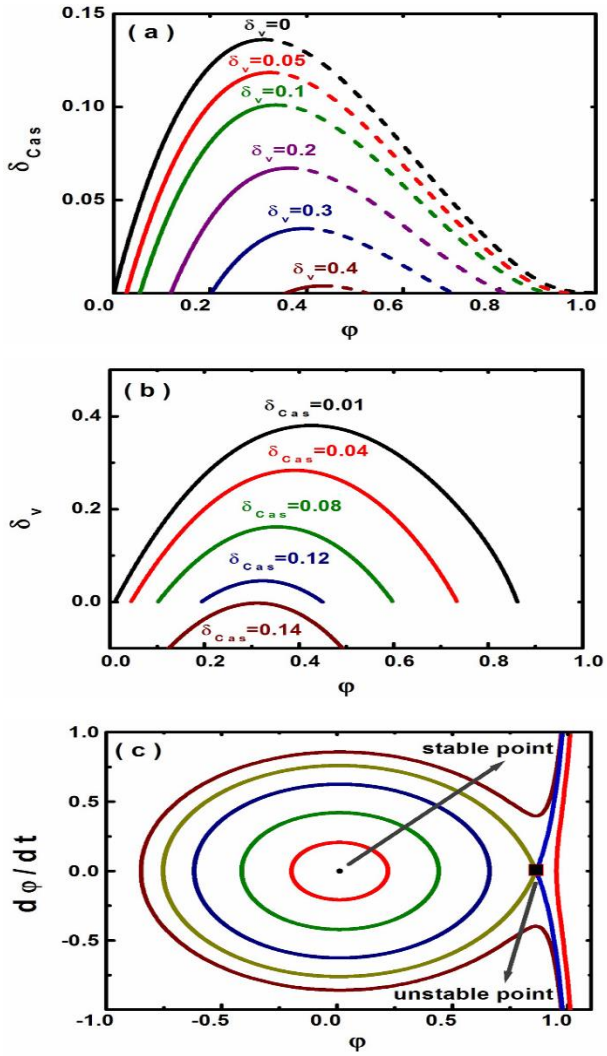

Figure 5.3: (a) Bifurcation diagrams δ_{Cas} vs. φ for different δ_v for the Au-Au system. All points of the solid and dashed lines represent the stable and unstable saddle points respectively. (b) Variation of δ_{v} for different value of δ_{Cas} for the Au-Au system. (c) Phase portraits for $\delta_{\mathrm{v}} = 0$, $\delta_{\mathrm{Cas}} = 0.01$ and initial conditions inside and outside the homoclinic orbit. The stable and unstable orbits are indicated.

5.4.2 Optically different material systems: Au/SiC-SiC

Having illustrated the dynamical analysis for the Au-Au, we will proceed further with the comparison between different materials. For this purpose we considered for the minimum Casimir torque τ_{Cas}^{m} in Eqs. 5.6 and 5.7 its lowest value that occurs for the SiC-SiC system. Figures 5.4a and 5.4b show the bifurcation parameter δ_{Cas} is strongly sensitive to changes of the material optical properties with or without applied voltage.

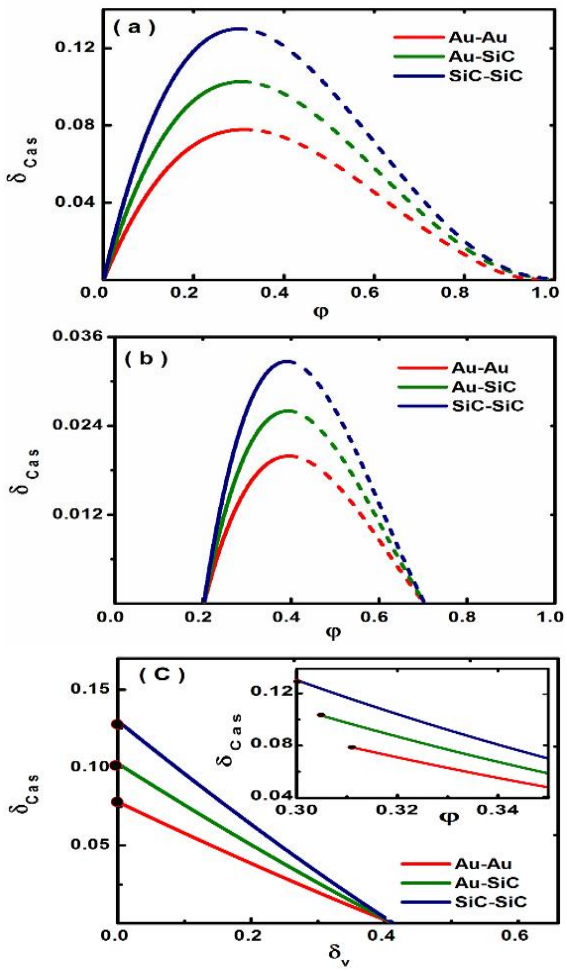

Figure 5.4: Bifurcation diagrams δ_{Cas} vs. φ for material combinations Au and SiC. The solid and dashed lines represent the center and unstable saddle points respectively. (a) $\delta_{\mathrm{v}} = 0$, and (b) $\delta_{\mathrm{v}} = 0.3$. (c) δ_{Cas} vs. δ_{v} for all combinations of Au and SiC. The inset shows δ_{Cas} vs. φ.

The region which corresponds to the stable actuation is strongly increased for the systems involving the less conductive material SiC. There are regions where the Au–Au system is unstable, while there are equilibrium points for the Au-SiC and SiC–SiC systems. Figure 4(c) shows that δ_{Cas} decreases with increasing δ_v, while it increases as overall with decreasing conductivity of the interacting materials. Similarly the inset in Figure 5.4(c) shows that the corresponding angle for the maximum of δ_{Cas} (circles) moves towards smaller values with decreasing conductivity. Therefore, we can infer that a torsional system, where the interacting surfaces under motion are coated with high conduction materials, will lose sooner its stability with decreasing restoring torque (since $\delta_{Cas} \sim 1/k$) in comparison to a system made from lower conductivity materials.

The phase portraits for different materials are presented in Figure 5.5(a) and 5.5(b). The closed orbits, which correspond to periodic motion around the stable center equilibrium point, are very sensitive to changes in the material conductivity with the Au-Au system having the largest orbit due to the stronger Casimir torque bringing the moving plate closest to the fixed plate. This is manifested in Figure 5.5(b), which shows the Au-Au system to be driven rapidly to stiction, while the other systems remain functional. If, however, we increase the dissipation or equivalently reduce the quality factor Q, then it is still feasible to reduce the possibility to drive the system into stiction. For finite Q factor, Eq. 5.3 obtains the form

$$I\frac{d^2\varphi}{dt^2} + I\frac{\omega}{Q}\frac{d\varphi}{dt} = -\varphi + \delta_v\frac{1}{\varphi^2}\left[\ln(1-\varphi) + \frac{\varphi}{1-\varphi}\right] + \delta_{Cas}\left[\frac{\tau_{cas}}{\tau_{Cas}^m}\right]. \quad (5.8)$$

The effect of finite Q due to intrinsic and extrinsic dissipation mechanisms [44] of the oscillating plate is shown in Figure 5.5(c). The values of the Q factor considered here are typical for a multitude of MEMS/NEMS operating in air or vacuum [8, 28, 40, 44]. Indeed, calculations indicate that the transition from stable, but dissipative motion, to unstable motion towards stiction takes place in Figure 5.5(c) for the critical quality factor $Q_C \approx 370$. The latter is typical for operation under ambient conditions [44]. Therefore, proper tuning of the system Q factor can also help to prevent the stiction of an otherwise unstable system. From Eq. 5.8 we can estimate the critical Q_C by setting in Eq. 5.6 $I\,(d^2\varphi/dt^2) \approx 0$ (around the critical point $\varphi = \varphi_C$ where the transition from stiction to dissipative stable motion occurs) and $d\varphi/dt = \omega$. Substitution in Eq. 5.7 yields for Q_C

$$\frac{1}{Q_c} \approx -\varphi_C + \delta_v\frac{1}{\varphi_C^2}\left[\ln(1-\varphi_C) + \frac{\varphi_C}{1-\varphi_C}\right] + \delta_{Cas}\left[\frac{\tau_{cas}(\varphi_C)}{\tau_{Cas}^m}\right]. \quad (5.9)$$

For the conditions in Figure 5.5(c) ($\delta_v = 0$, $\delta_{Cas} = 0.66$, and $\varphi_C = 0.47$), Eq. 5.8 yields for Q_c the numerical value $Q_c \approx 370$.

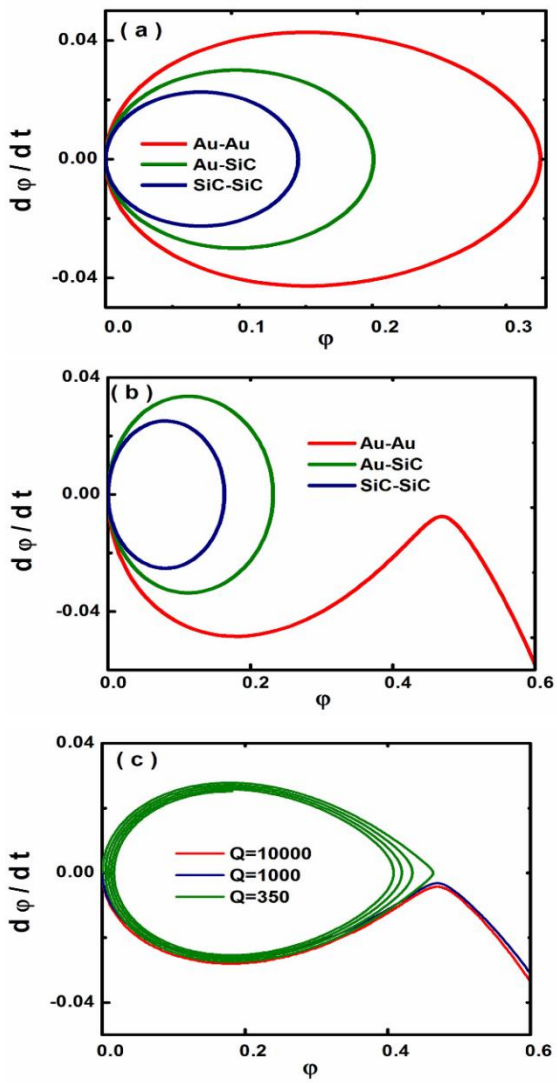

Figure 5.5: (a) Phase portraits for torsional system which made from Au, SiC by using the Drude model with $\delta_{Cas} = 0.06$ and $\delta_v = 0$. (b) $\delta_{Cas} = 0.066$, $\delta_v = 0$. Closed orbits indicate stable motion, while an open orbit is the sign of unstable motion leading to stiction c. (c) Influence of the damping term on actuation dynamics of Au torsional MEMS with $\delta_{Cas} = 0.066$, $\delta_v = 0$ and different values of the quality factor Q.

5.5 Conclusion

In conclusion, we have investigated how the dependence of the mechanical Casimir torque on the optical properties of interacting materials could play a role on the actuation dynamics of single beam torsional MEMS. The bifurcation curves and the phase portraits of the actuation dynamics have been analyzed to compare the sensitivity of a single beam torsional device operating between materials with conductivities that differ by several orders of magnitude. It is shown that the range of stable operation of torsional MEMS against stiction instabilities can increase by decreasing the conductivity of interacting materials. Moreover, the introduction of controlled dissipation, corresponding to a finite quality factor Q, in an otherwise unstable torsional system, could alter an unstable motion towards stiction to dissipative stable motion. Therefore, the proper choice of the conductivity of interacting materials in torsional MEM systems, and the tuning of energy dissipation, can help to maximize their regime of stable operation.

References

[1] A. W. Rodriguez, F. Capasso and S. G. Johnson, Nat. Photonics **5** 211 (2011).
[2] F. Capasso, J. N. Munday, D. Iannuzzi, & H. B. Chan. IEEE J. Sel. Top. Quant. Electron. **13,** 400 (2007).
[3] P. Ball. Nature **447,** 772 (2007).
[4] M. Bordag, G. L. Klimchitskaya, U. Mohideen, V. M. Mostepanenko, Advances in the Casimir Effect, Oxford University Press, New York, (2009).
[5] P. W. Milonni. The Quantum Vacuum: An Introduction to Quantum Electrodynamics (Academic, 1993).
[6] H. B. G. Casimir, Proc. K. Ned. Akad. Wet. **51** 793 (1948).
[7] E. M. Lifshitz. Sov. Phys. JETP **2,** 73 (1956); I. E. Dzyaloshinskii, E. M. Lifshitz and L. P. Pitaevskii. Sov. Phys. Usp. **4,** 153 (1961).
[8] S. K. Lamoreaux, Phys. Rev. Lett. **78**, 5 (1997); Rep. Prog. Phys. **68**, 201 (2005); H. B. Chan, V. A. Aksyuk, R. N. Kleiman, D. J. Bishop, and F.Capasso,Phys. Rev. Lett. **87**, 211801 (2001); Science **291**, 1941 (2001); R. S. Decca, D. L´opez, E. Fischbach, G. L. Klimchitskaya, D. E. Krause, and V. M. Mostepanenko, Ann. Phys. (NY) **318**, 37 (2005); ,Phys. Rev. D **75**, 077101 (2007).
[9] D. Iannuzzi, M. Lisanti, and F. Capasso, Proc. Natl. Acad. Sci. USA **101**, 4019 (2004).
[10] F. Chen, G. L. Klimchitskaya, V. M. Mostepanenko, and U. Mohideen, Opt. Express **15**, 4823 (2007); G. Torricelli, I. Pirozhenko, S. Thornton, A. Lambrecht, and C. Binns, Europhys. Lett. **93**, 51001 (2011).
[11] S. de Man, K. Heeck, R. J.Wijngaarden, and D. Iannuzzi, Phys. Rev. Lett. **103**, 040402 (2009).
[12] G. Torricelli, P. J. van Zwol, O. Shpak, C. Binns, G. Palasantzas, B. J. Kooi, V. B. Svetovoy, and M. Wuttig, Phys. Rev. A **82**, 010101 (R) (2010).
[13] G. Torricelli, P. J. van Zwol, O. Shpak, G. Palasantzas, V. B. Svetovoy, C. Binns, B. J. Kooi, P. Jost, and M. Wuttig, Adv. Funct. Mater. **22**, 3729 (2012).
[14] C.-C. Chang, A. A. Banishev, G. L. Klimchitskaya, V. M. Mostepanenko, and U. Mohideen, Phys. Rev. Lett. **107**, 090403 (2011).
[15] V. B. Svetovoy, P. J. van Zwol, G. Palasantzas, and J. Th. M. DeHosson, Phys. Rev. B. **77**, 035439 (2008); G. Bimonte, Phys. Rev. A **83**, 042109 (2011).
[16] A. Canaguier-Durand, P. A. Maia Neto, A. Lambrecht, and S. Reynaud, Phys. Rev. A **82**, 012511 (2010).
[17] M. Sedighi, V. B. Svetovoy, W. H. Broer, and G. Palasantzas, Phys. Rev. B **89**, 195440 (2014).
[18] M. Sedighi, W. H. Broer, G. Palasantzas, and B. J. Kooi. Phys. Rev. B **88**, 165423 (2013).
[19] H.-C. Chiu, G. L. Klimchitskaya, V. N. Marachevsky, V. M. Mostepanenko, and U. Mohideen. Phys. Rev. B **81**, 115417(2010); F. Chen**,** U. Mohideen, G. L. Klimchitskaya V. M. Mostepanenko, Phys. Rev. A **66**, 032113 (2002); T. Emig, A. Hanke, R. Golestanian, and M. Kardar. Phys. Rev. A **67**, 022114 (2003).

[20] F. Chen, U. Mohideen, G. L. Klimchitskaya and V. M. Mostepanenko. Phys. Rev. Lett.**88**, 101801(2002)
[21] R. B. Rodrigues, P. A. Maia Neto, A. Lambrecht and S. Reynaud, J. Phys. A. **41**. 164004 (2008).
[22] R. Guérout, A. Lambrecht, S. Reynaud C.Gent, Euro. Phys. Lett.**111**. 4 (2015).
[23] R. B. Rodrigues, P. A. Maia Neto, A. Lambrecht and S. Reynaud, Euro. Phys. Lett.**76**.822 (2006).
[24] J.N. Munday, D. Iannuzzi, Y. Barash, and F. Capasso, Phys. Rev. A **71**, 042102 (2005).
[25] J.N. Munday, D. Iannuzzi, and F. Capasso, New J. Phys.**8**, 244 (2006).
[26] T.G. Philbin and U. Leonhardt, Phys. Rev. A **78**, 042107(2008).
[27] X. Chen and J.C.H. Spence, Phys. Stat. Sol. A **210**, 9 (2013).
[28] F. Intravaiv, S. Koev, I. W. Jung , A. A. Talin, P. S. Davids, R. S. Decca, V. A. Aksvuk, D. A. R. Dalvit & D. Lopez, Nature Communications **4**, 2515 (2013); R. S. Decca, D. Lopez, E. Fischbach, G. L. Klimchitskaya, D. E. Krause and V. M. Mostepanenko, Annals of Physics **318**, 37 (2005).
[29] Y. Nemirovsky and O. Degani, J. Microelectromech. Syst. **10**, 601 (2001).
[30] O. Degani and Y. Nemirovsky, J. Microelectromech. Syst. **11**, 20 (2002).
[31] J. G. Guo, Y. P. Zhao. International Journal of Solids and Structures **43**, 675 (2006); R. Sattler, F. Plotz, G. Fattinger, and G. Wachutka, Sensors and Actuators A **97-98**, 337 (2002).
[32] R. Satter, F. Plötz, G. Fattinger, and G.Wachutka, Sens. Actuators, A **97–98**, 337 (2002).
[33] O. Bochobza-Degani and Y. Nemirovsky, Sens. Actuators, A **97-98**, 569 (2002).
[34] W. Broer, G. Palasantzas, J. Knoester, V.B. Svetovoy, Phys. Rev. B **87**, 125413 (2013).
[35] G. Palasantzas and J. Th. M. De Hosson, Phys. Rev. B **72**, 115426 (2005).
[36] M. Sedighi, V. B. Svetovoy, and G. Palasantzas, Phys. Rev. B **93**, 085434 (2016)
[37] M Sedighi, W H Broer, S Van der Veeke, V B Svetovoy and G Palasantzas, J. Phys.: Condens. Matter **27**, 214014 (2015)
[38] W. Broer, H. Waalkens, V. B. Svetovoy, J. Knoester, and G. Palasantzas, Phys. Rev. Applied **4**, 054016 (2015)
[39] W.H. Lin and Y.P. Zhao, J. Phys. D: Appl. Phys. **40**, 1649 (2007).
[40] R. S. Decca, D. López, E. Fischbach, G. L. Klimchitskaya, D. E. Krause, and V. M. Mostepanenko, Phys. Rev. D **75,** 077101 (2007).
[41] O. Degani, E. Socher, A. Lipson, T. Lejtner, D. J. Setter, Sh. Kaldor, Y. Nemirovsky, J. Microelectromech. Syst. **7,** 373 (1998).
[42] W. H. Lin, Y. P. Zhao. Chaos, Solitons and Fractals **23** 1777 (2005).
[43] V. B. Svetovoy and G. Palasantzas, Advances in Colloid and Interface Science **216**, 1 (2015); G. Palasantzas, V. B. Svetovoy and P. J. van Zwol, Int. J. Mod. Phys. B **24** 6013 (2010).
[44] R. Garcıa and R. Perez, Surf. Sci. Rep. **47,** 197 (2002), M. Li, H. X. Tang and M. L. Roukes Nat. Nanotechnol **2**, 114 (2007).
[45] S. Cui and Y. C. Soh, J. Microelectromech. Syst. **19,** 1153 (2010).

[46] M. W. Hirsch, S. Smale, and R. L. Devaney, Differential Equations, Dynamical Systems, and an Introduction to Chaos (Elsevier Academic Press, San Diego, CA, 2004).

Chapter 6

Chaotic behavior in Casimir oscillators: A case study for phase-change materials

Abstract. *Casimir forces between material surfaces at close proximity of less than 200 nm can lead to increased chaotic behavior of actuating devices depending on the strength of the Casimir interaction. We investigate these phenomena for phase change materials in torsional oscillators, where the amorphous to crystalline phase transitions lead to transitions between high and low Casimir force and torque states respectively, without material compositions. For a conservative system bifurcation curve and Poincare maps analysis show the absence of chaotic behavior but with the crystalline phase (high force-torque state) favoring more unstable behavior and stiction. However, for a non-conservative system chaotic behavior can take place introducing significant risk for stiction, which is again more pronounced for the crystalline phase. The latter illustrates the more general scenario that stronger Casimir forces and torques increase the possibility for chaotic behavior. The latter is making impossible to predict whether stiction or stable actuation will occur on a long term basis, and it is setting limitations in the design of micro-nano devices operating at short range nanoscale separations.*

This chapter has been published in :

F Tajik, M Sedighi, M. Khorrami, A A. Masoudi, G Palasantzas, “Chaotic behavior in Casimir oscillators: A case study for phase-change materials”, *Phys. Rev. E* 96, 042215 (2017).

6.1 Introduction

Nowadays, advancements in fabrication techniques has led to scaling down of micromechanical systems into the submicron length scales, which open new areas of applications of the Casimir effect [1-7]. This is because micro-nano electromechanical systems (MEMS-NEMS) have surface areas large enough but gaps small enough for the Casimir force to play significant role. An example is a torsional actuator that is a kind of MEM with applications to torsional radio frequency (RF) switches, tunable torsional capacitors, torsional micro mirrors, and Casimir force measurements in the search of new forces beyond the standard model [1-4,8]. A simple torsional device (cantilever type) has two electrodes with one fixed and the other able to rotate around an axis [9]. The electrostatic and Casimir force can rotate the movable electrode towards the surface of the fixed electrode, and under certain conditions it can undergo jump-to-contact leading to permanent adhesion, a phenomenon known as stiction.
Although the Casimir force was predicted in 1948 [10], one must use the Lifshitz theory to compute the force between real dielectric materials [11]. This is accomplished by exploiting the fluctuation-dissipation theorem, which relates the dissipative properties of the plates (optical absorption by many microscopic dipoles) and the resulting electromagnetic field fluctuations that mediate the Casimir interaction between macroscopic bodies [11]. Since the optical properties of materials play crucial role on the Casimir force [12-14], it is anticipated to influence the actuation dynamics of MEMS. Indeed, it has been predicted that less conductive materials can enhance stable operation of MEMS in comparison to metal coated electrodes that yield higher Casimir forces [15]. In addition, there have been several investigations on Casimir torques [16-22] for possible applications on MEMS-NEMS. The genuine Casimir torque in periodic systems arise due to the broken rotational symmetry [16-18], while in optically anisotropic materials it originates from the misalignment between two optical axes [19-22]. Moreover, the actuation of MEMS can be influenced by mechanical Casimir torques originating from normal Casimir forces [23-27].
Furthermore, the magnitude of the Casimir force, and consequently the corresponding mechanical Casimir torque, can be modulated using, for example, the amorphous and crystalline phase transitions in phase change materials (PCMs) without composition changes [14]. Notably the similar possibilities were also explored using the metal-to-insulator phase transitions in hydrogen-switchable mirrors, and topological-insulator materials [28]. In any case the PCMs are renowned for their use in optical data storage (Blue-Rays, DVDs etc.) where they

switch reversibly between the amorphous and crystalline phases [29]. Here we have chosen the AIST ($Ag_5In_5Sb_{60}Te_{30}$) PCM to perform our study, since we have measured the optical properties and the corresponding Casimir forces [14]. The amorphous phase of AIST is a semiconductor, while the crystalline phase shows closely metallic behavior [29], which is highly distinct from the amorphous state at low frequencies due to the high absorption of free carriers in the far-infrared (FAR-IR) spectrum [14]. Crystallization of the amorphous AIST has led up to ~25 % Casimir force contrast [14].
Therefore, PCMs offer a unique system to study how changes of the magnitude of the Casimir force and torque within the same system could affect the actuation dynamics of MEMS-NEMS. So far there is limited knowledge on how the Casimir forces-torques between actuating components at close proximity (typically less than 200 nm) can lead to chaotic behavior with changing strength of the force in relation also to the conduction properties of interacting materials. Surface roughness has been shown to strongly increase the Casimir force at separations less than 100 nm, and lead to chaotic behavior [30, 31]. On the other hand, for flat surfaces, which are desirable in device application, this is also a possible scenario that has to be carefully investigated since Casimir forces are omnipresent. Hence, we will investigate here the occurrence of chaotic behavior in torsional oscillators when the amorphous to crystalline phase transitions lead to transitions between low and high Casimir force states respectively, though the conclusions have qualitatively general application for any material that is used in actuation of micro-nano devices.

6.2 Theory of actuation system

The equation of motion for the torsional system (see Figure 6.1), where the fixed and rotatable plates are assumed to be coated with gold (Au) and AIST PCM respectively [14], is given by

$$I_0 \frac{d^2\theta}{dt^2} + \varepsilon\, I_0 \frac{\omega_0}{Q} \frac{d\theta}{dt} = \tau_{res} + \tau_{elec} + \tau_{Cas} + \varepsilon\, \tau_0 \cos(\omega t) \tag{6.1}$$

where I_0 is the rotation inertia moment of the rotating plate. The conservative case corresponds to ε=0, while the non-conservative forced oscillation with dissipation to ε=1. The mechanical Casimir torque τ_{Cas} is given by [25]

$$\tau_{Cas} = \int_0^{L_x} r F_{Cas}(d') L_y \, dr \tag{6.2}$$

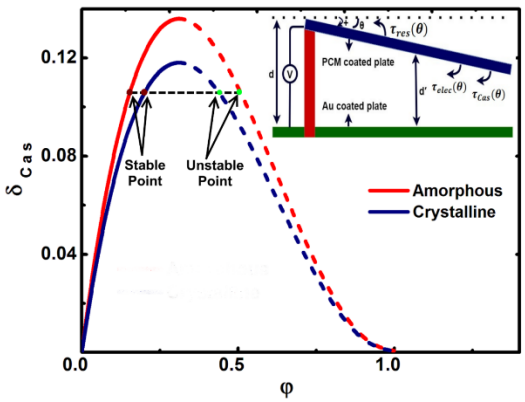

Figure 6.1: Bifurcation diagrams δ_{Cas} vs. φ for $\delta_v = 0$. The solid and dashed lines represent the stable and unstable points respectively. The inset shows the schematic of the torsional system.

where $F_{\mathrm{Cas}}(d)$ is the Casimir force (see chapter 2, Sect. 2.7 and 2.8 for Casimir force calculations via Lifshitz theory and dielectric function extrapolations in Figures 6.2 and 6.3), L_x and L_y are the length and width of each of the plates respectively (with $L_x = L_y = 10\mu m$), and $d' = d - r\sin\theta$ with d the distance for parallel plates.

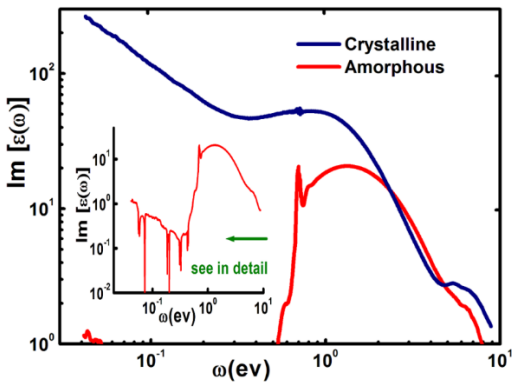

Figure 6.2: Imaginary part $\varepsilon''(\omega)$ of the frequency-dependent dielectric function for both phases of AIST [14].

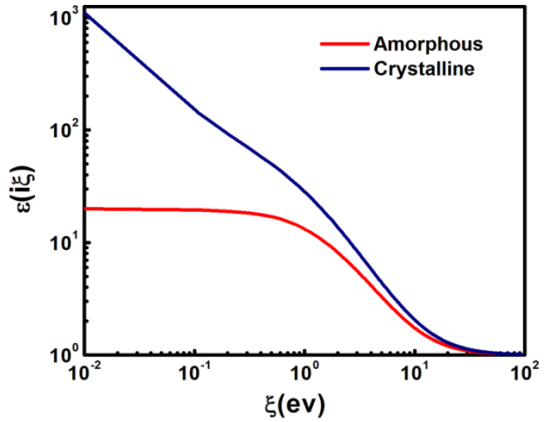

Figure 6.3: Dielectric functions at imaginary frequencies $\varepsilon(i\xi)$ for both phases of the AIST PCM.

The torsion angle θ, which is considered positive as the plates move closer to each other, and its sign are also indicated in the inset of Fig. 6.1 that shows the actuating system. We assume also d=200 nm so that the maximum torsion angle θ_0 to remain small ($\theta_0 = d/L_x = 0.02 \ll 1$) in order to ignore also any buckling of the moving beam (assuming typical operation at 300 K). Moreover, the electrostatic torque τ_{elec} due to an applied potential V_a is given by [14, 25]

$$\tau_{elec} = \frac{1}{2}\varepsilon_0 L_y (V_a - V_c)^2 \frac{1}{\sin^2(\theta)} \left[\ln\left(\frac{d - L_x \sin(\theta)}{d}\right) + \frac{L_x \sin(\theta)}{d - L_x \sin(\theta)}\right] \quad (6.3)$$

with ε_0 the permittivity of vacuum, and V_c is the contact potential difference between Au and AIST (V_c~0.4 V for both phases of AIST) [14]. In the following we will consider only the potential difference $V = V_a - V_c$ for the Casimir torque calculations, and we will ignore small variations of V_c between the amorphous and crystalline phases (~25 mV [14]). Both the Casimir and electrostatic torques are counterbalanced by the restoring torque $\tau_{res} = -k\theta$ with k the torsional spring constant around the support point of the beam [32]. Finally, the term $I_0(\omega/Q)(d\theta/dt)$ in Eq. 6.1 is due to the energy dissipation of the oscillating beam with Q the quality factor. The frequency ω is assumed to be typical like in AFM cantilevers and MEMS [1-4, 33].

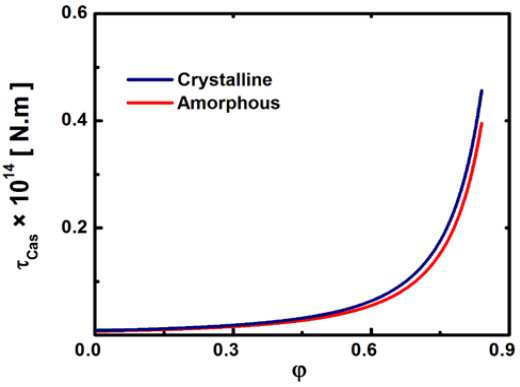

Figure 6.4: Casimir torques calculated for Au-PCM materials using as input the PCM optical data from Figure 6.3.

In order to investigate the actuation dynamics by taking into account the effect of PCM phase transitions, we introduce the bifurcation parameter $\delta_{Cas} = \tau^{m}_{Cas} / k\theta_0$ that represents the ratio of the minimal Casimir torque $\tau^{m}_{Cas} = \tau_{Cas}(\theta = 0)$ for the amorphous phase of AIST, and the maximum restoring torque $k\theta_0$ [34]. Eq. 6.1 can be rewritten in a normalized form in terms of δ_{Cas}, $\varphi = \theta/\theta_0$, and the bifurcation parameter of the electrostatic force $\delta_v = (\varepsilon_0 V^2 L_y L_x^3)/(2kd^3)$ [21],

$$\frac{d^2\varphi}{dT^2} + \varepsilon \frac{1}{Q}\frac{d\varphi}{dT} = -\varphi + \delta_v \frac{1}{\varphi^2}\left[\ln(1-\varphi) + \frac{\varphi}{1-\varphi}\right] + \delta_{Cas}\left[\frac{\tau_{cas}}{\tau^{m}_{Cas}}\right] + \varepsilon \frac{\tau_0}{\tau^{Max}_{res}}\cos\left(\frac{\omega}{\omega_0}T\right) \quad (6.4)$$

with $I = I_0/k$ and $T = \omega_0 t$.

6.3 Conservative system (ε=0)

The equilibrium points for conservative motion are obtained from the condition $\tau_{total} = \tau_{res} + \tau_{elec} + \tau_{Cas} = 0$, which yields

$$-\varphi + \delta_v \frac{1}{\varphi^2}\left[\ln(1-\varphi) + \frac{\varphi}{1-\varphi}\right] + \delta_{Cas}\left[\frac{\tau_{cas}}{\tau^{m}_{Cas}}\right] = 0. \quad (6.5)$$

Figure 6.1 shows plots of δ_{Cas} vs. φ for both the amorphous and crystalline phases for δ_v=0 or equivalently V=0 (for $\delta_v > 0$ see Figures 6.5 and 6.6). Similarly to the Casimir bifurcation diagrams in Fig 6.1, the bifurcation parameter δ_v also shows sensitive dependence on the amorphous to crystalline phase transition. In both cases the bifurcation curves of the amorphous and crystalline

phases are distinct around the maximum, where one approaches critical unstable behavior.

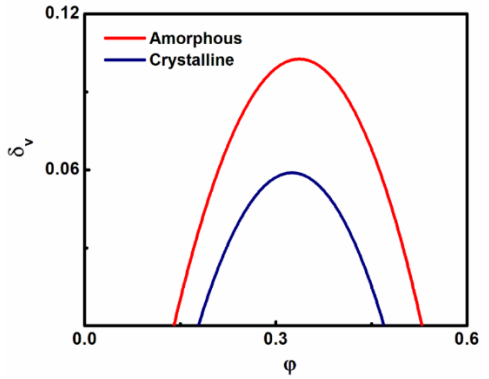

Figure 6.5: Bifurcation diagrams for both PCM states of the electrostatic parameter δ_v vs. φ with $\delta_{Cas} = 0.1$.

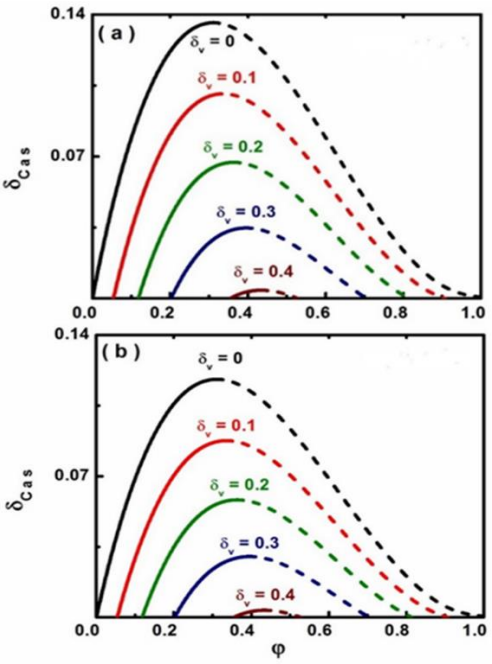

Figure 6.6: Bifurcation diagrams δ_{Cas} vs. φ for different δ_v. All points of the solid and dashed lines represent the stable and unstable points respectively in (a) amorphous and (b) crystalline phase. δ_{Cas}^{MAX} decreases in magnitude if one compares the amorphous and crystalline phases.

In Fig. 6.1 the solid lines show the stable regions where the restoring torque τ_{res} is strong enough to ensure stable periodic motion. The dash lines indicate unstable regions where the moving beam undergoes stiction. When $\delta_{Cas} < \delta_{Cas}^{MAX}$ two equilibrium points exist. The equilibrium point closer to $\varphi = 0$ (solid line) is a stable center point, and the other one closer to $\varphi = 1$ (dashed line) is the unstable saddle point. The latter obeys the additional condition $d\tau_{total}/d\varphi = 0$, which yields

$$-1 + \delta_v \left[\frac{2\varphi - 3}{\varphi^2(1-\varphi)^2} + \frac{2\ln(1-\varphi)}{\varphi^3}\right] + \delta_{Cas}\frac{1}{\tau_{Cas}^m}\left(\frac{d\tau_{Cas}}{d\varphi}\right) = 0. \quad (6.6)$$

By increasing δ_{Cas} or weakening the restoring torque ($\delta_{Cas} \sim 1/k$), the distance between the equilibrium points decreases until δ_{Cas} reaches the maximum saddle point δ_{Cas}^{MAX}. In fact, when $\delta_{Cas} \sim \delta_{Cas,C}^{MAX}$ for the crystalline phase, it is still $\delta_{Cas} < \delta_{Cas,A}^{MAX}$ for the amorphous phase ensuring the presence of two equilibrium points and increased possibility for stable motion. The situation is qualitatively similar in presence of an electrostatic force (see Figures 6.6 and 6.7).

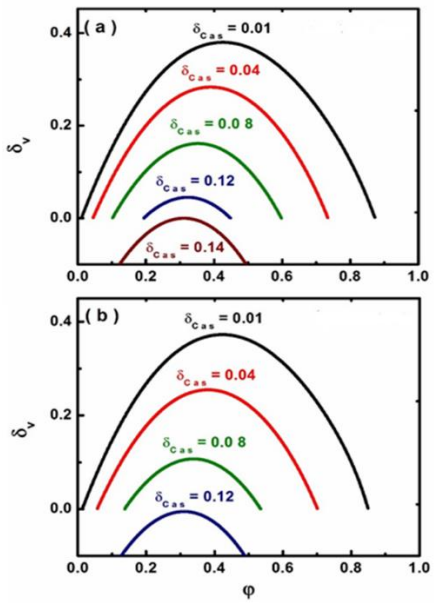

Figure 6.7: Variation of δ_v for different values of δ_{Cas} in (a) amorphous, and (b) crystalline phases. It can be clearly seen that for $\delta_{Cas} \leq 0.12$ we have $\delta_v \geq 0$. The latter means that for $\delta_{Cas} > 0.12$ there is no stability even without any voltage. For the amorphous phase the value of the critical δ_{Cas} is larger, and a weaker restoring torque can lead to stable actuation.

According to the diagram of the bifurcation parameter δ_v, the maximum δ_v^{MAX} decreases similar to δ_{Cas}^{MAX}. The range of bifurcation parameters to produce periodic motion ($0 < \delta_{Cas} < \delta_{Cas}^{MAX}$ and $\delta_v \geq 0$) is decreased during the amorphous to crystalline phase transition. Note that for $\delta_{Cas} > \delta_{Cas}^{MAX}$ there is no stability in the torsional device even in the absence of electrostatic torques ($\delta_v = 0$). In any case, when the applied voltage increases, δ_{Cas}^{MAX} decreases for both PCM phases. As a result, since the electrostatic force is attractive, the device would require higher restoring torque to ensure stable operation.
Besides the bifurcation diagrams, the sensitive dependence of the actuation dynamics on the PCM phase transition is reflected by the Poincare maps $d\varphi/dt$ vs. φ in Fig. 6.8 [35]. The homoclinic orbit separates unstable motion (leading to stiction within one period, Figure 6.9) from the periodic closed orbits around the stable center point.

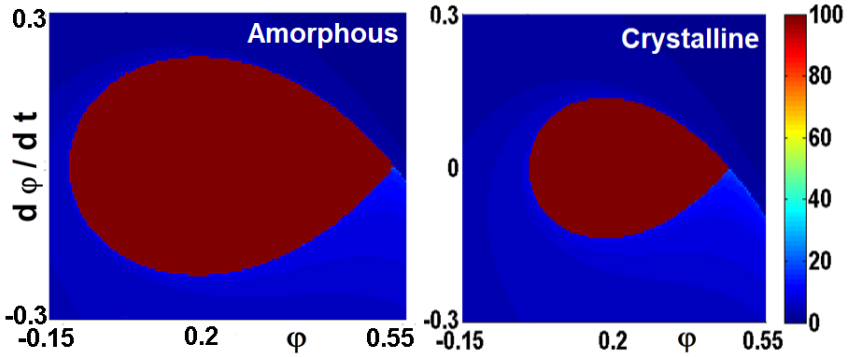

Figure 6.8: Poincare maps $d\varphi/dt$ vs. φ ($\delta_{Cas} = 0.1$, $\delta_v = 0$) of the conservative system (ε=0) for amorphous and crystalline PCM phases. For the calculations we used 150×150 initial conditions (φ, $d\varphi/dt$). The red (light gray) region (under the homoclinic orbit) shows that initial condition for which the torsional device shows stable motion after 100 oscillations with the natural frequency ω_0. The homoclinic orbit separates sharply stable and unstable solutions prohibiting chaotic behavior.

Since the distance between these two critical points is larger in the amorphous phase (see the phase portraits in Figure 6.10), a torsional MEMS can perform stable operation over a larger range of torsion angles. The orbit size in the crystalline phase is larger (Figure 6.9a) because the moving plate approaches closer the fixed plate. With increasing δ_{Cas}, the orbit breaks faster open for the crystalline phase leading to stiction (Figure 6.9), while for the amorphous phase there is still periodic motion.

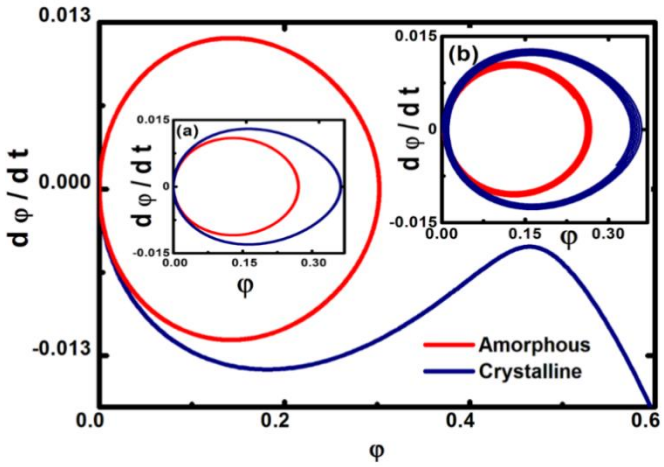

Figure 6.9: Phase portraits $d\varphi/dt$ vs. φ for $\delta_{Cas} = 0.1$, $\delta_v = 0$ and Q=∞. (a) Similar plot for smaller $\delta_{Cas} = 0.09$ where only stable motion takes place for both PCM phases. (b) Phase portraits for $\delta_{Cas} = 0.1$, $\delta_v = 0$, and finite damping contributing with Q=500.

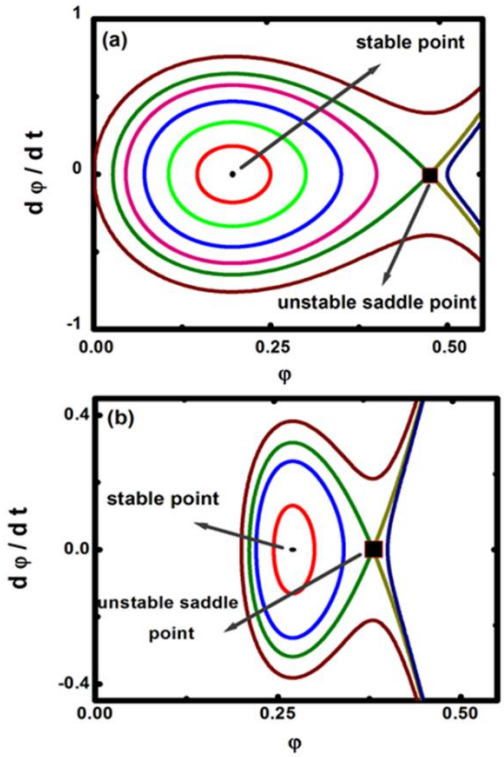

Figure 6.10: Phase portraits $d\varphi/dt$ vs. φ for $\delta_v = 0.05$ and $\delta_{Cas} = 0.1$, and initial conditions inside and outside of the homoclinic orbit. (a) Amorphous PCM, and (b) Crystalline PCM.

Therefore, the amorphous phase can ensure better device stability without any significant differences in electrostatic contributions (due to some difference in V_c [11]) from the crystalline phase.
Moreover, if one introduces some dissipation into the autonomous oscillating system via a finite quality factor Q, then dissipative motion can prevent stiction also for the crystalline phase despite the stronger Casimir torque (see Figure 6.9b and Figure 6.11). In any case, because the homoclinic orbit separates qualitatively different (stable-unstable) solutions, as the Poincare maps show in Fig. 6.8, it precludes the possibility of chaotic motion or equivalently sensitive dependence on the initial conditions [30, 35]. A chaotic oscillator can have qualitatively different solutions for an arbitrarily small difference in the initial conditions. As a result the conservative oscillating system provides an essential reference for the study of forced oscillations induced by an external applied forces and torque treated as a perturbative correction on the conservative system.

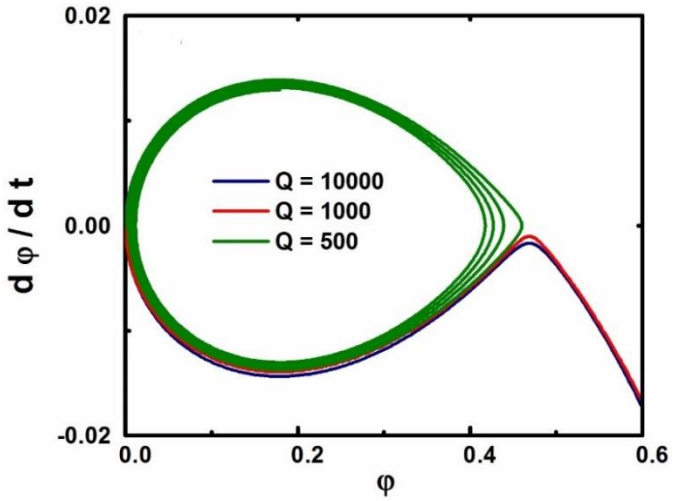

Figure 6.11: Influence of the damping term on actuation dynamics of torsional MEMS for the crystalline phase with $\delta_{Cas} = 0.1$, $\delta_v = 0$, and different values of the quality factor Q. A decreasing quality factor Q can change stiction to dissipative stable motion for torsional device.

6.4 Non-conservative system (ε=1)

Here we performed calculations to investigate the existence of chaotic behavior of the torsional system undergoing forced oscillation via an applied external torque $\tau_o \cos(\omega t)$ [30]. Chaotic behavior occurs if the separatrix (homoclinic orbit) of the conservative system splits, which it can be answered by the so-called Melnikov function and Poincare map analysis [30, 35]. If we define the homoclinic solution of the conservative system as $\varphi_{hom}^{C}(T)$, then the Melnikov function for the torsional system ($\varepsilon = 1$) is given by [30, 35]

$$M(T_0) = \frac{1}{Q}\int_{-\infty}^{+\infty}\left(\frac{d\varphi_{hom}^{C}(T)}{dT}\right)^2 dT + \frac{\tau_0}{\tau_{res}^{MAX}}\int_{-\infty}^{+\infty}\frac{d\varphi_{hom}^{C}(T)}{dT}\cos\left[\frac{\omega}{\omega_0}(T+T_0)\right]dT \quad (6.7)$$

The separatrix splits if the Melnikov function has simple zeros so that $M(T_0) = 0$ and $M'(T_0) \neq 0$. If $M(T_0)$ has no zeros, the motion will not be chaotic. The conditions of nonsimple zeros, $M(T_0) = 0$ and $M'(T_0) = 0$ gives the threshold condition for chaotic motion [30, 35]. If we define

$$\mu_{hom}^{c} = \int_{-\infty}^{+\infty}\left(\frac{d\varphi_{hom}^{C}(T)}{dT}\right)^2 dT \text{ and } \beta(\omega) = \left|H\left[Re\left(F\left\{\frac{d\varphi_{hom}^{C}(T)}{dT}\right\}\right)\right]\right|, \quad (6.8)$$

then the threshold condition for chaotic motion $\alpha = \beta(\omega)/\mu_{hom}^{c}$ with $\alpha = (1/Q)\left(\tau_0/\tau_{res}^{MAX}\right)^{-1} = \gamma\omega_{0\,\theta_0}/\tau_0$ obtains the form

$$\alpha = \frac{\gamma\omega_{0\,\theta_0}}{\tau_0} = \left|H\left[Re\left(F\left\{\frac{d\varphi_{hom}^{C}(T)}{dT}\right\}\right)\right]\right| \Big/ \int_{-\infty}^{+\infty}\left(\frac{d\varphi_{hom}^{C}(T)}{dT}\right)^2 dT \quad (6.9)$$

with $\gamma = I\omega_o/Q$, and H[...] denoting the Hilbert transform [30, 35].

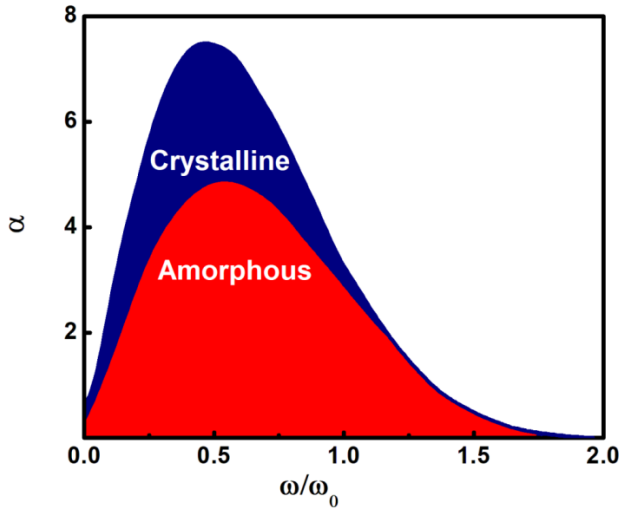

Figure 6.12: Threshold curve $\alpha\ (=\gamma\omega_{0\,\theta_0}/\tau_0)$ vs. driving frequency ω/ω_o (with ω_o the natural frequency of the system) for the amorphous and crystalline states. The area bellow the curve corresponds to chaotic motion.

Figure 6.12 shows the threshold curves $\alpha = \gamma\omega_{0\,\theta_0}/\tau_0$ vs. driving frequency ratio ω/ω_o. For large values of α (above the curve) the dissipation dominates the driving torque ($\alpha\sim\gamma/\tau_0$) leading to regular motion, which asymptotically approaches the stable periodic orbit of the conservative system. However, for parameter values below the curve, the splitting of the separatrix leads to chaotic motion. Clearly for the crystalline state, which gives to stronger Casimir torques, chaotic motion is more likely to occur.

Since we study the occurrence of chaotic motion in terms of the sensitive dependence of the motion on its initial conditions, we present in Fig.6.13 Poincare maps for different values of the threshold parameter α. When chaotic motion occurs (with decreasing value of α) there is a region of initial conditions where the distinction between qualitatively different solutions is unclear. If we compare with Fig. 6.8, where chaotic motion does not occur, the latter implies that for chaotic motion there is no a simple smooth boundary between the red (lighter gray) and the blue (Dark gray) regions. As a result, if the motion is chaotic then stiction can take place after several periods affecting the long-term stability of the device. Therefore, chaotic behavior introduces significant risk for stiction and this more prominent to occur for the more conductive crystalline PCM. In more general, as the Casimir force-torque increases the possibility for chaotic behavior increases and practically it could be impossible to predict whether stiction or stable actuation will occur on a long term basis.

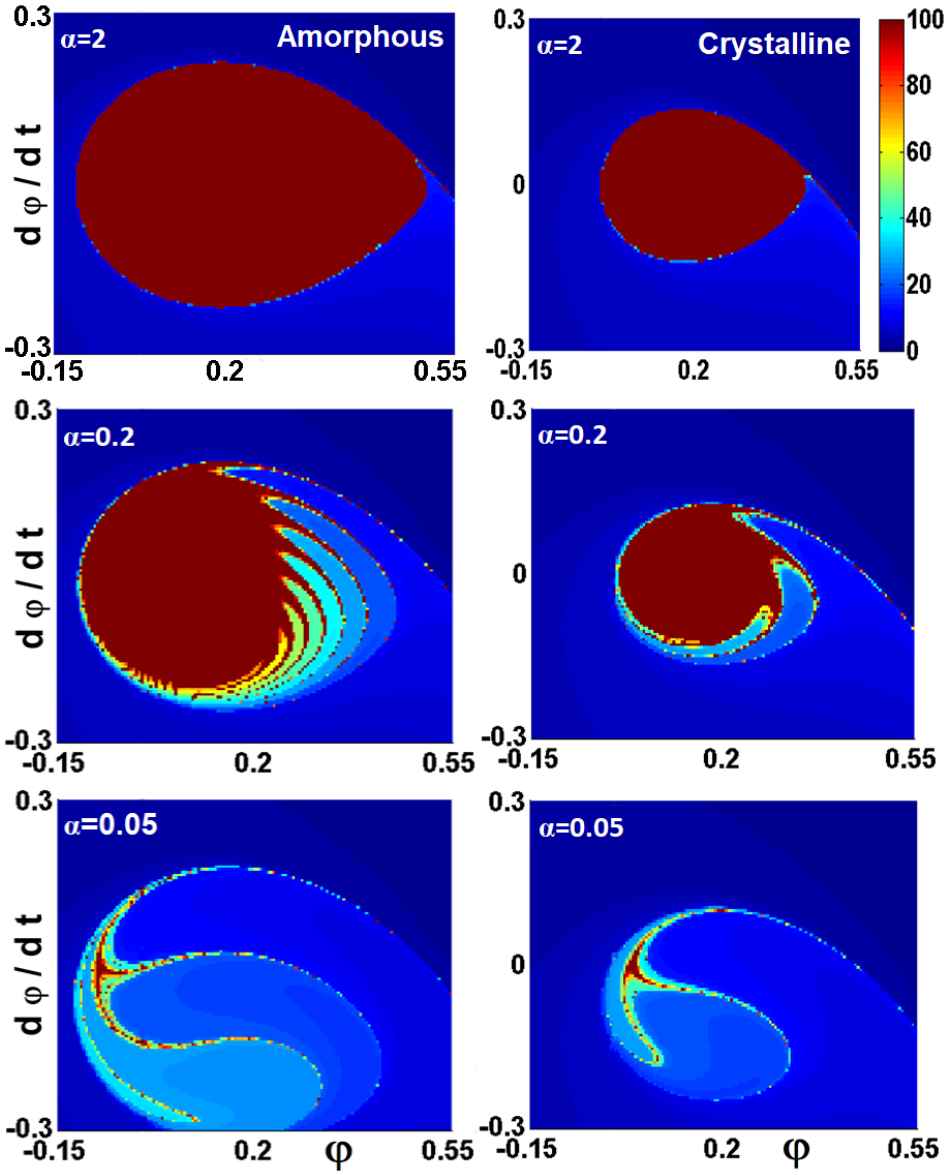

Figure 6.13: Poincare maps $d\varphi/dt$ vs. φ ($\delta_{Cas} = 0.1$, $\delta_v = 0$) of the non-conservative system (ε=1) for amorphous (left column) and crystalline (right column) PCM phases. For the calculations we used 150×150 initial conditions (φ, $d\varphi/dt$). The red region shows that initial condition for which the torsional device shows stable motion after 100 oscillations with oscillating frequency $\omega/\omega_0 = 0.8$. With decreasing α the chaotic behavior increases, and the area of stable motion shrinks more for the crystalline (high force-torque) phase.

6.5 Conclusions

In conclusion, Casimir forces and torques between actuating components at close proximity, typically less than 200 nm, can lead to increased chaotic behavior with increasing strength of the non-linear in nature Casimir interaction. We have illustrated these phenomena in torsional oscillators undergoing both conservative and non-conservative motion, where the amorphous to crystalline phase transitions in phase change materials lead to transitions between high and low Casimir force-torque states respectively. The occurrence of chaotic behavior introduces significant risk for stiction, and this more prominent for the more conductive crystalline phase that generates stronger Casimir forces and torques. In addition, this is also the case for conservative motion, where chaotic behavior is absent, that the crystalline phase is again more luckily to lead to stiction.

For the particular case of PCMs, our study shows that these materials can offer a versatile way to control motion by using both phases of the PCMs and controlled energy dissipation during device actuation. Furthermore, our analysis has general character in the sense that as the Casimir force-torque increases the possibility for chaotic behavior increases, and practically it could impossible to predict whether stiction or stable actuation will occur on a long term basis. The latter has serious implications because Casimir forces are omnipresent, and one must be very careful in choosing the proper conductivity materials in the design of micro-nano devices actuating at nanoscale separations.

References

[1] A. W. Rodriguez, F. Capasso and S. G. Johnson, Nat. Photonics **5** 211 (2011).
[2] F. Capasso, J. N. Munday, D. Iannuzzi, & H. B. Chan. IEEE J. Sel. Top. Quant. Electron. **13,** 400 (2007).
[3] M. Bordag, G. L. Klimchitskaya, U. Mohideen, V. M. Mostepanenko, Advances in the Casimir Effect, Oxford University Press, New York, (2009).
[4] R. S. Decca, D. López, E. Fischbach, G. L. Klimchitskaya, D. E. Krause, and V. M. Mostepanenko, Ann. Phys. (NY) **318**, 37 (2005); Phys. Rev. D **75**, 077101 (2007)
[5] A. Ashourvan, M.F. Miri, R. Golestanian Phys. Rev. Lett. **98,** 140801 (2014).
[6] M. F. Miri, R. Golestanian, Appl. Phys. Lett. **92**, 113103 (2011).
[7] A. Ashourvan, M.F. Miri, R. Golestanian, Phys. Rev. E. **75**, 040103 (2007).
[8] H.G. Craighead, Science **290**, 1532 (2000)
[9] O. Bochobza-Degani and Y. Nemirovsky, Sens. Actuators, **A97-98**, 569 (2002).
[10] H. B. G. Casimir, Proc. K. Ned. Akad. Wet. **51** 793 (1948).
[11] E. M. Lifshitz. Sov. Phys. JETP **2,** 73 (1956); I. E. Dzyaloshinskii, E. M. Lifshitz and L. P. Pitaevskii, Sov. Phys. Usp. **4,** 153 (1961).
[12] G. Palasantzas, V. B. Svetovoy and P. J. van Zwol, Int. J. Mod. Phys. B **24** 6013 (2010).
[13] F. Chen, G. L. Klimchitskaya, V. M. Mostepanenko, and U. Mohideen, Opt. Express **15**, 4823 (2007); C.-C. Chang, A. A. Banishev, G. L. Klimchitskaya, V. M. Mostepanenko, and U. Mohideen, Phys. Rev. Lett. **107**, 090403 (2011).
[14] G. Torricelli, P. J. van Zwol, O. Shpak, G. Palasantzas, V. B. Svetovoy, C. Binns, B. J. Kooi, P. Jost, and M. Wuttig, Adv. Funct. Mater. **22**, 3729 (2012).
[15] M. Sedighi, V. B. Svetovoy, W. H. Broer, and G. Palasantzas, Phys. Rev. B **89**, 195440 (2014).
[16] R. B. Rodrigues, P. A. Maia Neto, A. Lambrecht and S. Reynaud, J. Phys. A. **41**, 164004 (2008).
[17] R. Guérout, A. Lambrecht, S. Reynaud C.Gent, Euro. Phys. Lett.**111**, 4 (2015).
[18] R. B. Rodrigues, P. A. Maia Neto, A. Lambrecht and S. Reynaud, Euro. Phys. Lett.**76**, 822 (2006).
[19] J.N. Munday, D. Iannuzzi, Y. Barash, and F. Capasso, Phys. Rev. A **71**, 042102 (2005).
[20] J.N. Munday, D. Iannuzzi, and F. Capasso, New J. Phys.**8**, 244 (2006).
[21] T.G. Philbin and U. Leonhardt, Phys. Rev. A **78**, 042107(2008).
[22] X. Chen and J.C.H. Spence, Phys. Stat. Sol. A **210**, 9 (2013).
[23] Y. Nemirovsky and O. Degani, J. Microelectromech. Syst. **10**, 601 (2001).
[24] O. Degani and Y. Nemirovsky, J. Microelectromech. Syst. **11**, 20 (2002).
[25] J. G. Guo, Y. P. Zhao. International Journal of Solids and Structures **43**, 675 (2006); W.H. Lin and Y.P. Zhao, J. Phys. D: Appl. Phys. **40**, 1649 (2007).
[26] R. Satter, F. Plötz, G. Fattinger, and G.Wachutka, Sens. Actuators, **A97–98**, 337 (2002).
[27] W. H. Lin, Y. P. Zhao. Chaos, Solitons and Fractals **23** 1777 (2005).

[28] D. Iannuzzi, M. Lisanti, and F. Capasso, Proc. Nat. Acad. Sci. USA **101**, 4019(2004); A. G. Grushin and A. Cortijo, Phys. Rev. Lett. **106**, 020403 (2011)
[29] M. Wutting and N. Yamada Nature Material **6,** 824 (2007).
[30] W. Broer, H. Waalkens, V. B. Svetovoy, J. Knoester, and G. Palasantzas, Phys. Rev. Appl. **4**, 054016 (2015)
[31] V. B. Svetovoy and G. Palasantzas, Adv. Colloid and Interface Science **216**, 1 (2015).
[32] O. Degani, E. Socher, A. Lipson, T. Lejtner, D. J. Setter, Sh. Kaldor, Y. Nemirovsky, J. Microelectromech. Syst. **7,** 373 (1998).
[33] R. Garcıa and R. Perez, Surf. Sci. Rep. **47,** 197 (2002), M. Li, H. X. Tang and M. L. Roukes Nat. Nanotechnol **2**, 114 (2007).
[34] S. Cui and Y. C. Soh, J. Microelectromech. Syst. **19,** 1153 (2010).
[35] M. W. Hirsch, S. Smale, and R. L. Devaney. Differential Equations, Dynamical Systems, and an Introduction to Chaos, Elsevier Academic Press, San Diego, CA, (2004).

Chapter 7

Dependence of chaotic actuation of dynamics Casimir oscillators on optical properties and electrostatic effects

Abstract. *Casimir forces between material surfaces at close proximity of less With Casimir and electrostatic forces playing a crucial role for the performance and stability of microelectromechanical systems (MEMS), the presence of chaotic behavior, which is often unavoidable, leads to device malfunction due to stiction. Therefore, we investigate here how the optical properties of different materials influence the chaotic behavior of electrostatic torsional MEMS due to changes in magnitude of the Casimir forces and torques. We consider the materials Au, which is a good conductor, AIST, which is a phase change material being close to metal in the crystalline state, and finally doped SiC as a very poor conductor. For the conservative systems, there is no chaotic behavior and the analysis of phase portraits and bifurcation diagrams reveal the strong sensitivity of stable actuation dynamics on the material optical properties, while applied electrostatic potentials lead faster to instability and stiction for higher conductivity materials. For the driven systems, the Melnikov method is used to study the chaotic behavior. The results from this method are supported by the study of the contours of the transient time to stiction in the phase plane, which reveal a substantially increased chaotic behavior for higher conductivity materials, associated with stronger Casimir torques and applied electrostatic potentials.*

This chapter has been published in :

F Tajik, M Sedighi, A A. Masoudi, H. Waalkense, G Palasantzas, “Dependence of chaotic actuation dynamics of Casimir oscillators on optical properties and electrostatic effects”, Eur. Phys. J. B 91, 71(2018).

7.1 Introduction

Dispersion forces, also known as van der Waals and Casimir forces, are omnipresent in nature and become dominant when the bodies are separated by distances smaller than 100 nm [1]. With the advancement in fabrication and miniaturization of MEMS technology towards nanoelectromechanical systems (NEMS) [2-8], deep understanding of stiction phenomena and correct estimation of the magnitude of the Casimir force is crucial for the analysis and design of MEMS/NEMS involving complex materials. This is because these systems have sufficiently large surface areas and gaps small enough for Casimir forces and torques to play a significant role causing device malfunction due to permanent adhesion, known as stiction, of moving components. Therefore, strategies to reduce stiction are widely studied in an attempt to ensure stable device performance, and long-term predictability for complex MEMS/NEMS designs.

One of the most prominent methods of device actuation is electrostatic, where inevitably Casimir forces and torques could play a role [3, 9-11]. Although the electrostatic forces can be switched off when no potential is applied, the Casimir forces are omnipresent and can influence the actuation dynamics of devices. The Casimir force was predicted by H. Casimir in 1948 [12] where he proved that two perfectly conducting parallel plates, separated by a gap d, attract each other via the force $F_{Cas} = \pi^2 \hbar c/240 d^4$ due to perturbation of vacuum fluctuations of the electromagnetic (EM) field. Here ħ and c are the Planck constant and the speed of light, respectively. Soon after Lifshitz and co-workers [13] considered the general case of dielectric plates by exploiting the fluctuation-dissipation theorem, which relates the dissipative properties of the plates (optical absorption by many microscopic dipoles) and the resulting EM fluctuations. In terms of the Lifshitz theory [13] the van der Waals and Casimir forces are the short and long range limits, respectively, of the same force. In torsional systems these forces generate mechanical Casimir torques that have to be taken into account during the analysus of actuation dynamics.

Torsional MEMS, which find applications in torsional radio frequency (RF) switches, tunable torsional capacitors, torsional micro mirrors, and high precision Casimir force measurements [2-5], are viewed as a cantilever type, where of the two electrodes one is fixed and the other is able to rotate around an axis [14]. By simply applying a voltage, both the electrostatic and the mechanical Casimir torques, which originate from the normal Casimir force [15-19], can rotate the movable electrode towards the fixed one. However, under certain conditions it can undergo jump-to-contact, which could lead to stiction [20]. Furthermore, the design of MEMS can be quite challenging due to the occurrence of chaotic behavior, which causes abrupt changes in their dynamical

behavior, and as a result device malfunctions. Hence, more detailed knowledge about the phenomena of stiction and its relation to chaos is necessary to improve the performance and design of MEMS devices. So far, however, there is limited knowledge on how the Casimir forces-torques between actuating components at close proximity (typically less than 200 nm) can lead to chaotic behavior when changing the strength of the force via the optical properties of interacting materials, and possibly in presence of applied electrostatic potentials.

Therefore, we investigate here how the change in optical properties of materials, corresponding to several orders of magnitude change in material conductivity and subsequently of the Casimir torque [21-23], can influence the chaotic behavior of torsional MEMS taking into account electrostatic torques. The choice of the materials in the present study (see Figure 7.1) is motivated by requiring them to have the following properties: i) the application of electrostatic voltage is feasible [5, 23-28], ii) they are used in actuating devices, and iii) they show significantly diverse values of their conductivity ratio ω_p^2/ω_τ with ω_p the plasma frequency, and ω_τ the damping factor in terms of the Drude model that is used to fit the low frequency optical data in Casimir studies [5, 23-28].

7.2 Modeling of dynamical system

For our purpose, Au was used as a material due to its high conduction ratio $\omega_p{}^2/\ \omega_\tau|_{Au} \approx 1600$ eV and its frequent use in devices [5, 24]. As an intermediate conductivity system we used the crystalline (C) state of the phase change material (PCM) AIST ($Ag_5In_5Sb_{60}Te_{30}$). The latter is used in optical data storage (Blue-Rays, DVDs etc.) and analysis of the optical data for Casimir studies, with a measured force contrast ~25 % between the amorphous (A) and crystalline (C) states, yields the conductivity ratio $\omega_p{}^2/\ \omega_\tau|_{AIST(C)} = 10.1$ eV [23]. As a poor conductor we use nitrogen doped SiC, which is suitable for operation in harsh environments and an important element in Si-based technologies [26, 27]. Analysis of optical data gives for SiC the conductivity ratio $\omega_p{}^2/\ \omega_\tau|_{SiC} = 0.4$ eV [26]. The corresponding dielectric functions $\varepsilon(i\xi)$ at imaginary frequencies, which are necessary as input for the calculations of the Casimir force via Lifshitz theory (see chapter 2, Sect. 2.7 and 2.8 for Casimir force calculations via Lifshitz theory and dielectric function extrapolations), are shown in Fig. 7.1.

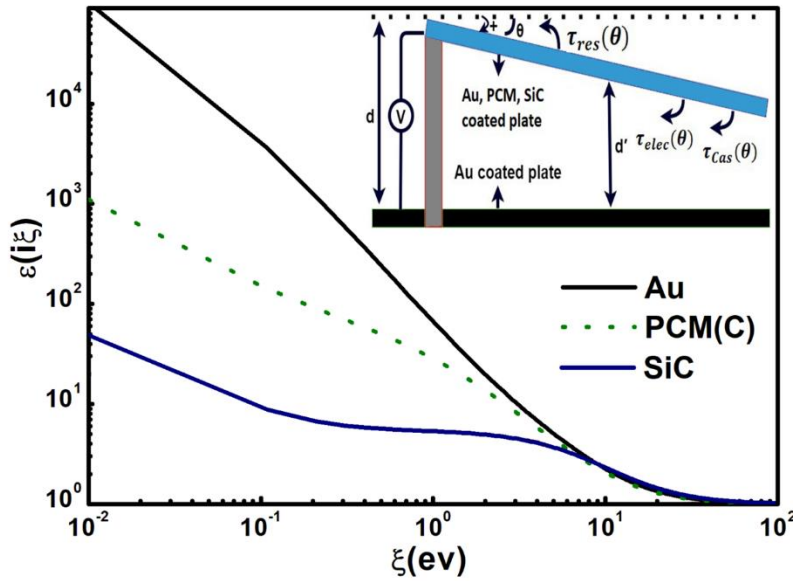

Figure 7.1: Dielectric functions at imaginary frequencies ε(iξ) for Au, SiC, and crystalline (C) AIST (PCM (C)) The inset shows the schematic of the torsional system.

Furthermore, we consider the electrostatic torsional actuator shown in the inset of Fig. 7.1, where only the upper plate is rotatable (and stiff enough to resist any buckling by the applied torques). The fixed plate is assumed to be coated by Au, while the rotatable one by the materials of interest Au, SiC, and AIST (C) (with coating thickness in all cases more than 100 nm to ensure optically bulk materials) [24, 26]. For simplicity, we consider flat plates because at short separations (<100 nm) nanoscale roughness can have significance influence [21, 29-31]. The initial distance when the plates are parallel is assumed to be d=200 nm, and the system temperature T=300 K. The equation of motion for the torsional system is given by

$$I_0 \frac{d^2\theta}{dt^2} + \varepsilon I_0 \frac{\omega_0}{Q} \frac{d\theta}{dt} = \tau_{res} + \tau_{elec} + \tau_{Cas} + \varepsilon\tau_0 \cos(\omega t), \qquad (7.1)$$

where I_0 is the rotation moment of inertia of the rotating plate. The term $I_0(\omega/Q)(d\theta/dt)$ in Eq. 7.1 is due to the intrinsic energy dissipation of the moving plate with Q the quality factor of the system. The frequency ω is assumed to be typical like in AFM cantilevers and MEMS [2-5]. The motion is conservative for ε=0, while for ε=1 we have forced non-conservative motion.
In Eq. 7.1 the torsional restoring torque τ_{res} is given by $\tau_{res} = k\theta$ with θ the torsional angle, which is considered positive as the plates move closer to each

other. k is the torsional spring constant around the support point allowing rotation of the rest of the beam [25, 32-34]. τ_{elec} is the electrostatic torque when a voltage V_a is applied between the two electrodes, and it is given by [17, 35]

$$\tau_{elec} = \frac{1}{2}\varepsilon_0 L_y (V_a - V_c)^2 \frac{1}{\sin^2(\theta)}\left[\ln\left(\frac{d - L_x\sin(\theta)}{d}\right) + \frac{L_x\sin(\theta)}{d - L_x\sin(\theta)}\right]. \quad (7.2)$$

V_c is the contact potential difference between the coating materials of the fixed and rotatable plate. In the following we will consider only the potential difference $V = V_a - V_c$ for the torque calculations. Finally the mechanical Casimir torque τ_{Cas}, which acts on the rotating plate, is given by [19]

$$\tau_{Cas} = \int_0^{L_x} r F_{Cas}(d') L_y dr, \quad (7.3)$$

where $F_{Cas}(d)$ is the Casimir force that is calculated using Lifshitz theory (see chapter 2, Sect. 2.7), and $d' = d - r\sin\theta$ with d the distance for parallel plates of width and length L_x and L_y. We choose $L_x = L_y = 10\mu m$ and d=200 nm so that the maximum torsional angle θ_0 remains small ($\theta_0 = d/L_x = 0.02 \ll 1$) in order to ignore also any buckling of the moving beam.

Furthermore, we introduce the Casimir bifurcation parameter $\delta_{Cas} = \tau^m_{Cas}/k\theta_0$, which represents the ratio of the minimum Casimir torque $\tau^m_{Cas} = \tau_{Cas}(\theta = 0)$ and the maximum restoring torque $k\theta_0$ [36, 37], and the bifurcation parameter for the electrostatic force $\delta_v = (\varepsilon_0 V^2 L_y L_x^3)/(2kd^3)$ [11, 16]. Using δ_{Cas} and δ_v Eq. (7.1) assumes the more convenient form

$$\frac{d^2\varphi}{dT^2} + \varepsilon\frac{1}{Q}\frac{d\varphi}{dT} = -\varphi + \delta_v\frac{1}{\varphi^2}\left[\ln(1-\varphi) + \frac{\varphi}{1-\varphi}\right] + \delta_{Cas}\left[\frac{\tau_{cas}}{\tau^m_{Cas}}\right] + \varepsilon\frac{\tau_0}{\tau^{Max}_{res}}\cos\left(\frac{\omega}{\omega_0}T\right) \quad (7.4)$$

with $\varphi = \theta/\theta_0$, $T = \omega_0 t$, and $I = I_0/k$.

7.3 Results and discussion

Conservative system (ε=0)

The equilibrium points for conservative motion are obtained by the condition $\tau_{total} = \tau_{res} + \tau_{elec} + \tau_{Cas} = 0$. The latter yields from Eq. 7.4

$$-\varphi + \delta_v\frac{1}{\varphi^2}\left[\ln(1-\varphi) + \frac{\varphi}{1-\varphi}\right] + \delta_{Cas}\left[\frac{\tau_{cas}}{\tau^m_{Cas}}\right] = 0. \quad (7.5)$$

Figure 7.2 shows plots of δ_{Cas}, δ_v vs. φ for all materials studied here. The solid lines in Fig. 7.2a show stable regions where the restoring torque τ_{res} is strong enough to produce a stable equilibrium point near which the motion is periodic since $\delta_{Cas} \sim 1/k$. The dash lines indicate unstable regions, where the equilibrium of the torsional system is unstable, and the moving beam undergoes stiction due to motion close to the fixed plate.

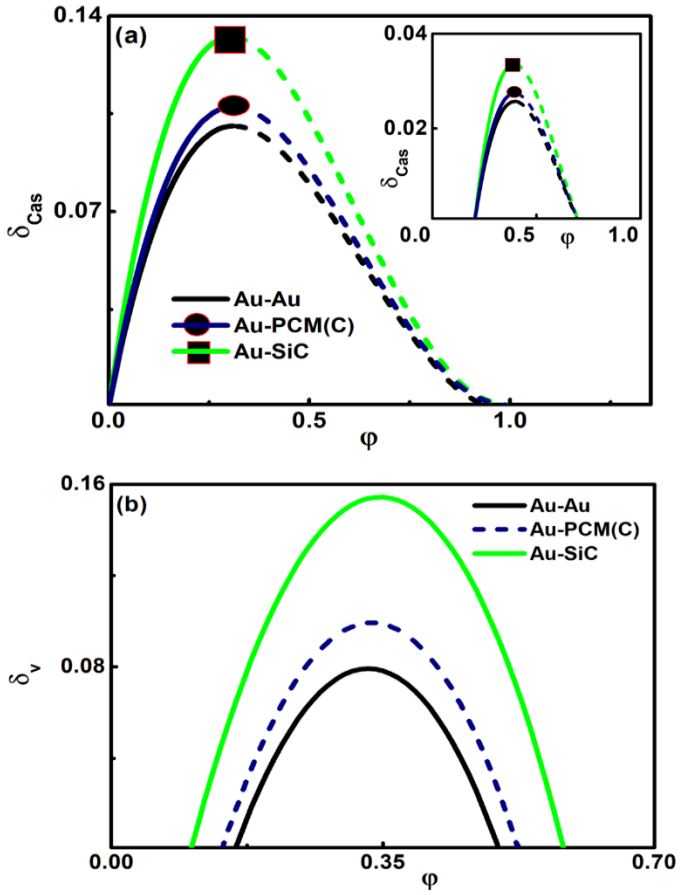

Figure 7.2: (a) Bifurcation diagrams δ_{Cas} vs. φ with $\delta_v = 0$ (the inset shows similar plots for $\delta_v = 0.3$). The solid and dashed lines represent the stable and unstable points respectively. (b) Bifurcation diagrams δ_v vs. φ for δ_{Cas} =0.08.

The situation is qualitatively similar in presence of an electrostatic voltage (inset Figure.7.2a). If the applied voltage increases then δ_{Cas}^{MAX} also decreases. Due to the attractive nature of the electrostatic force, the device would require a higher restoring torque to preserve stable motion of the system. The presence of two equilibrium points occurs if $\delta_{Cas} < \delta_{Cas}^{MAX}$. The equilibrium point closer to $\varphi = 0$ (solid line) is stable and the other one closer to $\varphi = 1$ (dashed line) is unstable. When δ_{Cas} reaches δ_{Cas}^{MAX} for the torsional system with higher conductivity materials, it is still $\delta_{Cas}<\delta_{Cas}^{MAX}$ for the other less conductive materials yielding two equilibrium points and ensuring increased possibility for stable motion. Moreover, voltage bifurcation analysis gives useful information about the device dynamics. Figure 7.2b shows the sensitive dependence of the bifurcation parameter δ_v on materials. Not only the maximum δ_v^{MAX} decreases, but also the distance between the stable and unstable equilibrium points with increasing material conductivity. In all cases, the range of bifurcation parameters to produce stable periodic motion ($0 < \delta_{Cas} < \delta_{Cas}^{MAX}$ and $\delta_v \geq 0$) decreases for increasing material conductivity.

Further information about the dynamics can be obtained from the phase diagrams $d\varphi/dt$ vs. φ. For a conservative system, the homoclinic orbit separates stable motion that manifests itself as continuous oscillation around the stable equilibirum from unstable motion across the unstable equilibrium point which leads to stiction. The homoclinic orbit is the orbit which connects the unstable equilibrium in the limit of infinite positive or negative time to itself. Hence, only the initial conditions in the region of the phase plane, which is enclosed by the homoclinic orbit, result in stable oscillatory motion. For any other initial conditions in the region outside the homoclinic orbit, the moving beam will perform unstable motion and collapse onto the ground plate within one period. As for any conservative system with one degree of freedom, the motion is not chaotic. However, according to Fig. 7.3, for the less conductive material the size of the region enclosed by the homoclinic orbit is larger leading to a wider range for stable operation. In addition, any application of voltage strongly reduces the size of the region enclosed by the homoclinic orbit, and consequently the range of initial conditions that favor stable motion as the material conductivity increases.

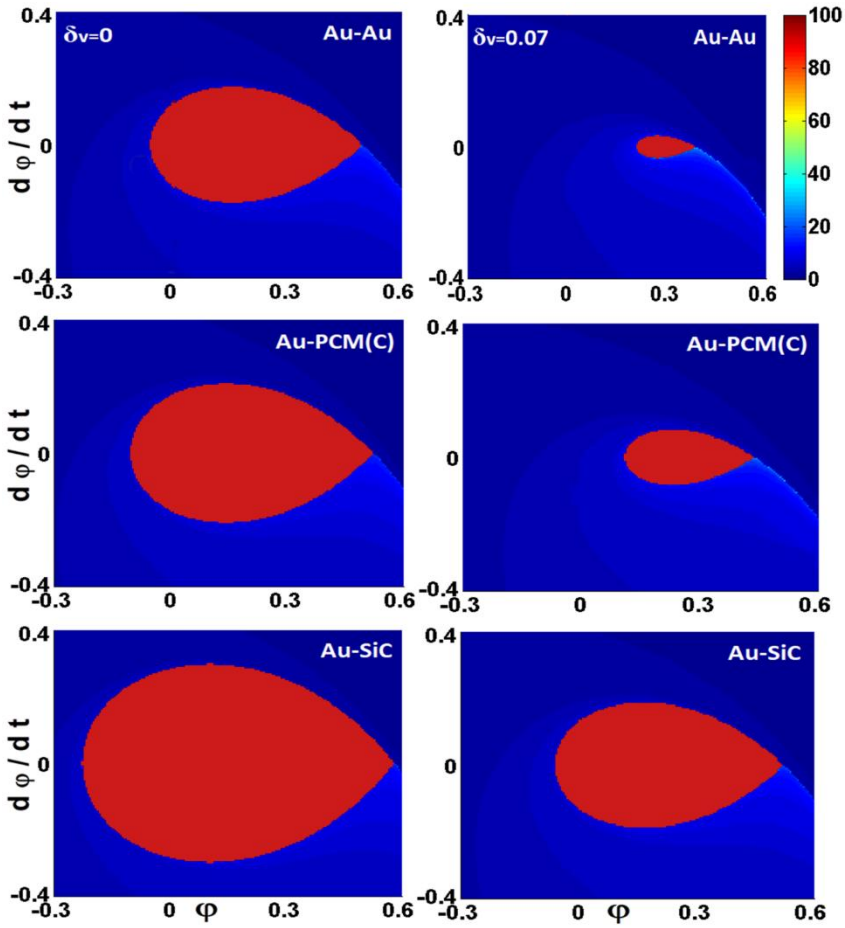

Figure 7.3: Phase portrait $d\varphi/dt$ vs. φ (with $\delta_{Cas} = 0.08$, left column $\delta_v = 0$, and right column $\delta_v = 0.07$) for the conservative system. For the calculations we used 150×150 initial conditions (φ, $d\varphi/dt$). The red region shows that initial condition for which the torsional device shows stable motion after 100 oscillations. The homoclinic orbit separates sharply stable and unstable solutions also reflecting the absence of chaotic behavior.

Non-conservative system ($\varepsilon = 1$)

Here we investigate the existence of chaotic behavior of the torsional system of finite quality factor Q during forced oscillation via an applied external torque $\tau_o \cos(\omega t)$ [30]. In this case the the separatrix (homoclinic orbit) of the conservative system "splits''. For the driven system, the unstable equilibrium turns into an unstable periodic orbit. The splitting of the separatrix means that the orbits which asymptotically reach the unstable periodic orbit in the forward and

backward time directions no longer coincide. These orbits now form the unstable and stable manifolds of the unstable periodic orbit, respectively. Chaotic motion occurs if the stable and unstable manifolds have a transversal intersection. This condition can be investigated by the Melnikov method [30, 38]. If we denote the homoclinic solution of the conservative system as $\varphi_{\mathrm{hom}}^{\mathrm{C}}(\mathrm{T})$, then the Melnikov function for the torsional system is given by [30, 38]

$$\mathrm{M}(\mathrm{T}_0) = \frac{1}{\mathrm{Q}}\int_{-\infty}^{+\infty}\left(\frac{\mathrm{d}\varphi_{\mathrm{hom}}^{\mathrm{C}}(\mathrm{T})}{\mathrm{dT}}\right)^2 \mathrm{dT} + \frac{\tau_0}{\tau_{\mathrm{res}}^{\mathrm{MAX}}}\int_{-\infty}^{+\infty}\frac{\mathrm{d}\varphi_{\mathrm{hom}}^{\mathrm{C}}(\mathrm{T})}{\mathrm{dT}}\cos\left[\frac{\omega}{\omega_0}(\mathrm{T}+\mathrm{T}_0)\right]\mathrm{dT} \tag{7.6}$$

The stable and unstable manifolds have a transverse intersection if the Melnikov function has simple zeros, i.e. $\mathrm{M}(\mathrm{T}_0) = 0$ and $\mathrm{M}'(\mathrm{T}_0) \neq 0$. If $\mathrm{M}(\mathrm{T}_0)$ has no zeros, then the motion will not be chaotic. The conditions of nonsimple zeros, $\mathrm{M}(\mathrm{T}_0) = 0$ and $\mathrm{M}'(\mathrm{T}_0) = 0$ gives the threshold condition for chaotic motion [30, 38]. If we define

$$\mu_{\mathrm{hom}}^{\mathrm{C}} = \int_{-\infty}^{+\infty}\left(\frac{\mathrm{d}\varphi_{\mathrm{hom}}^{\mathrm{C}}(\mathrm{T})}{\mathrm{dT}}\right)^2 \mathrm{dT} \text{ and } \beta(\omega) = \left|\mathrm{H}\left[\Re\left(\mathrm{F}\left\{\frac{\mathrm{d}\varphi_{\mathrm{hom}}^{\mathrm{C}}(\mathrm{T})}{\mathrm{dT}}\right\}\right)\right]\right|, \tag{7.7}$$

then the threshold condition for chaotic motion $\alpha = \beta(\omega)/\mu_{\mathrm{hom}}^{\mathrm{C}}$ with $\alpha = \gamma\,\omega_{0\theta_0}/\tau_0 = (1/\mathrm{Q})\left(\tau_0/\tau_{\mathrm{res}}^{\mathrm{MAX}}\right)^{-1}$ obtains the form

$$\alpha = \frac{\gamma\omega_{0\theta_0}}{\tau_0} = \left|\mathrm{H}\left[\Re\left(\mathrm{F}\left\{\frac{\mathrm{d}\varphi_{\mathrm{hom}}^{\mathrm{C}}(\mathrm{T})}{\mathrm{dT}}\right\}\right)\right]\right| \Big/ \int_{-\infty}^{+\infty}\left(\frac{\mathrm{d}\varphi_{\mathrm{hom}}^{\mathrm{C}}(\mathrm{T})}{\mathrm{dT}}\right)^2 \mathrm{dT}, \tag{7.8}$$

where $\gamma = \mathrm{I}\,\omega_{\mathrm{o}}/\mathrm{Q}$, and $\mathrm{H}[\ldots]$ denotes the Hilbert transform [30, 38].

Figure 7.4 shows the threshold curves $\alpha = \gamma\,\omega_{0\theta_0}/\tau_0$ vs. driving frequency ratio $\omega/\omega_{\mathrm{o}}$. For large values of α (above the curve), the dissipation dominates the driving torque leading to regular motion that asymptotically approaches the stable periodic orbit resulting from the stable equilibrium point of the conservative system. However, for parameter values below the curve, the transversal intersections of the stable and unstable manifolds causes chaotic motion. Clearly for systems with higher conductivity, which lead to stronger Casimir torques, chaotic motion is more likely to occur as it is manifested by the larger area below the threshold curve. Figure 7.4b shows the strong dependence of the region below the threshold curve, which corresponds to chaotic motion, on the applied voltage. The presence of an electrostatic torque changes the threshold curves, which is further amplified by the increasing material conductivity. According to Figure 7.5 the largest change for the threshold condition

belongs to Au-Au system, which has the highest conductivity, while for the Au-Sic system it is drastically weaker for the same applied voltage.

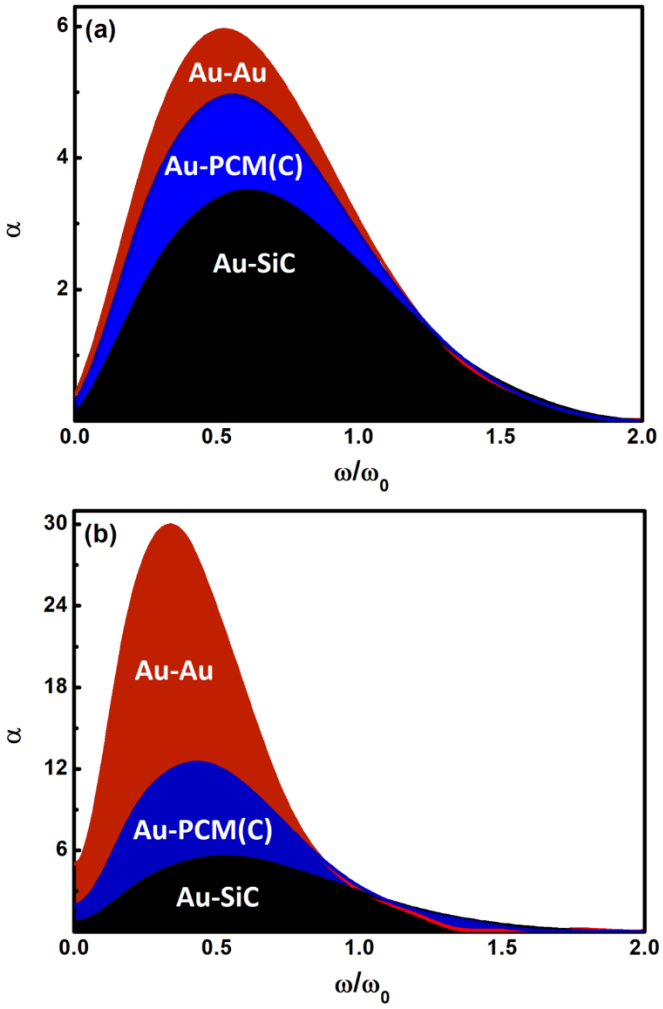

Figure 7.4: Threshold curve $\alpha\left(=\gamma\,\omega_{0\theta_0}/\tau_0\right)$ vs. driving frequency ω/ω_o (with ω_o the natural frequency of the system). The area bellow the curve corresponds to parameters that lead to chaotic motion ($\delta_{Cas} = 0.08$, (a) $\delta_v = 0$ (a) and (b) $\delta_v = 0.07$).

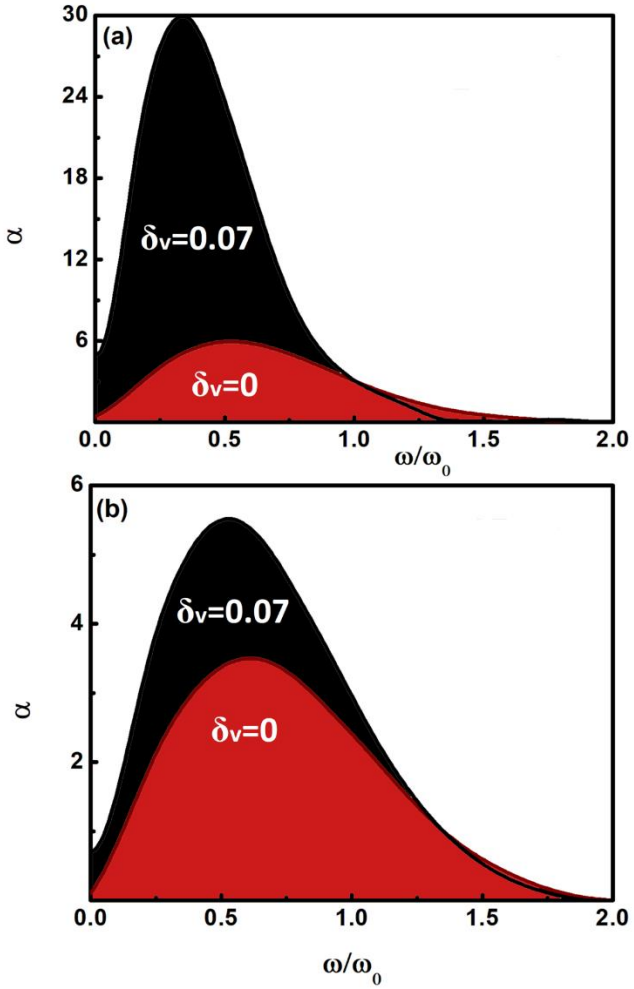

Figure 7.5: Threshold curve $\alpha(\gamma\,\omega_{0\theta_0}/\tau_0)$ vs. driving frequency ω/ω_o (with ω_o the natural frequency of the system) for (a) Au-Au and (b) Au-SiC. The area below the curve corresponds to parameters that lead to chaotic motion

Indeed, the chaotic behavior is shown by the contours of the transient times to stiction in the phase plane in Fig. 7.6 for different values of the threshold parameter α for all materials studied here. If we compare with Fig. 7.3, where chaotic motion does not occur, the latter plots show that chaotic motion takes place since there is no a simple smooth boundary between the red and the dark-blue regions. Chaotic behavior introduces significant risk for stiction, prohibiting long term prediction of the behavior of the oscillating system being more evident for material systems with higher conductivity or equivalently higher Casimir torques. In addition, as in Fig. 7.5 for the threshold curves, the transient times to stiction in Fig. 7.7 show the sensitive dependence of chaotic motion on

the applied electrostatic potential for the Au-Au and Au-SiC systems. Again it is confirmed that any voltage application will strongly influence the chaotic behavior of the system having a dramatic effect for the higher conductivity materials (i.e. Au-Au system).

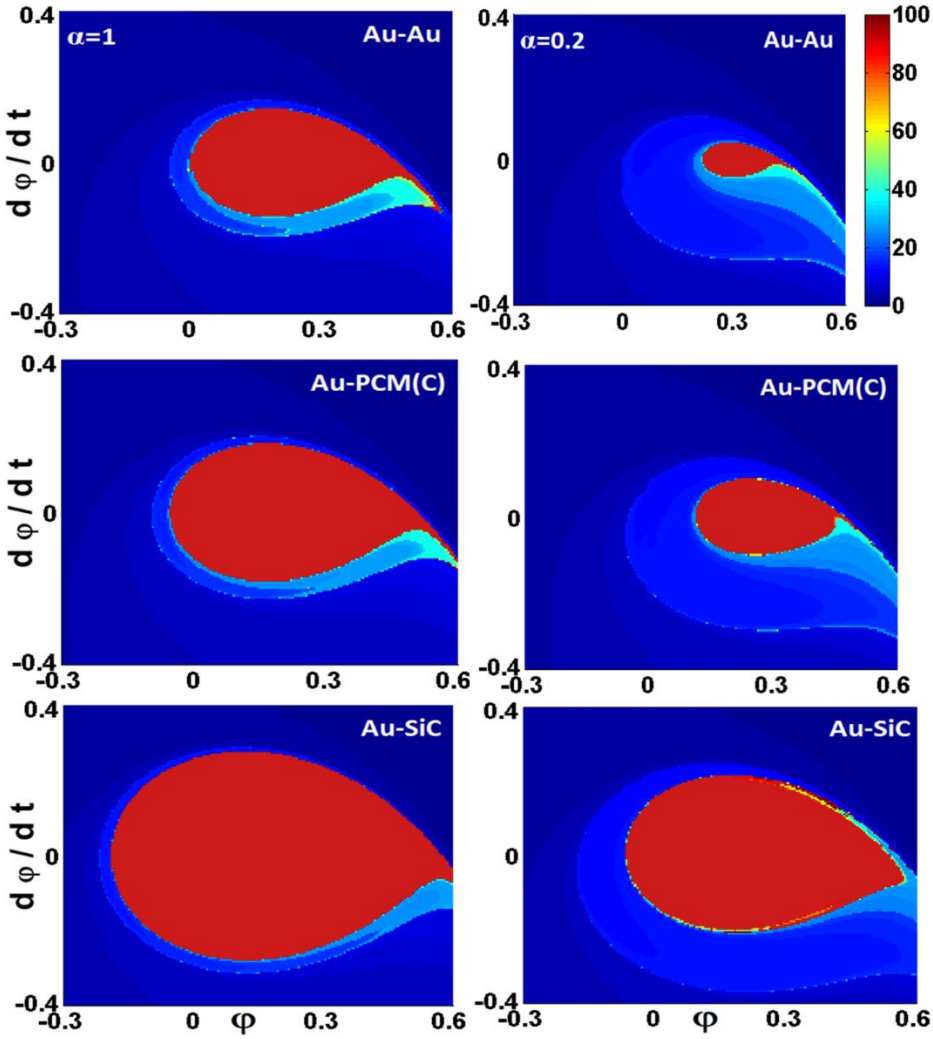

Figure 7.6: Contour plot of the transient times to stiction in the phase plane $d\varphi/dt$ vs. φ ($\delta_{Cas} = 0.08$, $\delta_v = 0$) for the non-conservative system for $\alpha = 1$ (left column) and $\alpha = 0.2$ (right column). For the calculations we used 150×150 initial conditions (φ, $d\varphi/dt$). The red region shows that initial condition for which the torsional device shows still stable motion after 100 oscillations. With decreasing α the chaotic behavior increases, and the area of stable motion (red region) shrinks more for the systems with higher conductivity

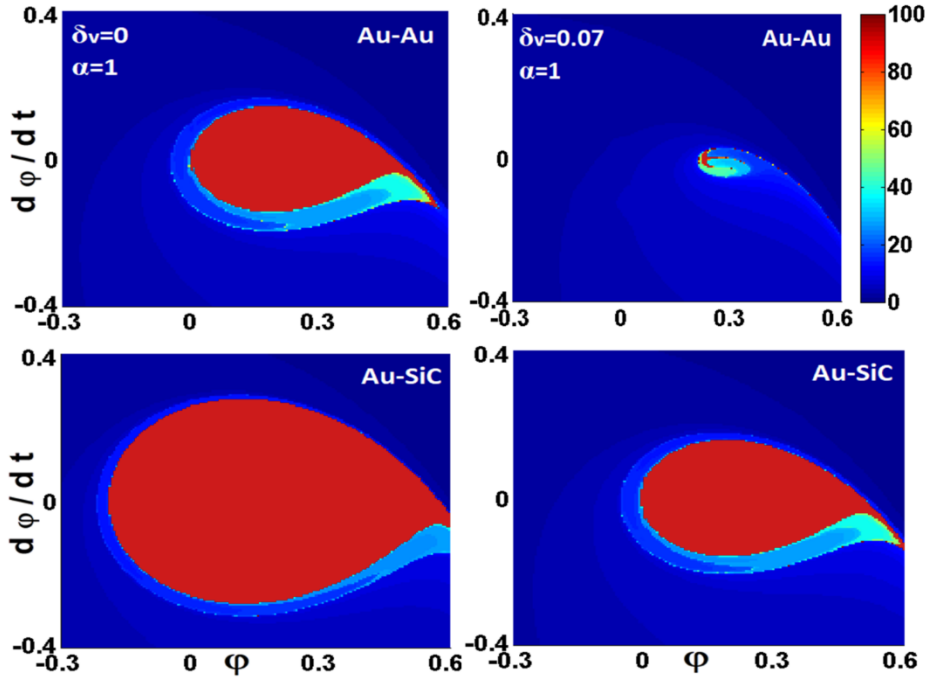

Figure 7.7: Contour plot of the transient times to stiction in the phase plane $d\varphi/dt$ vs. φ ($\delta_{Cas} = 0.08$, $\alpha = 1$) of the non-conservative system with $\delta_v = 0$ (left column) and $\delta_v = 0.07$ (right column) for Au-Au and Au-SiC systems. For the calculations we used 150×150 initial conditions (φ, $d\varphi/dt$). The red region shows the initial conditions for which the torsional device shows stable motion after 100 oscillations. with oscillating frequency $\omega/\omega_0 = 0.5$. With increasing δ_v (or equivalently applied voltage) the chaotic behavior increases, and the area of stable motion shrinks more for the systems with higher conductivity and applied potential.

7.4 Conclusions

In conclusion, chaotic behavior, which is often unavoidable and leads to device malfunction, is strongly dependent on material conductivity and optical properties leading to different Casimir interactions, as well as on the applied electrostatic voltages. For conservative motion, phase portraits and bifurcation analysis show the strong sensitivity of actuation dynamics on the optical properties of interacting materials, where applied electrostatic forces lead faster to instability. For the driven systems, the Melnikov method in agreement with contours

of the transient times to stiction revealed that an increasing material conductivity leads to stronger Casimir torques and subsequently more extensive chaotic behavior. The latter is strongly enhanced with applied electrostatic potentials. Since chaotic behavior leads to increased possibility for stiction prohibiting long term prediction of actuation dynamics, it becomes evident that characterization of the optical properties and conductivity of interacting materials is crucial for the design of dynamical microsystems.

References

[1] J. Israelachvili, *Intermolecular and Surface Forces.* (Academic, New York, 1992).
[2] A.W. Rodriguez, F. Capasso and S. G. Johnson, Nat. Photonics **5** 211 (2011).
[3] F. Capasso, J. N. Munday, D. Iannuzzi and H. B. Chan, IEEE J. Sel. Top. Quant. Electron. **13,** 400 (2007).
[4] M. Bordag, G. L. Klimchitskaya, U. Mohideen and V. M. Mostepanenko, *Advances in the Casimir Effect* (Oxford University Press, New York, 2009).
[5] S. R. Decca, D. López, E. Fischbach , G. L. Klimchitskaya, D. E. Krause and V. M. Mostepanenko, Ann. Phys. (NY) **318**, 37 (2005); Phys. Rev. D **75**, 077101 (2007).
[6] A. Ashourvan, M. F. Miri and R. Golestanian, Phys. Rev. Lett. **98**, 140801 (2014).
[7] M. F. Miri, R. Golestanian, Appl. Phys. Lett. **92,** 113103 (2011).
[8] A. Ashourvan, M. F. Miri and R. Golestanian, Phys. Rev. E. **75,** 040103 (2007).
[9] P. Ball, Fundamental physics: Feel the force, Nature **447,** 77 (2007).
[10] G. Palasantzas and J. Th. M. DeHosson, Phys. Rev. B. **72,** 121409 (2005); G. Palasantzas and J. Th. M. DeHosson, Phys. Rev. B. **72,** 115426 (2005).
[11] F. Tajik, M. Sedighi, M. Khorrami, A. A. Masoudi and G. Palasantzas, Phys. Rev. E **96**, 042215 (2017); F. Tajik, M. Sedighi and G. Palasantzas, J. Appl. Phys. **121**, 174302 (2017).
[12] H. B. G. Casimir and K. Proc, Ned. Akad. Wet. **51,** 793 (1948).
[13] E. M. Lifshitz, Sov. Phys. JETP **2,** 73 (1956); I. E. Dzyaloshinskii, E. M. Lifshitz and L. P. Pitaevskii, Sov. Phys. Usp. **4,** 153 (1961).
[14] O. Bochobza-Degani and Y. Nemirovsky, Sens. Actuators, **A97-98,** 569 (2002).
[15] Y. Nemirovsky and O. Degani and J. Microelectromech, Syst. **10**, 601 (2001).
[16] O. Degani and Y. Nemirovsky, J. Microelectromech. Syst. **11,** 20 (2002).
[17] J. G. Guo and Y. P. Zhao, International Journal of Solids and Structures **43,** 675 (2006); W. H. Lin and Y. P. Zhao, J. Phys. D: Appl. Phys. **40,** 1649 (2007).
[18] R. Satter, F. Plötz, G. Fattinger and G. Wachutka, Sens. Actuators, **A97–98,** 337 (2002).
[19] W. H. Lin and Y. P. Zhao, Chaos, Solitons and Fractals **23,** 1777 (2005).
[20] R. Maboudian and R. T. Howe, J. Vac. Sci. Technol. B **15,** 1 (1997).
[21] G. Palasantzas, V. B. Svetovoy and P. J. van Zwol, Int. J. Mod. Phys. B **24,** 6013 (2010).
[22] F. Chen, G. L. Klimchitskaya, V. M. Mostepanenko and U. M. Mohideen, Opt. Express **15,** 4823 (2007); C. C. Chang, A. A. Banishev, G. L. Klimchitskaya, V. M. Mostepanenko and U. Mohideen, Phys. Rev. Lett. **107,** 090403 (2011).
[23] G. Torricelli, P. J. van Zwol, O. Shpak, G. Palasantzas, V. B. Svetovoy, C. Binns, B. J. Kooi, P. Jost and M. Wuttig, Adv. Funct. Mater. **22,** 3729 (2012).
[24] V. B. Svetovoy, P. J. van Zwol, G. Palasantzas and J. Th. M. DeHosson, Phys. Rev. B. **77** , 035439 (2008).
[25] S. K. Lamoreaux, Phys. Rev. Lett. **78,** 5 (1997); Rep. Prog. Phys. **68,** 201 (2005); H. B. Chan, V. A. Aksyuk, R. N. Kleiman, D. J. Bishop and F. Capasso, Phys. Rev. Lett. **87,** 211801 (2001).

[26] M. Sedighi, V. B. Svetovoy, W. H. Broer and G. Palasantzas, Phys. Rev. B **89,** 195440 (2014)
[27] M. Sedighi, V. B. Svetovoy and G. Palasantzas, Phys. Rev. B **93,** 085434 (2016)
[28] M. Wutting and N. Y. Yamada, Nature Material **6,** 824 (2007)
[29] W. Broer, G. Palasantzas , J. Knoester and V. B. Svetovoy , Phys. Rev. B **87,** 125413 (2013)
[30] W. Broer, H. Waalkens , V. B. Svetovoy, J. Knoester and G. Palasantzas, Phys. Rev. Applied **4,** 054016 (2015)
[31] V. B. Svetovoy and G. Palasantzas, Advances in Colloid and Interface Science **216,** 1 (2015)
[32] F. Intravaia, A. Koev, I.W. Jun, A. A. Talin, P. S. Davids, R. S. Decca, V. A. Aksyuk, D. A. R. Dalvit and D. Lopez, Nature Communications **4,** 2515 (2013); R. S. Decca, D. Lopez, E. Fischbach, G. L. Klimchitskaya, D. E. Krause and V. M. Mostepanenko, *Annals of Physics* **318,** 37 (2005)
[33] S. R. Decca, D. L´opez, E. Fischbach, G. L. Klimchitskaya, D. E. Krause and V. M. Mostepanenko, Phys. Rev. D **75,** 077101 (2007)
[34] O. Degani, E. Socher, A. Lipson, T. Lejtner, D. J. Setter, Sh. Kaldor and Y. Nemirovsky, J. Microelectromech. Syst. **7,** 373 (1998)
[35] W. H. Lin and Y. P. Zhao, J. Phys. D: Appl. Phys. **40,** 1649 (2007)
[36] M. Sedighi, W. H. Broer, G. Palasantzas and B. J. Kooi, Phys. Rev. B **88,** 165423 (2013)
[37] S. Cui and Y. C. Soh, J. Microelectromech. Syst. **19,** 1153 (2010)
[38] J. Guckenheimer and P. Holmes, *Nonlinear Oscillations, Dynamical Systems, and Bifurcations of Vector Fields* (Springer, Berlin, Heidelberg, New York, 1983)

Summary and outlook

We have investigated how self-affine roughness can affect the lateral Casimir force and Casimir torque using the pair wise summation method under appropriate conditions. The results show that this effect is significant, enabling one to tailor roughness parameters in order to obtain the desirable Casimir force and increase the yield of micro or nano-electromechanical devices. It has also be seen that for a positive coefficient cross correlation (γ) between plates, the lateral Casimir force is repulsive for all displacements. This means that the point of no displacement (in which the lateral Casimir force is zero) is an unstable equilibrium when the correlation between the plates is positive. The effect of roughness on the torque is particularly important for the component of the torque which is normal to the plates, as this component vanishes in the absence of roughness. While it was seen that for the component parallel to the plates, there is a nonzero part even if the planes are smooth. The effect of the correlation between the plates increases when the roughness index increases or when the correlation length increases.

By applying the Lifshitz theory it is possible to take into account the material optical properties and consequently the obtained results are more realistic. The latter gives huge importance in the technology of designing and fabrication of micro or nano-electromechanical devices. Therefore we study how the Casimir force is sensitive to changes of the optical properties by using different materials including gold (Au), Phase-Change-Materials (PCMs) in the amorphous and crystalline state, and Silicon Carbide (SiC). In order to obtain accurate information about the dynamic behavior of a micro devices, we have used the phase portraits that characterize the actuation dynamics and show strong sensitivity to changes of the Casimir force as a function of the stiffness of the actuating component. Small changes of the force magnitude can make abrupt changes in the system operation, as for instance, it can lead to stiction. On the other hand, the introduction of energy dissipation can prevent stiction by driving the system to attenuated motion towards equilibrium depending on the optical properties and the system quality factor Q.

The bifurcation and phase portraits analysis of electrostatic torsional MEMS actuations indicated that SiC can enhance the regime of stable equilibria against stiction instabilities. Therefore, it is a good candidate for systems operating in harsh environments in comparison to Au and AIST in both its phases. Also, we have explored how the reversible amorphous to crystalline phase transitions in PCMs can have a strong influence on nanoscale actuation of micro electromechanical systems (MEMS) under the influence of Casimir effect. This

results are valid in both presence and absence of electrostatic voltage in device. Due to the attractive nature of the electrostatic force, the device would require a higher restoring torque to preserve stable motion of the system.

Knowledge of Casimir and electrostatic forces between interacting bodies is not only important from a fundamental point of view, but also these forces playing a crucial role for the performance and stability of microelectromechanical systems (MEMS). In such devices the presence of chaotic behavior, which is often unavoidable, leads to device malfunction due to stiction, and practically it could make impossible to predict whether stiction or stable actuation will occur on a long term basis. We have done research of how the optical properties of different materials and different values of applying voltages influence the chaotic behavior of electrostatic torsional MEMS due to changes in the magnitude of the Casimir forces and torques by use of the Melnikov method and Poincare map for many different value of the initial conditions.

Chaotic behavior leads to increased possibility for stiction prohibiting long term prediction of actuation dynamics. We have illustrated these phenomena in torsional oscillators undergoing both conservative and non-conservative motion. For conservative motion, chaotic behavior is always absent. However, for a non-conservative system chaotic behavior can take place introducing significant risk for stiction. The results reveal that an increasing material conductivity leads to stronger Casimir torques and subsequently more extensive chaotic behavior by increasing applied electrostatic forces lead faster to instability in devices which are fabricate out of more conductive materials. Therefore, for the more conductive crystalline phase that generates stronger Casimir forces and torques, the possibility of occurrence of chaotic behavior increases which it introduces significant risk for stiction.

The presented result in this thesis can be helpful to become familiar and gain accurate information about the dynamical behavior of MEMS/NEMS. This issue is crucially important in the technology of design and fabrication of such devices. Moreover, this kind of knowledge can offer the proper vision to researchers to use suitable materials to adjust the regime of operation to improve productivity, and remain away from any malfunctions such as stiction between moving parts.

Samenvatting

Wij hebben met PWS methode in speciale voorwaarden dat deze methode hoge nauwkeurigheid heeft, gecontroleerd dat hoe kan een ruwheid invloed hebben op bestanddeel van Casimir effect en Casimir moment raaklijn. Resultaten hebben bewezen dat sterke invloed van dit factor op energie en momentmacht zodat een gunstige ruwheid in het systeem is kan een goede niveau van casimireffect produceren en op het einde kan opbrengst verhogen. Er is gezien wanneer de correlatie tussen de bladden positief is, casimireffect raaklijn in alle posities van breedte verplaatsing is weerzinwekkend en dat wil zeggen in deze voorwaarden wanneer er geen breedte verplaatsing is tussen de bladden, wordt een onstabiel evenwicht in het systeem uitgevoerd. Invloed van ruwheid op de krachtmoment is ook te veel. Want dat bestanddeel van de krachtmoment die parallel is met de bladden, wanneer er een gebrek is met de ruwheid blijft dat nog steeds, aanwezigheid van ruwheid in het systeem en correlatie van de bladden kan dit bestanddeel versterken.

Ookal gebruik maken van “Lifshitz” theorie maakt het mogelijk dat de optische kenmerken van fabrikante materialen van microsysteem beter gezien wordt en zo worden de resultaten echter en geldig. Geldige resultaten voor ontwerping en maken van elektromechanische microsysteems zijn belangrijk. Dus wij hebben gecontroleerd dat hoe casimir energie en krachtmoment tegen de verandering van optische kenmerken van fabrikante materialen gevoelig en afhankelijk wordt. Gebruikte element of materiaal in deze onderzoek is goud (Au), veranderende materiaal van de fase (PcMs) in twee fazen zijn Amorphous en Sic. Om geldige informatie te krijgen in verband met dynamische gedrag van microsysteem, is gebruik gemaakt van fase curve, die kunnen strenge gevoeligheid van dynamische gedrag van microsysteem tegen de veranderingen van casimir effect aantonen. Aan de andere kant met de herzienning van energiedissipatie invloed op systeem kan adhesie tussen de bewegende onderdelen van microsysteem voorkomen en stabiele oscillerende bewegingen in systeem kan gehouden worden. Deze invloed is ook afhankelijk van de kwaliteitsfactor en optische kenmerken van het machine.

Analyse van evenwicht curves en fase diagrammen in een draaiende oscillator en elektrostatische micro systeem toont dat de aanwezigheid van **Sic** kan een plaats die in dat systeem oscillerende stabiele bewegingen heeft, vergroten en de adhesie kans verminderen. Dus deze materiaal in vergelijking met goud en veranderende materiaal van fase, voor het maken van microsystemen die in harde omgeving moeten zijn, is geschikt. Ookal hebben

wij gestudeerd dat de aanwezigheid van het omkeerbaar proces van Amorpous fase naar crystal fase in veranderende materiaal van fase kan goede invloed hebben op dynamische gedrag van oscillerende micro systeem. Resultaten in twee omstandigheden zijn geldig.Vanwege de aantrekkelijkheid van elektrostatische energie in dat geval is het nodig dat de machine een hogere niveau van krachtsmoment produceert om te kunnen in een onstabiel oscillerend beweging te blijven.

Kennis van Casimir en elektrostatische krachten tussen interagerende materialen is niet alleen belangrijk vanuit een fundamenteel oogpunt, maar ook deze krachten spelen een cruciale rol voor de prestaties en stabiliteit van micro-elektromechanische systemen (MEMS). Terwijl in dergelijke apparaten de aanwezigheid van chaotisch gedrag, wat vaak onvermijdelijk is, leidt tot een defect van het apparaat als gevolg van stictie en praktisch onmogelijk is om te voorspellen of stictie of stabiele aansturing op lange termijn zal plaatsvinden. We hebben onderzoek gedaan naar de manier waarop de optische eigenschappen van verschillende materialen en de verschillende waarde van de toegepaste spanning het chaotische gedrag van elektrostatische torsie MEMS beïnvloeden als gevolg van veranderingen in de sterkte van de Casimir-krachten en -momenten met behulp van de Melnikov-methode en de Poincare-kaart voor veel verschillende waarden van de initiële waarde. voorwaarden.

Het gepresenteerde resultaat in dit proefschrift kan helpen om vertrouwd te geraken en accurate informatie te verkrijgen over het dynamisch gedrag van MEMS/NEMS. Dit probleem is van cruciaal belang in de technologie van het ontwerp en de fabricage van dergelijke apparaten. Dit soort kennis kan een goede visie bieden aan een onderzoeker die met behulp van geschikt materiaal bedrijfsregimes aanpast om de productiviteit te verbeteren en weg te blijven van eventuele malfuncties zoals stictie tussen bewegende delen.

List of publications

Journal papers

1. **F. Tajik**, A. A. Masoudi and M. Khorrami "Lateral Casimir force between self-affine rough surfaces", Physica B: Condensed Matter. 485, 116 (2016)

2. **F. Tajik**, M. Sedighi and G. Palasantzas"Sensitivity on materials optical properties of single beam torsional Casimir actuation",J. Appl. Phys. 121, 174302 (2017).

3. **F. Tajik**, M. Khorrami ,A. A. Masoudi and F. Mohammad Dezashibi "The effect of roughness and correlation on the Casimir torque between two plates", Int. J. Mod. Phys. B .31, 1750258 (2017).

4. **F. Tajik**, M. Sedighi, M. Khorrami, A A. Masoudi, G Palasantzas, "Chaotic behavior in Casimir oscillators: A case study for phase-change materials", Phys. Rev. E 96, 042215 (2017).

5. **F. Tajik**, M. Sedighi, A. A. Masoudi, H. Waalkense, G. Palasantzas, "Dependence of chaotic actuation dynamics of Casimir oscillators on optical properties and electrostatic effects", Eur. Phys. J. B 91, 71(2018).

Acknowledgements

During the moments of my doctoral study which is approaching towards its end, there were people whose presence were always a true privilege for me. Here, I would like to convey my sincere appreciation to them.

First of all, I would like to express my deepest gratitude to my advisors, Prof. George Palasantzas and Prof. Amir Ali Masoudi and Prof. Mohammd Khorrami, who gave me the opportunity to become familiar with the field of Casimir effect. I am indebted for their tremendous support, continuous encouragement, and never ending trust. Their extensive knowledge, and inspiring enthusiasm for physics were constant motivations for me to work harder and learn more.

I am extremely grateful for getting to know Prof. Vitaly Svetovoy. I would like to sincerely thank him for sharing his scientific perspectives, and for various constructive pieces of advice that he has gave me since we have met.

My sincere thank will also go to Prof. Bart Kooi, for his valuable feedback during group meeting which help me to improve my study.

I would like to acknowledge the companionship and beneficial discussions with Dr. Mehdi Sedighi during my study, especially when I started learning the bifurcation analysis and phase portrait.

I would like to express my gratitude to Gert, he was always available to help me.

I would like to truly thank Anna for her very quick and effective responses in providing things which I needed them and were not available to me. Through her help, I was able to have access to all of them.

I am gratefully acknowledge the members of the assessment committee, Ricardo Decca, Shirin Faraji, and Erik van der Giessen for spending their valuable time on reading this thesis.

I also would like to sincerely thank my friend, Zahra for her companionship and endless support during my stay in Groningen. Also, I would like to express my gratitude to Lijuan and Paul for their help in order to prepare for defense.

Immersing in a scientific atmosphere was not possible without great group members. I also would like to thank all my friends in group in both Groningen University and University of Alzahra who friendly environment of the group owes to them.

My wholeheartedly gratitude goes to my very first teachers, who I have owed a lot to them, my parents. From the deepest part of my heart, I would like to thank my parents for their unconditional love, endless support, infinite patience,

and firm guidance. They are without any doubt the best parent that I can ever imagine.
My special appreciations and profusely thanks are for my brother, who I shared a lot of moments of my whole life with. His companionship to create brilliant moments of my life was a true privilege, which can not be forgotten.